CHARACTERIZING THE ROLE OF DEFECTS ON THE SENSING PERFORMANCE OF CARBON NANOTUBE AND GRAPHENE BASED GAS SENSORS

BY

KEVIN YU-CHUNG LIN

DISSERTATION

Submitted in partial fulfillment of the requirements
for the degree of Doctor of Philosophy in Chemical Engineering
in the Graduate College of the
University of Illinois at Urbana-Champaign, 2011

Urbana, Illinois

Doctoral Committee:

Professor Daniel W. Pack, Chair
Professor Richard I. Masel, Director of Research
Professor Huimin Zhao
Assistant Professor Charles M. Schroeder
Assistant Professor Ryan C. Bailey

Characterizing the role of defects on the sensing performance of carbon nanotube and graphene based gas sensors

Kevin Yu-Chung Lin

Department of Chemical and Biomolecular Engineering

University of Illinois at Urbana-Champaign, 2011

Richard I. Masel, Advisor

The major theme of this thesis is to investigate the influence of defects on the sensing mechanisms and performance of gas sensors made from films of carbon nanotubes, chemical vapor deposition (CVD) graphene film, CVD graphene ribbons, and surfactant exfoliated graphene. The definition of defects on carbon materials is the disordered carbon atoms formed due to dislocations, vacancies, and deformations. These defects were introduced during processing.

The thesis is separated into three sections that analyze various types of defects on these carbon based chemical sensors. First section focuses on single-walled carbon nanotubes with point defects. It will be demonstrated that these point defects can alter the main sensing mechanism of the CNT based sensors. There is a controversy in literature on whether the sensing response seen in carbon nanotube chemiresistors is associated with a change in the resistance of the individual carbon nanotubes or changes in the resistance of the junctions. A network analysis was carried out to better understand the relative contributions of the carbon nanotubes and the junctions on the change in resistance of the carbon nanotube network. It was

found that the dominant mode of detection in carbon nanotube networks changes according to the defect level in the carbon nanotubes which may explain the apparently contradictory results in the literature. With high concentration of the point defects in the carbon nanotube film along with applying high electric field, the Poole-Frenkle conduction regime can be induced. Generally, desorption of gases from carbon nanotubes is a slow process that limits the carbon nanotubes' utility as sensors. It will be demonstrated that electron flows in the carbon nanotube above the Poole-Frenkel conduction threshold can stimulate adsorbates to desorb without heating the sensor significantly. This desorption process is analogous to electron stimulated desorption, but with an internally conducted rather than externally applied source of electrons. As a result, this gives a fast and reversible CNT sensor within seconds. An application can be utilized to use carbon nanotubes based GC detector for multi-component chemical analysis. The approach is to use a CNT based detector in a series configuration with a gas chromatography column. It will demonstrated that a mixture of nine different compounds can be detected with these CNT based detectors when the detector operates in current stimulated desorption (CSD) mode. This is the first demonstration of a CNT based GC detector to analyze multi-component gas mixtures providing a new sensing approach for online air quality control and health monitoring applications.

The second section of the thesis focuses on analyzing two-dimensional line defects arises from wrinkles and grain boundaries as well as edge defected created manually on the graphene film synthesized with chemical vapor deposition (CVD) process. Due to two-dimensional nature of the graphene film, adsorption of isolated analyte molecules on point defects has minimal effect on graphene resistance because current pathways can always form around the adsorbate. In contrast, analytes adsorbing on line defects lead to significant changes in resistance. It will be

demonstrated that polycrystalline graphene easily obtained through chemical vapor deposition contains line defects. This can offer a scalable path to 50x more sensitive chemiresistors than mechanically exfoliated crystalline graphene. Moreover, current flow can be confined by cutting the polycrystalline graphene into ribbons, the sensitivity increases by another factor of four. These results show that polycrystalline graphene has extraordinary sensitivity, achieved through geometry and linear defect density.

The last section of the thesis focuses on intrinsic two-dimensional edge defects on graphene isolated with sodium cholate surfactant assisted exfoliation of graphite powders. With this technique, it is possible to produce high edge defect concentrations for individual graphene island due to its micron-sized dimension offering more defects per unit area. Various randomly-stacked oxide-free graphene films can be formed with various filtration volumes. It will be demonstrated the films produced can range 6 orders of magnitude in film conductance. At thinner graphene films, the electron transport mechanism is mainly through two-dimensional variable range hopping. At thicker graphene films, electron transport is through fluctuation-assisted tunneling. It is also observed the graphene films go from semiconducting-like to metallic-like behavior at around 8 mL filtration volume. At low filtration volumes, oxide-free randomly stacked graphene film sensors showed better sensitivity towards target molecules compared to polycrystalline/ribbon graphene and defective CNT gas sensors due to two-dimensional electron hopping. As the graphene film thickness increases, there is a shift in conduction mechanism from two-dimensional electron hopping to metallic-like conduction which explains the drop in sensitivity as the filtration volume increases.

Dedicated to my family, for their love and support

ACKNOWLEDGEMENTS

First and foremost, I would like to thank my mom, dad, and brother. I will not be where I am today without their continued love and support.

This dissertation would not have been possible without the help and support of many people. I would like to thank my advisor Professor Richard I. Masel. With his insight and assistance throughout, it has been a wonderful experience working on this project. In addition, I would like to thank my other committee members, Professor Daniel W. Pack, Professor Huimin Zhao, Professor Charles M. Schroeder, and Professor Ryan C. Bailey for their time and in agreeing to serve on my defense committee.

It was a great pleasure to having an opportunity to work and share thoughts with my coworkers in the lab. Special thanks to Dr. Amin Salehi-Khojin for collaborating on the carbon nanotubes and graphene projects. I also would like to express my gratitude for my collaborator from Professor Eric Pop's group, David Estrada, on the CVD graphene work. I would like to thank my past and present colleagues in the Masel group for their support and friendship: Dr. Chelsea Monty, Dr. Matthew Luebbers, Dr. Christopher Field, Dr. Zachary Dunbar, Dr. John Haan, Dr. Likun Zhu, Dr. Saeed Moghaddam, Dr. Tianjiao Wu, Nicolas Londono, Robert Morgan, Lingjuan Shen, Wei Zhu, Brian Rosen, and Maryam Sayyah.

TABLE OF CONTENTS

Chapter 1: Introduction

The major theme of this thesis is to investigate the influence of defects on the sensing mechanisms and performance of gas sensors made from films of carbon nanotubes, chemical vapor deposition (CVD) graphene film, CVD graphene ribbons, and surfactant exfoliated graphene. The definition of defects on carbon materials is the disordered carbon atoms formed due to dislocations, vacancies, and deformations. These defects were introduced during processing.

Background information from literature on carbon nanotubes and graphene is presented in Chapter 2. An overview on chemical gas sensors and the various sensing mechanisms were introduced. The intrinsic properties of carbon nanotubes were discussed in detail. Motivation was given as to the reason for using carbon nanotubes as gas sensing materials for gas sensors. Literature review was done to give a brief history of the field and pioneering work on carbon nanotubes based gas sensors was presented further. Both experimental and theoretical aspects were discussed in detail for sensing mechanism when gas molecules adsorbed onto carbon nanotubes surface. The second half of this chapter is dedicated on graphene. The intrinsic properties of graphene were first introduced. Various graphene isolation and synthesis techniques were presented in details along with its advantages and disadvantages for each technique. Brief introduction pertained to graphene was done in characterizing the film. Literature review on graphene based gas sensors was presented along with the pioneering work in this field. Experimental and theoretical aspects of gas molecules adsorption on graphene surface were discussed in detail.

Major fabrication techniques that were used in manufacturing silicon substrates for carbon nanotubes and graphene gas sensors were presented in Chapter 3. First, the theoretical backgrounds on these fabrication processes were discussed. Device fabrication process flow sheet was presented to give a detailed fabrication recipe in manufacturing these silicon substrates.

Non-thermal current stimulated desorption of gases from carbon nanotubes was presented in Chapter 4. Motivation was given as to desorbing gas molecules from carbon nanotubes within a short amount of time at room temperature is of particular interest to the carbon nanotube gas sensor community. Experimental procedures were discussed in producing carbon nanotubes films and the conditions the sensor was operated at that would result in gas desorption within a short amount of time frame. Theoretical explanations were presented as to how defects can influence the sensing mechanism, sensing performance, and coupled with high electric field that can promote desorption.

Ultra fast carbon nanotubes based GC detectors for multi-component gas mixtures is presented in Chapter 5. Here, approaches were discussed in operating the carbon nanotubes to detect 9 component gas mixture that would utilize the application of current-stimulated desorption process developed in Chapter 4. It is also investigated as to what happens to carbon nanotubes detection when it is not operated at the CSD regime.

On the sensing mechanism in carbon nanotubes chemiresistors is presented in Chapter 6. Motivation was given in conflicting reports on the exact gas sensing mechanism when molecules adsorbed onto the carbon nanotubes. Detailed simulation study was done and presented here to categorize the various sensing mechanism groups when the carbon nanotubes are consisted of

perfect tubes, highly defective tubes and in-between cases. Efficient current for electron hopping and 1/f noise in carbon nanotubes were investigated in details.

Polycrystalline graphene ribbons as chemiresistors is presented in Chapter 7. Motivation was given as to investigate the effects of defects for CVD grown graphene and graphene ribbons based gas sensors. Comparisons were performed to analyze sensing responses for mechanically exfoliated pristine graphene, CVD graphene film, CVD graphene ribbons and carbon nanotubes based gas sensors. Experimental procedures were discussed in details on manufacturing and characterizing these films. The side effect of PMMA residue was presented as well that is common during processing. Simple COMSOL simulation was set up to analyze the electron transport in these films for various cases presented in this chapter.

Randomly stacked oxide-free graphene film based gas sensors is presented in Chapter 8. This is the first demonstration in literature for gas sensors made of these films. Previous studies were mostly on reduced graphene oxide based gas sensors. Surfactant/solvent exfoliation of graphite to produce graphene has been recently explored as an alternative approach to chemically modified graphene process in producing large scale low cost graphene materials. How defects affect the electron transport has not been explored yet in systems like these with overlapping graphene layers rather than continuous graphene film. This is demonstrated in this chapter to discover the effect of 2D electron hopping and the sensing performance of these sensors. It is also observed the intrinsic properties change when the thickness of these overlapping layers increases. Lastly, the sensing performances were compared with other carbon based gas sensors under same experimental conditions.

In summary, this thesis focused mainly on the effect of defects on the sensing performances of these gas sensors made with different carbon based materials. The thesis is separated into two sections. The first section is focused on carbon nanotubes based gas sensors and discuss how defects can affect electric conduction mechanism, gas sensing mechanism, and be utilized in promoting gas desorption within a short time. The second section is focused on graphene based gas sensors. CVD graphene film, CVD graphene ribbons, and surfactant exfoliated graphene were discussed in details and how defects can affect the gas sensing performance and electron conduction through these films.

Chapter 2: Literature Review on Carbon Nanotubes and Graphene

2.1 Introduction on Chemical Gas Sensors

A physical device that is able to change the physical properties upon exposure to gas molecules either through electrical conductance, capacitance or mass is known as a chemical gas sensor. An electrical signal is measured upon the change in these properties. The results are then used to detect the gas molecules. Fast response time and acceptable accuracy are the two main requirements for gas sensors. Size, weight and cost are the main constraints along with capability to measure the physical properties over a typical lifetime.

Depending upon the applications, gas sensors can be grouped based on the operating principles. Examples for such application include conductive polymer sensors, surface acoustic wave sensors, field-effect transistors, electrochemical sensors, and chemiresistors. The traditional applications for the gas sensors can be found in medical analysis, and toxic gas monitoring. Newfound applications consist of waste water monitoring, military defense, food and beverage process, and consumer products.

Typically, conventional laboratory analytical instruments such as mass spectroscopy, gas chromatography, and ion mobility spectroscopy are costly and complex instruments to run analysis. In contrast, commercially available gas sensors have advantages in lower cost, smaller size and simpler to operate. Typical gas sensors can be from micrometers to centimeters while the size can be reduced due to large scale ups of such productions. These all make these gas sensors viable for real time in situ environments. The common drawbacks for gas sensors

include sensitivity, selectivity, stability, and reproducibility which could render these gas sensors unsuitable for long term applications. Considerable interests have been on new room temperature operated gas sensing materials. Due to the high surface area and the ability to change electrical properties at room temperature upon exposure to gas molecules, carbon nanotubes (CNT) have been a promising new gas sensing material.[1]

Nanotechnology is known as any process or product that has sub micrometer dimensions. Since 1990s, new research interests that have seen rapid growth due to nanotechnology include high performance nanomaterials, microelectromechanical systems, and nanoscale electronics. As a result, recent advancements in nanotechnology have provided opportunities to improve sensor performances dramatically. Therefore, a huge effort in research has been carried out in new gas sensors as the demand of gas detection technologies is increased. It is indeed not surprising to see the sensor research community as a beneficiary due to advanced nanomaterial developments as carbon nanotubes have been one of the mostly studied nanomaterial.

2.2 Properties of Carbon Nanotubes

Ijiima first discovered CNTs in 1991 at the Japanese NEC Corporation.[2] Carbon nanotubes have special structures that are different from graphite. There are three types of CNTs: single-walled carbon nanotubes (SWNT), double-walled carbon nanotubes (DWNT) and multi-walled carbon nanotubes (MWNT). Single-walled carbon nanotubes consist of a single layer of graphene sheet wrapped into a cylindrical tube. Double-walled and multi-walled carbon nanotubes comprise of two and array of SWNTs respectively that are concentrically nested like rings of a tree trunk.[3] The typical diameter of CNTs ranges from 1 to 100 nm and lengths up to

millimeters. The most common CNT synthesis techniques include chemical vapor deposition, carbon arc discharge and laser ablation of carbon.

Single-walled carbon nanotubes can either be metallic or semiconducting depending on the direction in which the graphene sheet rolls to form the cylinder tube. The diameter and chirality of a SWNT are characterized by the graphene lattice vectors.[4] Carbon nanotubes types are determined by the n and m integer values. Depending on these n and m values, it can be either amchair (n=m), zigzag (n=0 or m=0) or chiral (any other n and m). All armchair SWNTs and those with n-m = 3k (k is a nonzero integer) are metallic. All others are semiconducting with the band gap inversely dependent on the diameter.[3] Electron transport in CNTs was found to take place through quantum effects and be ballistic along the tube axis without scattering due to its one-dimensional nature. As a result, they are capable of conducting high current density without dissipating heat.[5, 6] Theoretically, metallic CNTs can have a current density of 1000 times higher than that of metals such as copper.[7]

Carbon nanotubes are excellent thermal conductors along the tube axis due to the ballistic electron conduction. It has been reported in literature the room temperature thermal conductivity is 3000 W/m-K for CNTs which is greater than that of natural diamond.[8] It has also been predicted that the thermal conductivity of CNTs could reach 6000 W/m-K at room temperature which is 15 times increase of copper,[7] a well known metal for its high thermal conductivity. Superconductivity has also been reported in CNTs at low temperatures.[9, 10]

Carbon nanotubes are one of the strongest and stiffest materials known consisting of high Young's modulus and tensile strength. The mechanical strength is due to the covalent sp^2 bond formed between the individual carbon atoms along the walls of CNTs. It has been reported CNT

has Young's modulus of 0.64 TPa[11, 12] and tensile strength of 63 GPa[13] which is 50 times greater than carbon steel.[14] Therefore, the high mechanical strength and unique electrical properties of CNTs have attracted considerable interest for various applications.

2.3 Carbon Nanotubes Based Gas Sensors

Carbon nanotubes are surface reacting materials as they are composed of entirely surface atoms where adsorbed gas molecules can dramatically change CNT electrical properties at room temperature. The ballistic electron transport along the tube axis provides excellent transduction of the altered electrical signal to the external contact. The long term performance of CNTs based sensors is stable due to their chemically robust graphitic surface. The aforementioned three reasons made CNTs extensively researched material for chemical gas sensing applications. Therefore, great research interests in the sensor community have been on room temperature CNT based gas sensors.

Kong[15] and Collins[16] were the first groups to report the adsorption of gas molecules can dramatically change the electrical conductance of SWNTs. Kong's group investigated individual semiconducting SWNT as a resistive sensor for NO_2 and NH_3 detection at room temperature in argon. They demonstrated that an electron acceptor molecule NO_2 can cause the conductivity of SWNT to increase while an electron donor molecule NH_3 can cause a reduction in conductance.[15] They concluded that the gas sensing mechanism is based on the charge transfer between the semiconducting SWNT and electron accepting NO_2 and electron donating NH_3 gas molecules. The recovery time of these sensors were found to be 12 hours.[15] Using conductivity measurement and scanning tunneling microscopy (STM), Collins demonstrated that the electrical

resistance, and local density of states of SWNTs are sensitive to oxygen exposure. They described the change in SWNT resistance is due to the charge transfer between adsorbed oxygen molecules and SWNTs.[16]

Chen's group was the first to discover the photo-induced gas desorption in gas moelcule-CNT system.[18] They found that UV light induced desorption of oxygen, NO_2, and NH_3 molecules can drastically alter the electrical characteristics of semiconducting SWNTs and suggested that the photo-desorption in CNTs is a non-thermal process and is dependent on wavelength. Li's group confirmed the experimental results obtained by Chen's group. Li investigated[17] an SWNT based sensor for detecting NO_2 and nitrotoluene vapors at room temperature. Due to the high bonding energy between NO_2 and SWNT, the sensor recovered slowly with a recovery time of 10 hours. They applied ultraviolet (UV) light during recovery and successfully accelerated the recovery time to 10 minutes.[17] They reported that UV light lowered the desorption energy barrier of CNTs thus facilitating the NO_2 desorption.

Zhao has performed first principle calculations on the electronic properties of SWNT upon adsorption of various gas molecules.[19] They found all molecules either electron donor or electron acceptor are weakly adsorbed onto SWNT with small charge transfer. They also obtained the equilibrium position, adsorption energy, charge transfer, and electronic band structures for SWNTs with various structures.[19] Therefore, theoretical studies have also predicted significant variation of the electric properties of CNTs as the result of gas molecule adsorption.

Bradley's group measured the amount of charge transfer to SWNT from one molecule of NH_3 to be 0.04 electrons.[20] Qi calculated that NO_2 binds to the SWNT surface with energy of 0.8 eV and withdraws 0.1 electron per molecule.[21] Chang[22] performed density function theory

calculation and showed that binding energy is 0.18 eV for NH_3 and 0.42 for NO_2. Therefore, they stated that physisorption and electron charge transfer are the major mechanisms for the change in conductivity for both NH_3 and NO_2 molecules binding to SWNTs.

2.4 Graphene Properties

Graphene is a mono-layer graphite sheet consisting of carbon atoms bonding together in a two-dimensional hexagonal structure. Each carbon atom bonds with three other carbon atoms with strong sp^2 hybridized sigma bonds of length 1.42 angstroms. In graphene, the delocalized pi electrons are unbounded and available for electric conduction. In contrast, these delocalized pi bonds of 3.35 angstroms length are what kept these individual graphene sheets bounded weakly from one another in graphite.

Graphene is known as a zero bandgap semiconductor due to valence band is full and conduction band has no electrons as a result of the energy that the bands touch coincides with the Fermi energy. The energy bands start to overlap as the number of layers in graphene samples increases, and it becomes semi-metallic. With two layers, the overlap is 1.6 meV. The overlap increases with the number of layers and reaching 10% of graphite by eleventh layer.[23]

Linear dispersion around the K-point is an unique feature of single layer graphene band structure. Therefore for graphene, the velocity of electrons near the K-point is constant at 10^6 m/s. This linear dispersion is similar to a system of relativistic particles with zero effective mass.[23] This is the reason why many interesting quantum mechanical effects were observed in graphene. Study has also shown that electrons in graphene obey the Dirac equation with zero rest mass.[24] Graphene also displays Klein effect as electrons can tunnel through potential

barriers with almost 100% probabilities. One of the most studied quantum mechanical effects in graphene is the quantum Hall effect. It is a property of two-dimensional structures in the presence of very strong magnetic fields, the Hall resistivity of the material takes on specific quantized values.[25]

Graphene has been shown to be the strongest material ever measured with a breaking force of 42 N/m.[26] It is also flexible and stretchable as experiments have shown little change in the electrical resistance of graphene.[25] Graphene has also been shown to have the highest known thermal conductivity at 5000 W/m-K.[27] Optically, graphene is quite transparent with 70% transmittance over the visible and infrared regions of the spectrum.[28] It has been found experimentally that graphene becomes visible when placed on a silicon substrate with 300 nm oxide.[29] Therefore, aforementioned exceptional properties make graphene suitable for large variety of applications.

2.5 Graphene Isolation/Synthesis Methods

Graphene is a mono-layer plane of carbon atoms bonded together in a hexagonal lattice. The three-dimensional structure built of these stacked sheets of graphene is the ordinary graphite that we are familiar with. Surprisingly, scientists were not able to isolate these two-dimensional graphene from its bulk graphite until 2004. Nonetheless, an extensive amount of research efforts have be done in discovering novel ways to produce mono-layer graphene samples for applications and studies.

First the pioneer technique of mechanical cleavage of highly oriented pyrolitic graphite (HOPG) is presented. Next, methods used to obtain graphene from carbon nanotubes are

introduced. Graphene obtained from the epitaxial growth on silicon carbide is then briefly discussed before the new techniques involving chemical vapor deposition (CVD) of graphene from carbon gas sources onto various metal surfaces. The method of oxidation of graphite and subsequent reduction of graphene oxide to produce graphene is then discussed in detail. Finally, surfactant or solvent assisted exfoliation of graphite to produce graphene is introduced in more details.

2.6 Mechanical Cleavage from Graphite (HOPG)

The original method used to isolate mono-layer of graphene has been known as the "Scotch tape" method. It involves mechanical cleavage or mechanical exfoliation of graphene films from bulk graphite samples. This method is mechanical due to the application and subsequent removal of sticky tape onto the graphite sample to obtain graphene.

The initial complex process developed by Novoselov[30] involved lithography patterning and oxygen plasma etching onto the surface of HOPG sample. The sample was then pressed against fresh wet photoresist (PR) which was allowed to harden. These became attached to the PR and were able to be cleaved from the rest of the HOPG sample. Each of the islands of graphitic material stuck on the PR was next peeled thinner and thinner by repeatedly using Scotch tape to remove layer after layer. Thereby leaving only single and few layered graphene samples behind. Finally, these graphene samples were then released in acetone and dispersed onto a silicon substrate.

The subsequent improved and simpler method involves taking a piece of tape, sticking it to a HOPG sample, and then peeling off the top layers.[31] With a chunk of graphitic material

stuck onto the tape, the tape is then pressed against the graphitic material again on a clean location. By unpeeling the tape, the graphitic material is separated into two pieces. The process is repeated ten times, each time cleaving the graphitic material thinner until single layer regions remain on the tape. The tape is then pressed against the silicon substrate to transfer the graphene to the substrate before slowly removing the tape.

The Scotch tape method is a fairly easy process in obtaining graphene, although finding mono-layer graphene sheets can be challenging among thicker few layers. Mechanical exfoliation from HOPG is still the best process in producing high quality mono-layer graphene sheets. However, the disadvantage of this process is the lack of control over the number of layers and is an inefficient process not suitable for large scale productions.

2.7 Graphene from Unzipping Carbon Nanotubes

An alternative process in producing graphene is through using carbon nanotubes as starting materials and unzips them to form graphene. The two main approaches for unzipping CNTs are through chemical treatment and plasma etching.

In the chemical treatment method,[32] CNTs are suspended in concentrated sulfuric acid. Dilute potassium permanganate is then added and solution is heated for thirty minutes. This treatment unzips the CNTs, but also oxidizes the material so it is actually a graphene oxide rather than graphene which needs to be subsequently reduced through hydrazine or reduction methods.

In the plasma etching method,[33] higher quality graphene samples are produced than the chemical treatment method. However, it is generally considered more complex as CNTs must

first be embedded in PMMA polymer. Etching was done in argon plasma. The disadvantage of this approach is the complex nature of the process and inefficient for large scale productions.

2.8 Epitaxial Growth on Silicon Carbide

Berger's group first reported the controlled growth of graphene films on silicon carbide (SiC).[35] They were unable to observe a quantum Hall effect on these graphene samples. Growing these graphene films on different surfaces of SiC has seen a lot more progress ever since.[36]

These graphene grown on SiC have shown similar electrical transport as those obtained by mechanical exfoliated on HOPG. Due to the contact between graphene sheet with the SiC substrate, it has made these graphene sheets unique as well. Due to SiC substrate doping, these graphenes are n-type as the Fermi level lies 0.4 eV above the point when the valence and conduction bands touch.[37] As a result, a bandgap of 0.26 eV is created whenever mono-layer of grpahene is grown on SiC. However, increase in graphene film thickness has been observed on decreasing of the substrate induced bandgap. At four layers, the effect is no longer observed.[38]

Advantage with epitaxial growth of graphene on SiC is the potential to bypass lengthy process of removing graphene from graphite and re-deposition of these graphene onto the substrate. Therefore, it has the potential to be a simple and reproducible process for graphene synthesis. Disadvantage with this process is that the first layer of graphene has no graphene electronic properties and mainly acts as a buffer layer. Due to the charge transfer from SiC substrate to graphene layers which in turn introduced a bandgap making the subsequent graphene

layers n-type. The process also requires high temperatures and ultrahigh vacuum as well as high cost limiting the applications.

2.9 Chemical Vapor Deposition

The most recent advances in graphene synthesis involved using chemical vapor deposition (CVD) of carbon precursors (methane, ethylene) onto the surfaces of various metals (Ni, Cu).[25, 39-41] This technique has demonstrated the ability to produce high quality mono-layer graphenes.

Exact flow rate of carbon precursors, inert and reducing gases, temperature of the reaction chamber, heating and cooling rates, and the thickness as well as the quality of the metal substrates are the main variables in every CVD processes that have to optimized in order to obtain large area continuous mono-layer graphene.

The most popular approach in synthesizing graphene is through the use of Ni metal substrate.[41] A 500 nm nickel films is first evaporated/sputtered onto silicon substrate. The CVD process consists of two major steps. During the first step, the metal Ni substrate is heated to 1000 Celsius for 20 minutes under argon flow of 600 sccm and hydrogen flow of 500 sccm. The purpose of this step is to let the polycrystalline nickel to form large grains in the order of 20 microns. Therefore, it can allow better uniformity of graphene grown on top of Ni substrate. The second step is the actual CVD growth. The sample is maintained at 1000 Celsius while the hydrogen flow is increased to 1500 sccm and methane flow of 25 sccm is substituted for the argon. The reaction time is 10 minutes.

During the CVD process, carbon only precipitates to the surface as it is cooled. Study has shown that slower cooling rates of less than 25 Celsius/min gave a greater area covered by mono to double layer graphene films than faster cooling rates with more than 100 Celsius/min. For very slow cooling rates of 4 Celsius/min, the coverage is 87% maximum for less than double-layer graphene.[42]

CVD grown graphene process offers four major advantages. These graphene films have excellent electrical properties as well as large area coverage. It is also compatible with existing fabrication processes as the Ni film can be patterned first follow by metal lift-off procedure by etching off the undesired Ni prior to CVD process. It also affords the possibility for transferring to other substrates. In order to give these graphene film better mechanical stiffness and stability before the film is transferred, it is typical to spin coat the film first with polymethylmethacrylate PMMA polymer. Photoresist stripper is subsequently used to dissolve away these PMMA polymers. The disadvantages with CVD process include wrinkles introduced on the graphene film during processing as well as PR polymer residues and etchant residues.

2.10 Reduction of Graphene Oxide (GO)

The use of Hummers[43] method first published in 1958 to synthesis graphene oxide (GO) involves mixing graphite flakes with sulfuric acid, sodium nitrate, and potassium permanganate. The later modification[44] of Hummers method requires the pretreatment of graphite with sulfuric acid, potassium perfulfate, and phosphorous pentoxide. The modified Hummers method also ignores the main oxidation step of Hummers method through the use of sodium nitrate.

After oxidizing graphite, graphene oxide is created. Due to its hydrophilic nature, it therefore enables these GO sheets dispersion in water. The GO sheets are different from pristine graphene due to their low electrical conductivity.[45] The conductivity of GO is low as well due to the presence of hydroxyl and epoxy functional groups chemically bonded to the surface of these graphene. Through the removal of these functional groups from GO, the conductivity can be recovered.[46]

The two main processes in removing these functional groups are thermal treatment[47, 48] by exposing the GO sheets to extremely high temperatures, and chemical treatments[45, 49, 50] through reducing agent hydrazine. The most common technique in characterizing these GO sheets through electrical measurements is first dispersed them in solution follow by depositing on silicon substrate along with metal contact deposition through photolithography patterning.

In the thermal treatment studies to reduce these GO sheets,[48] GO flakes resistance values were measured in situ. Initially before any thermal treatment is done, the GO resistance was too high to be measurable. However, studies have shown these graphene samples obtained through graphene oxide reduction can go from giga-ohms to mega-ohms after thermal treatments.

An alternative method to thermal reduction is by chemical reduction through hydrazine reducing agent to increase the GO conductivities. Before and after hydrazine reduction procedure, Gilje[49] also observed the same resistance drop as thermal reduction method from giga-ohms to mega-ohms on these overlapping GO sheets. However, the conductivity is far inferior to the pristine graphene with graphene obtained through this chemical reduction technique as well as the thermal reduction method.[48, 49]

The advantage of reduced graphene oxide wet chemistry process is the simple and low cost process leading to viable large scale productions. The disadvantages include high temperature required to thermally reduce graphene oxide post processing or toxic reducing chemical hydrazine required to chemically reduce it. Hydrazine also introduces extra nitrogen functional groups on graphene surface in addition to oxygen functional groups introduced during oxidation step.

2.11 Surfactant/Solvent Assisted Exfoliation of Graphite

Recent studies of using surfactant and solvent assisted exfoliation of graphite to produce graphene have produce interests as an alternative method to chemically reduced graphene oxide process. Surfactant and solvent assisted exfoliated graphene is a large scale and high throughput processing method. It is also an oxide-free process as no oxidation is done chemically throughout the procedure. It has been reported predominately edge rather than basal plane defects of graphene are introduced during this process.[51] These dispersions can be used to prepare high quality free standing graphene films.

The method involves powdered graphite as the starting material and various surfactants (SDBS, sodium cholate) or solvents (N-methyl-pyrrolidone or NMP) is used to exfoliate graphite in either a bath sonicator or an ultrasonication equipment.[29, 51-59] After sonication, the resulting dispersions were centrifuged to allow sedimentation of large/thick layers to settle down to the bottom. The top resulting dispersion is decanted for use.

2.12 Raman Spectroscopy

Determination on the defect concentrations and the number of graphene layers can be done using Raman spectroscopy. This method is simpler than other methods such as atomic force microscopy (AFM) or transmission electron microscopy (TEM) in quantizing these values. First, the target sample is irradiated with a particle frequency light source. The scattered light is then analyzed. Raman shift is the change in frequency that corresponds to the excitation of a phonon. This different light frequency from original light source is the result of re-emitted remainder energy from the sample as some of the energy is used to create an optical phonon when the photon is originally absorbed on the sample.

Raman scattering results are typically presented with wave numbers on the x-axis in units of cm^{-1} and intensity on the y-axis in arbitrary units. The wave number represents a frequency shift from the incident light source. The detector is then used to measure the intensity of the scattered light over a range of frequencies and compare to the original light source. Typically, peaks appear at specific wave numbers that is characteristic of a specific material.

Each graphene layer of the sample shows a distinct Raman spectrum which can be used for determination on number of layers. The characteristic Raman spectrum shows three main peaks. The first peak is due to the sample defects which is known as the "D" band occurring at around 1350 cm^{-1}. The peak at around 1580 cm^{-1} is known as the "G" peak. Finally, the last peak at around 2700 cm^{-1} has been known as the "G'" or "2D" peak. It has been reported in literature that the 2D peak is significantly larger and more sharply peaked for graphene than for graphite upon exposure of incident light source with 514 nm laser. The 2D peak has also been found to shift to slightly lower wave numbers as well.[60] The number of graphene layers on a

sample has been found to be correlated to the 2D FWHM. Mono-layer graphene exhibits FWHM of 24 cm^{-1} and increases with subsequent layer and finally to bulk graphite at 60 cm^{-1}.[61]

2.13 Graphene Based Gas Sensors

Graphene has been shown to be a potential material for gas sensing applications. Graphene based gas sensors have been demonstrated by Schedin's group to be able to detect individual gas molecules as they adsorbed onto graphene surface either by donating or accepting an electron which in turn affects the sensor's conductivity.[62] The experiments were conducting with Hall resistivity measurements in a vacuum environment. Several types of gas molecules were investigated and it was found that NO_2 and H_2O acted as electron acceptors, while NH_3 and CO were electron donors. They concluded the unity surface to volume ratio very low levels of intrinsic noises were the main reasons for graphene's surprising sensitivity towards individual molecule detections.

Studies have been done to determine the energy required for gas adsorption on graphene surface using density functional theory[63] to do first principle calculations. The calculations used three different adsorption sites. One adsorption site is directly on top of a carbon atom, one is at the center of a carbon hexagon, and the other at the center of a carbon-carbon bond. Several orientations of the gas molecule on graphene surface were calculated for each type of molecule. The calculated adsorption energy and the amount of charge transferred to the graphene sheet from the gas molecule were reported for each molecule orientation.

The results of the theoretical[63] work correlate very nicely with the experimental[62] results. The most stable orientation of H_2O was found to produce an electron transfer of 0.025 e^-

/molecule from graphene to the H_2O molecule, making it an electron acceptor gas. NO_2 is also shown theoretically to be an acceptor gas with an electron transfer of 0.099 e^-/molecule, making it a stronger electron acceptor than H_2O. The calculations also predict both NH_3 and CO to be electron donor gases and confirmed experimentally.

Adsorbed water is a surface impurity on graphene based gas sensors as it can cause indirect doping of graphene by water from the ambient. Therefore, even if water not initially present on graphene, the water molecules might diffuse into graphene upon exposure to humid air. This is the result of P-type doping of graphene by ambient water molecules.[64]

Studies done have also shown that polymer residues could unintentionally functionalize graphene sensors by providing a surface phase in which the gas molecules can adsorb and influence charge transfer from the gas to the graphene or vice versa.[62, 65, 66] The polymer residue is fairly common when lithographic resists (PMMA) are used. Studies[65] were done to confirm the effects of polymer residues on graphene gas sensors using mechanically exfoliated graphene before and after removal of PMMA residues. Commonly, PMMA were rid of by resist stripper or acetone. However, it has been confirmed the residues left behind after processing. It has been suggested further cleaning procedure can get rid of PMMA completely and leaving the graphene surface clean. The process[65] is through heating graphene to 400 Celsius in a reducing H_2/Ar atmosphere for 1 hr. The electrical quality of the devices improved as carrier mobility increased by four times and the doped carrier density was reduced by nearly 70%.

Most recent studies using graphene as the material for gas sensors have focused on using reduced graphene oxide[67-70] method rather than mechanical exfoliation,[62, 65] epitaxial growth on SiC,[71] and CVD growth of graphene routes.[72] It is not surprising as chemical route is easier to

produce large scale and easily manipulates graphene as compared to other techniques. Either the defects or functional groups in reduced graphene oxide can act as high energy adsorption sites thereby increasing the sensitivity to target gas adsorptions.

Robinson et al.[70] used hydrazine reduced graphene oxide with variable degrees of reduction and was able to detect HCN, chloroethylethylsulfide, dimethylmethylphosphonates and DNT (70 ppb, 0.5 ppb, 5 ppb, 0.1 ppb, respectively). Jung et al.[48] used both thermal and chemical reduction routes on graphene oxide for their sensors to detect H_2O (0.1 torr of H_2O). Lu et al.[69] used low temperature thermal reduction of graphene oxide to detect NO_2 gas at 2 ppm. Fowler et al.[68] used hydrazine reduced graphene oxide at various reduction levels to detect NO_2, NH_3, and DNT (5 ppm NO_2, 5 ppm NH_3, 28 ppb DNT).

Schedin et al.[62] used mechanically exfoliated graphene to detect NO_2, H_2O, I_2, NH_3, CO and ethanol at 1 ppb. Dan et al.[65] also used same exfoliation process to detect H_2O, NH_3, nonanal, octanoic acid, and trimethylamine (30 ppm with nonanal). Pearce et al.[71] used epitaxial growth of graphene on SiC to detect NO_2 at 2.5 ppm. Joshi et al.[72] used CVD grown graphene and ribbons to detect 100 ppm of O_2, CO and NO_2.

2.14 References

1. Moulton, S. E.; Minett, A. I.; Wallace, G. G., Carbon Nanotube Based Electronic and Electrochemical Sensors. *Sensor Letters* **2005,** *3* (3), 183-193.
2. Iijima, S., Helical Microtubules of Graphitic Carbon. *Nature* **1991,** *354* (6348), 56-58.
3. Baughman, R. H.; Zakhidov, A. A.; De Heer, W. A., Carbon Nanotubes - the Route toward Applications. *Science* **2002,** *297* (5582), 787-792.

4. Wildöer, J. W. G.; Venema, L. C.; Rinzler, A. G.; Smalley, R. E.; Dekker, C., Electronic Structure of Atomically Resolved Carbon Nanotubes. *Nature* **1998,** *391* (6662), 59-62.

5. Liang, W.; Bockrath, M.; Bozovic, D.; Hafner, J. H.; Tinkham, M.; Park, H., Fabry-Perot Interference in a Nanotube Electron Waveguide. *Nature* **2001,** *411* (6838), 665-669.

6. Frank, S.; Poncharal, P.; Wang, Z. L.; De Heer, W. A., Carbon Nanotube Quantum Resistors. *Science* **1998,** *280* (5370), 1744-1746.

7. Collins, P. G.; Avouris, P., Nanotubes for Electronics. *Scientific American* **2000,** *283* (6), 62-69.

8. Kim, P.; Shi, L.; Majumdar, A.; McEuen, P. L., Thermal Transport Measurements of Individual Multiwalled Nanotubes. *Physical Review Letters* **2001,** *87* (21), 2155021-2155024.

9. Kociak, M.; Kasumov, A. Y.; Guéron, S.; Reulet, B.; Khodos, I. I.; Gorbatov, Y. B.; Volkov, V. T.; Vaccarini, L.; Bouchiat, H., Superconductivity in Ropes of Single-Walled Carbon Nanotubes. *Physical Review Letters* **2001,** *86* (11), 2416-2419.

10. Tang, Z. K.; Zhang, L.; Wang, N.; Zhang, X. X.; Wen, G. H.; Li, G. D.; Wang, J. N.; Chan, C. T.; Sheng, P., Superconductivity in 4 Angstrom Single-Walled Carbon Nanotubes. *Science* **2001,** *292* (5526), 2462-2465.

11. Gao, G.; Çağin, T.; Goddard Iii, W. A., Energetics, Structure, Mechanical and Vibrational Properties of Single-Walled Carbon Nanotubes. *Nanotechnology* **1998,** *9* (3), 184-191.

12. Yu, M. F.; Files, B. S.; Arepalli, S.; Ruoff, R. S., Tensile Loading of Ropes of Single Wall Carbon Nanotubes and Their Mechanical Properties. *Physical Review Letters* **2000,** *84* (24), 5552-5555.

13. Yu, M. F.; Lourie, O.; Dyer, M. J.; Moloni, K.; Kelly, T. F.; Ruoff, R. S., Strength and Breaking Mechanism of Multiwalled Carbon Nanotubes under Tensile Load. *Science* **2000,** *287* (5453), 637-640.

14. Qian, D.; Wagner, G. J.; Liu, W. K.; Yu, M. F.; Ruoff, R. S., Mechanics of Carbon Nanotubes. *Applied Mechanics Reviews* **2002,** *55* (6), 495-532.

15. Kong, J.; Franklin, N. R.; Zhou, C.; Chapline, M. G.; Peng, S.; Cho, K.; Dai, H., Nanotube Molecular Wires as Chemical Sensors. *Science* **2000,** *287* (5453), 622-625.

16. Collins, P. G.; Bradley, K.; Ishigami, M.; Zettl, A., Extreme Oxygen Sensitivity of Electronic Properties of Carbon Nanotubes. *Science* **2000,** *287* (5459), 1801-1804.

17. Li, J.; Lu, Y.; Ye, Q.; Cinke, M.; Han, J.; Meyyappan, M., Carbon Nanotube Sensors for Gas and Organic Vapor Detection. *Nano Letters* **2003,** *3* (7), 929-933.

18. Chen, R. J.; Franklin, N. R.; Kong, J.; Cao, J.; Tombler, T. W.; Zhang, Y.; Dai, H., Molecular Photodesorption from Single-Walled Carbon Nanotubes. *Applied Physics Letters* **2001,** *79* (14), 2258-2260.

19. Zhao, J.; Buldum, A.; Han, J.; Lu, J. P., Gas Molecule Adsorption in Carbon Nanotubes and Nanotube Bundles. *Nanotechnology* **2002,** *13* (2), 195-200.

20. Bradley, K.; Gabriel, J. C. P.; Briman, M.; Star, A.; Grüner, G., Charge Transfer from Ammonia Physisorbed on Nanotubes. *Physical Review Letters* **2003,** *91* (21), 218301/1-218301/4.

21. Qi, P.; Vermesh, O.; Grecu, M.; Javey, A.; Wang, Q.; Dai, H.; Peng, S.; Cho, K. J., Toward Large Arrays of Multiplex Functionalized Carbon Nanotube Sensors for Highly Sensitive and Selective Molecular Detection. *Nano Letters* **2003,** *3* (3), 347-351.

22. Chang, H.; Lee, J. D.; Lee, S. M.; Lee, Y. H., Adsorption of Nh3 and No2 Molecules on Carbon Nanotubes. *Applied Physics Letters* **2001,** *79* (23), 3863-3865.

23. Partoens, B.; Peeters, F. M., From Graphene to Graphite: Electronic Structure around the K Point. *Physical Review B - Condensed Matter and Materials Physics* **2006,** *74* (7).

24. Novoselov, K. S.; Geim, A. K.; Morozov, S. V.; Jiang, D.; Katsnelson, M. I.; Grigorieva, I. V.; Dubonos, S. V.; Firsov, A. A., Two-Dimensional Gas of Massless Dirac Fermions in Graphene. *Nature* **2005,** *438* (7065), 197-200.

25. Kim, K. S.; Zhao, Y.; Jang, H.; Lee, S. Y.; Kim, J. M.; Ahn, J. H.; Kim, P.; Choi, J. Y.; Hong, B. H., Large-Scale Pattern Growth of Graphene Films for Stretchable Transparent Electrodes. *Nature* **2009,** *457* (7230), 706-710.

26. Lee, C.; Wei, X.; Kysar, J. W.; Hone, J., Measurement of the Elastic Properties and Intrinsic Strength of Monolayer Graphene. *Science* **2008,** *321* (5887), 385-388.

27. Ghosh, S.; Nika, D. L.; Pokatilov, E. P.; Balandin, A. A., Heat Conduction in Graphene: Experimental Study and Theoretical Interpretation. *New Journal of Physics* **2009,** *11*.

28. Wang, X.; Zhi, L.; Müllen, K., Transparent, Conductive Graphene Electrodes for Dye-Sensitized Solar Cells. *Nano Letters* **2008,** *8* (1), 323-327.

29. Blake, P.; Hill, E. W.; Castro Neto, A. H.; Novoselov, K. S.; Jiang, D.; Yang, R.; Booth, T. J.; Geim, A. K., Making Graphene Visible. *Applied Physics Letters* **2007,** *91* (6).

30. Novoselov, K. S.; Geim, A. K.; Morozov, S. V.; Jiang, D.; Zhang, Y.; Dubonos, S. V.; Grigorieva, I. V.; Firsov, A. A., Electric Field in Atomically Thin Carbon Films. *Science* **2004,** *306* (5696), 666-669.

31. Geim, A. K.; Kim, P., Carbon Wonderland. *Scientific American* **2008,** *298* (4), 90-97.

32. Kosynkin, D. V.; Higginbotham, A. L.; Sinitskii, A.; Lomeda, J. R.; Dimiev, A.; Price, B. K.; Tour, J. M., Longitudinal Unzipping of Carbon Nanotubes to Form Graphene Nanoribbons. *Nature* **2009,** *458* (7240), 872-876.

33. Jiao, L.; Zhang, L.; Wang, X.; Diankov, G.; Dai, H., Narrow Graphene Nanoribbons from Carbon Nanotubes. *Nature* **2009,** *458* (7240), 877-880.

34. Forbeaux, I.; Themlin, J. M.; Debever, J. M., Heteroepitaxial Graphite on 6h-Sic(0001): Interface Formation through Conduction-Band Electronic Structure. *Physical Review B - Condensed Matter and Materials Physics* **1998,** *58* (24), 16396-16406.

35. Berger, C.; Song, Z.; Li, T.; Li, X.; Ogbazghi, A. Y.; Feng, R.; Dai, Z.; Alexei, N.; Conrad, M. E. H.; First, P. N.; De Heer, W. A., Ultrathin Epitaxial Graphite: 2d Electron Gas Properties and a Route toward Graphene-Based Nanoelectronics. *Journal of Physical Chemistry B* **2004,** *108* (52), 19912-19916.

36. Seyller, T.; Bostwick, A.; Emtsev, K. V.; Horn, K.; Ley, L.; McChesney, J. L.; Ohta, T.; Riley, J. D.; Rotenberg, E.; Speck, F., Epitaxial Graphene: A New Material. *Physica Status Solidi (B) Basic Research* **2008,** *245* (7), 1436-1446.

37. Varchon, F.; Feng, R.; Hass, J.; Li, X.; Nguyen, B. N.; Naud, C.; Mallet, P.; Veuillen, J. Y.; Berger, C.; Conrad, E. H.; Magaud, L., Electronic Structure of Epitaxial Graphene Layers on Sic: Effect of the Substrate. *Physical Review Letters* **2007,** *99* (12).

38. Zhou, S. Y.; Gweon, G. H.; Fedorov, A. V.; First, P. N.; De Heer, W. A.; Lee, D. H.; Guinea, F.; Castro Neto, A. H.; Lanzara, A., Substrate-Induced Bandgap Opening in Epitaxial Graphene. *Nature Materials* **2007,** *6* (10), 770-775.

39. Levendorf, M. P.; Ruiz-Vargas, C. S.; Garg, S.; Park, J., Transfer-Free Batch Fabrication of Single Layer Graphene Transistors. *Nano Letters* **2009,** *9* (12), 4479-4483.

40. Eom, D.; Prezzi, D.; Rim, K. T.; Zhou, H.; Lefenfeld, M.; Xiao, S.; Nuckolls, C.; Hybertsen, M. S.; Heinz, T. F.; Flynn, G. W., Structure and Electronic Properties of Graphene Nanoislands on Co(0001). *Nano Letters* **2009,** *9* (8), 2844-2848.

41. Reina, A.; Jia, X.; Ho, J.; Nezich, D.; Son, H.; Bulovic, V.; Dresselhaus, M. S.; Jing, K., Large Area, Few-Layer Graphene Films on Arbitrary Substrates by Chemical Vapor Deposition. *Nano Letters* **2009,** *9* (1), 30-35.

42. Reina, A.; Thiele, S.; Jia, X. T.; Bhaviripudi, S.; Dresselhaus, M. S.; Schaefer, J. A.; Kong, J., Growth of Large-Area Single- and Bi-Layer Graphene by Controlled Carbon Precipitation on Polycrystalline Ni Surfaces. *Nano Research* **2009,** *2* (6), 509-516.

43. Hummers Jr, W. S.; Offeman, R. E., Preparation of Graphitic Oxide. *Journal of the American Chemical Society* **1958,** *80* (6), 1339.

44. Kovtyukhova, N. I., Layer-by-Layer Assembly of Ultrathin Composite Films from Micron-Sized Graphite Oxide Sheets and Polycations. *Chemistry of Materials* **1999,** *11* (3), 771-778.

45. Stankovich, S.; Dikin, D. A.; Piner, R. D.; Kohlhaas, K. A.; Kleinhammes, A.; Jia, Y.; Wu, Y.; Nguyen, S. T.; Ruoff, R. S., Synthesis of Graphene-Based Nanosheets Via Chemical Reduction of Exfoliated Graphite Oxide. *Carbon* **2007,** *45* (7), 1558-1565.

46. Boukhvalov, D. W.; Katsnelson, M. I., Modeling of Graphite Oxide. *Journal of the American Chemical Society* **2008,** *130* (32), 10697-10701.

47. Hirata, M.; Gotou, T.; Ohba, M., Thin-Film Particles of Graphite Oxide. 2: Preliminary Studies for Internal Micro Fabrication of Single Particle and Carbonaceous Electronic Circuits. *Carbon* **2005,** *43* (3), 503-510.

48. Jung, I.; Dikin, D. A.; Piner, R. D.; Ruoff, R. S., Tunable Electrical Conductivity of Individual Graphene Oxide Sheets Reduced at "Low" Temperatures. *Nano Letters* **2008,** *8* (12), 4283-4287.

49. Gilje, S.; Han, S.; Wang, M.; Wang, K. L.; Kaner, R. B., A Chemical Route to Graphene for Device Applications. *Nano Letters* **2007,** *7* (11), 3394-3398.

50. Gómez-Navarro, C.; Weitz, R. T.; Bittner, A. M.; Scolari, M.; Mews, A.; Burghard, M.; Kern, K., Electronic Transport Properties of Individual Chemically Reduced Graphene Oxide Sheets. *Nano Letters* **2007,** *7* (11), 3499-3503.

51. Khan, U.; O'Neill, A.; Lotya, M.; De, S.; Coleman, J. N., High-Concentration Solvent Exfoliation of Graphene. *Small* **2010,** *6* (7), 864-871.

52. Bourlinos, A. B.; Georgakilas, V.; Zboril, R.; Sterioti, T. A.; Stubos, A. K., Liquid-Phase Exfoliation of Graphite Towards Solubilized Graphenes. *Small* **2009,** *5* (16), 1841-1845.

53. De, S.; King, P. J.; Lotya, M.; O'Neill, A.; Doherty, E. M.; Hernandez, Y.; Duesberg, G. S.; Coleman, J. N., Flexible, Transparent, Conducting Films of Randomly Stacked Graphene from Surfactant-Stabilized, Oxide-Free Graphene Dispersions. *Small* **2009,** *6*, 458-464.

54. Green, A. A.; Hersam, M. C., Solution Phase Production of Graphene with Controlled Thickness Via Density Differentiation. *Nano Letters* **2009,** *9* (12), 4031-4036.

55. Hamilton, C. E.; Lomeda, J. R.; Sun, Z.; Tour, J. M.; Barron, A. R., High-Yield Organic Dispersions of Unfunctionalized Graphene. *Nano Letters* **2009,** *9* (10), 3460-3462.

56. Hernandez, Y.; Lotya, M.; Rickard, D.; Bergin, S. D.; Coleman, J. N., Measurement of Multicomponent Solubility Parameters for Graphene Facilitates Solvent Discovery. *Langmuir* **2010,** *26* (5), 3208-3213.

57. Hernandez, Y.; Nicolosi, V.; Lotya, M.; Blighe, F. M.; Sun, Z.; De, S.; McGovern, I. T.; Holland, B.; Byrne, M.; Gun'ko, Y. K.; Boland, J. J.; Niraj, P.; Duesberg, G.; Krishnamurthy, S.; Goodhue, R.; Hutchison, J.; Scardaci, V.; Ferrari, A. C.; Coleman, J. N., High-Yield Production of Graphene by Liquid-Phase Exfoliation of Graphite. *Nature Nanotechnology* **2008,** *3* (9), 563-568.

58. Lotya, M.; Hernandez, Y.; King, P. J.; Smith, R. J.; Nicolosi, V.; Karlsson, L. S.; Blighe, F. M.; De, S.; Zhiming, W.; McGovern, I. T.; Duesberg, G. S.; Coleman, J. N., Liquid Phase Production of Graphene by Exfoliation of Graphite in Surfactant/Water Solutions. *Journal of the American Chemical Society* **2009,** *131* (10), 3611-3620.

59. Vadukumpully, S.; Paul, J.; Valiyaveettil, S., Cationic Surfactant Mediated Exfoliation of Graphite into Graphene Flakes. *Carbon* **2009,** *47* (14), 3288-3294.

60. Ferrari, A. C.; Meyer, J. C.; Scardaci, V.; Casiraghi, C.; Lazzeri, M.; Mauri, F.; Piscanec, S.; Jiang, D.; Novoselov, K. S.; Roth, S.; Geim, A. K., Raman Spectrum of Graphene and Graphene Layers. *Physical Review Letters* **2006,** *97* (18).

61. Malard, L. M.; Nilsson, J.; Elias, D. C.; Brant, J. C.; Plentz, F.; Alves, E. S.; Castro Neto, A. H.; Pimenta, M. A., Probing the Electronic Structure of Bilayer Graphene by Raman Scattering. *Physical Review B - Condensed Matter and Materials Physics* **2007,** *76* (20).

62. Schedin, F.; Geim, A. K.; Morozov, S. V.; Hill, E. W.; Blake, P.; Katsnelson, M. I.; Novoselov, K. S., Detection of Individual Gas Molecules Adsorbed on Graphene. *Nature Materials* **2007,** *6* (9), 652-655.

63. Leenaerts, O.; Partoens, B.; Peeters, F. M., Adsorption of H2 O, N H3, Co, N O2, and No on Graphene: A First-Principles Study. *Physical Review B - Condensed Matter and Materials Physics* **2008,** *77* (12).

64. Romero, H. E.; Joshi, P.; Gupta, A. K.; Gutierrez, H. R.; Cole, M. W.; Tadigadapa, S. A.; Eklund, P. C., Adsorption of Ammonia on Graphene. *Nanotechnology* **2009,** *20* (24).

65. Dan, Y.; Lu, Y.; Kybert, N. J.; Luo, Z.; Johnson, A. T. C., Intrinsic Response of Graphene Vapor Sensors. *Nano Letters* **2009,** *9* (4), 1472-1475.

66. Ishigami, M.; Chen, J. H.; Cullen, W. G.; Fuhrer, M. S.; Williams, E. D., Atomic Structure of Graphene on Sio2. *Nano Letters* **2007,** *7* (6), 1643-1648.

67. Dua, V.; Surwade, S. P.; Ammu, S.; Agnihotra, S. R.; Jain, S.; Roberts, K. E.; Park, S.; Ruoff, R. S.; Manohar, S. K., All-Organic Vapor Sensor Using Inkjet-Printed Reduced Graphene Oxide. *Angewandte Chemie - International Edition* **2010,** *49* (12), 2154-2157.

68. Fowler, J. D.; Allen, M. J.; Tung, V. C.; Yang, Y.; Kaner, R. B.; Weiller, B. H., Practical Chemical Sensors from Chemically Derived Graphene. *ACS Nano* **2009,** *3* (2), 301-306.

69. Lu, G.; Ocola, L. E.; Chen, J., Gas Detection Using Low-Temperature Reduced Graphene Oxide Sheets. *Applied Physics Letters* **2009,** *94* (8).

70. Robinson, J. T.; Perkins, F. K.; Snow, E. S.; Wei, Z.; Sheehan, P. E., Reduced Graphene Oxide Molecular Sensors. *Nano Letters* **2008,** *8* (10), 3137-3140.

71. Pearce, R.; Iakimov, T.; Andersson, M.; Hultman, L.; Spetz, A. L.; Yakimova, R., Epitaxially Grown Graphene Based Gas Sensors for Ultra Sensitive No2 Detection. *Sensors and Actuators, B: Chemical* **2011**.

72. Joshi, R. K.; Gomez, H.; Alvi, F.; Kumar, A., Graphene Films and Ribbons for Sensing of O2, and 100 Ppm of Co and No2 in Practical Conditions. *J. Phys. Chem. C* **2010,** *114* (14), 6610-6613.

Chapter 3: Fabrication of Silicon Devices

Here, major fabrication techniques that are essential in this project would be presented to introduce them in the sequence of processing steps used to prepare samples for study. The first process is the thermal oxidation of silicon. Next is the photolithography process follow by thin metal film deposition by sputtering system. Lastly, fabrication sequences is presented in manufacturing silicon devices to be used throughout.

3.1 Thermal Oxidation of Silicon

It has been observed that graphene becomes visible when placed on a substrate of silicon with silicon oxide. The first step of the fabrication process is the thermal oxidation of silicon wafers. The mathematical model for silicon oxide was worked out by Deal and Grove in 1965.[1] In their model, the incoming oxygen must diffuse through any native layer of SiO_2 already present in order to reach the silicon surface and react to form more oxide. This leads to a reduced reaction rate as oxidation proceeds. Due to this reason, clean wafers were dip in buffered oxide etchant (BOE) solution to etch away any native oxides on them.

3.2 Photolithography

After oxidation of silicon wafers, the process of photolithography is next to create electrode patterns for subsequent gold deposition. First the theory of photolithography will be reviewed.

Photolithography[2] or optical lithography is the transfer of a pattern by selective exposure to a radiation source such as UV light from a photomask to a photosensitive material deposited on a substrate.

The photolithography process involves several steps which are substrate preparation, photoresist application, soft baking, exposure, developing and hard baking. Silicon wafer is the most commonly used material as a substrate. The photosensitive material is mostly a light sensitive resist known as a photoresist that changes its physical properties when exposed to the radiation source. It is deposited on the substrate by spin coating to produce a thin and uniform film at the surface of the substrate. It is followed by soft baking to harden the photoresist. A transparent plate with patterned chromium areas printed on it is known as a photomask or shadow mask. The mask is placed between the radiation source and wafer to selectively expose parts of the substrate to light. Then the exposed positive resist will become soluble in a developing solution. Exposed areas are removed with the developing solution leaving the substrate with the patter of the mask. The remaining photoresist would become a protecting layer for the underlying substrate.

3.3 Thin Metal Film Deposition via Sputtering Process

Physical vapor deposition[2] (PVD) is a physical reaction where the material to be deposited is moved from a target source to the substrate. Sputtering is the commonly used method in PVD for metal deposition. The formation of a thin film deposit on a substrate consists of two steps. First, atoms from a source material are rejected by energetic ions. The atoms are then condensed on the substrate to form a film.

The basic theory with sputtering process is discussed as follows. First, a combination of magnetic and electric fields was used in order to accelerate the ions towards the target material. These high energy ions cause the atoms from the target material to be expelled upon impact with sufficient energy. These target material atoms then re-deposit onto the surface of the substrate to form a thin film.

Stripping electrons away from inert gas argons is done via high electric field application. As a result, a mixture of free electrons and positive ions are created which is known as plasma. This high electric field accelerates these heavy positive ions onto the target material when it is held at a negative potential. A magnetic field is created through the use of a circular rings of magnets that is behind the target material and then subsequently trap these heavy ions into circular orbits above the surface of the target material. As a result, the rate at which target material is bombarded with ions is increased.

Electric field is used to generate the plasma and the power used is the main factor in determining the deposition rate. The number of atoms ejected from the target material surface per each ion striking on the surface is different for different materials. The sputter yield determines the deposition rate which is dependent on the ratio of atoms ejected per incident ion. The film thickness is controlled by the amount of time that a shutter covering the target is left open which allows the deposition on the substrate at a given deposition rate. Simply rotating the substrate beneath the target can improve the uniformity of the deposited film.

After the thin film of metal layer had been deposited, the lift-off process is used to remove metal from unwanted regions. During the sputtering process, metal was deposited everywhere on the wafer. In the areas where the photoresist was removed, the metal would

adhere directly to the oxide underneath. This forms the pattern that is desired. On the other hand, the metal that deposits onto of the photoresist areas is removed by soaking the wafer in acetone and exposing to mild ultrasonic agitation. This allows the acetone to dissolve away the photoresist with the unwanted metal on top leaving only the desired metal patterns behind.

3.4 Device Fabrication Process Flow Sheet

The substrates used in this project were from single side polished (SSP) 100 mm silicon wafer (Silicon Quest, 500 micron thick, <100> orientation, 1-5 ohm-cm nominal resistivity). Clean wafers were dip in buffered oxide etchant (BOE) solution and water in equal parts for one minute to etch away any native oxides on them.

The 6-stack multi-zone tube furnace system located at MNMS cleanroom was used for dry oxidation. The temperature of the oxidation process is chosen at 1100 Celsius. For these parameters, the Deal-Grove equation gives an expected growth time of 13 hr for 500 nm thick oxide with 6 L/min oxygen flow.

The wafer was spin coated with photoresist AZ1518 (HD AZ Electronic Material) at 3000 rpm for 30 seconds. With these parameters, it would yield resist thickness around 500 nm. The wafer is then soft baked on hot plate at 110 Celsius for 2 minutes. The resist was patterned using an Electron Visions (EVG) double sided manual aligner (Figure 3.1). Once the photoresist has been exposed, the wafer is placed in a dish of 400K developer mixed with four parts of DI water. It was found two minute in the developer was required with exposure time of 8 seconds. The developed wafer is then inspected under optical microscope to ensure all patterns were developed properly. The sample is then rinsed thoroughly with DI water and placed on a

110 Celsius hotplate for 2 minutes. Oxygen plasma (Jupiter RIE) was used to descum the photoresist at 250 W for 30 seconds (O_2/Ar of 3/1).

For this project, thin metal films of gold and chromium were deposited via sputtering process (AJA 8-gun DC metal sputtering system) (Figure 3.2, 3.3). A thin layer of gold of 100 nm on top of thinner layer of chromium of 10 nm was used. Gold was preferred as electrical contacts for its low resistivity and excellent stability. Chromium was used as an adhesion layer to help the gold to stick to the substrate. Lift off technique was employed here to remove unneeded metal layers.

The patterned side of the wafer is coated with the photoresist to protect the gold contacts for dicing up individual device chips in the laser shop (Figure 3.4). The chips were stripped with photoresist via stripper solution (400T stripper) and cleaned in SC-1 solution (10:2:1 ratio of H_20:H_2O_2:NH_4OH). Self assembled monolayer (SAM) process was done in 3-aminopropyl triethoxysilane (APTES) solution (1 ml APTES, 200 ml acetone).

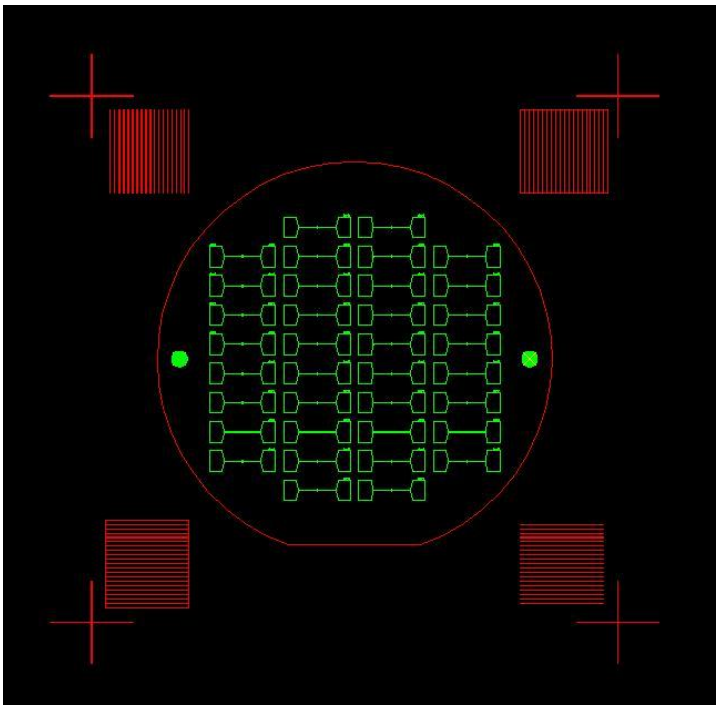

Figure 3.1: Autodesk AutoCAD drawing of individual silicon chips on a silicon wafer.

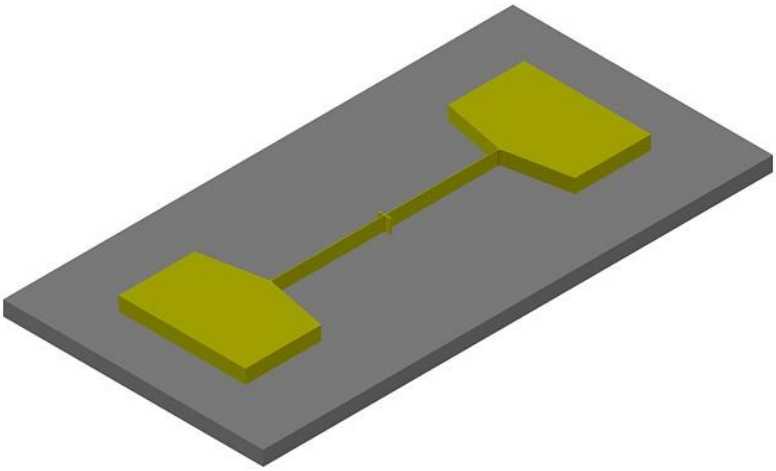

Figure 3.2: AutoCAD drawing depicting a single silicon chip with gold electrode on top.

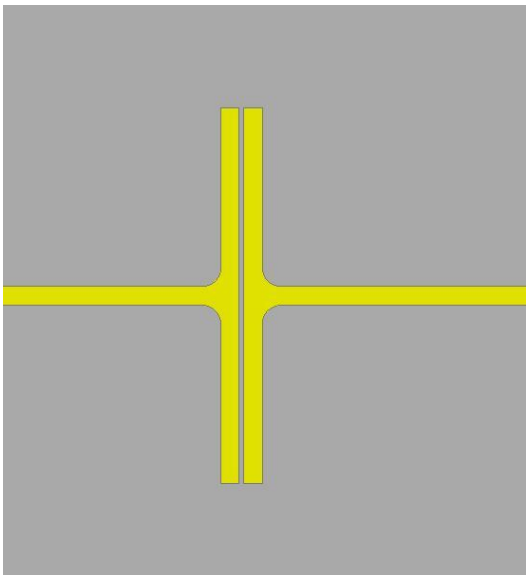

Figure 3.3: AutoCAD drawing depicting a 6 micron gap between gold electrodes on a single silicon chip.

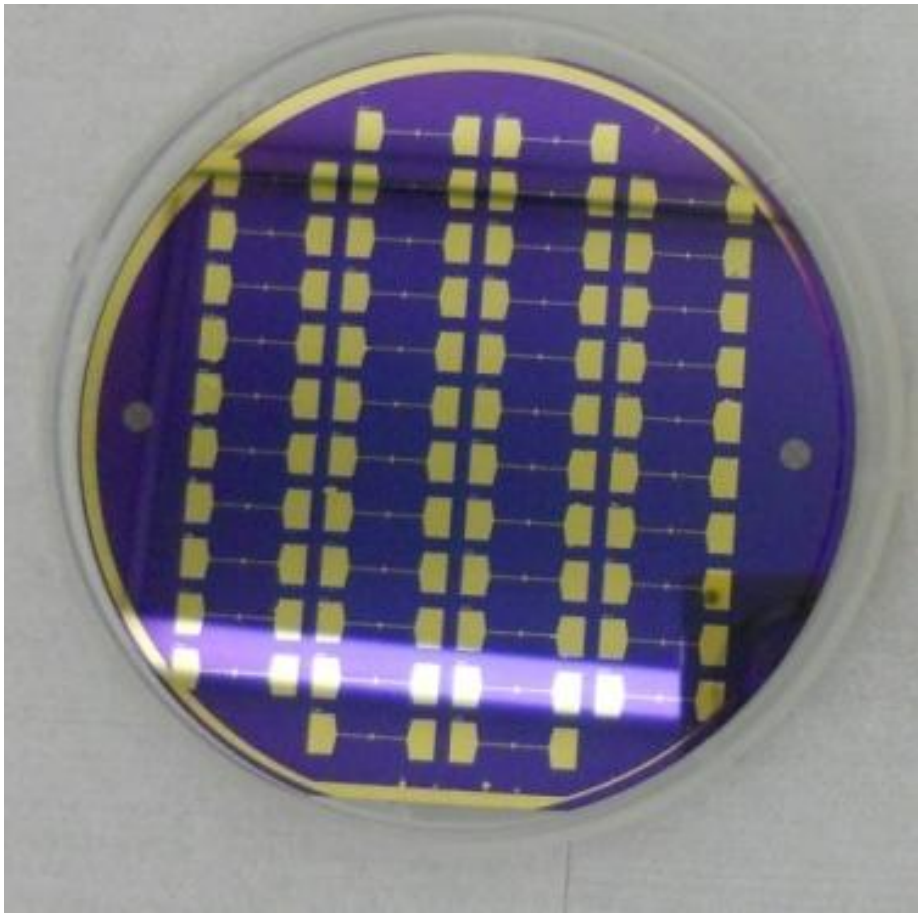

Figure 3.4: Picture showing many silicon chips on a single wafer after fabrication processes.

3.5 References

1. Deal, B. E.; Grove, A. S., General Relationship for the Thermal Oxidation of Silicon. *Journal of Applied Physics* **1965,** *36* (12), 3770-3778.
2. Madou, M. J., Fundamental of Microfabrication: The Science of Miniaturization. **2002**.

Chapter 4: Non-Thermal Current Stimulated Desorption Of Gases from Carbon Nanotubes

The desorption of gases from carbon nanotubes is usually a slow process that limits the nanotubes' utility as sensors or as memristors. Here we demonstrate that flow in the nanotube above the Poole-Frenkel conduction threshold can stimulate adsorbates to desorb without heating the sensor significantly. The method is general: alcohols, aromatics, amines and phosphonates were all found to desorb. We postulate that the process is analogous to electron stimulated desorption, but with an internally conducted rather than externally applied source of electrons. This chapter is the expanded version of an already published paper: A. Salehi-Khojin, Kevin Y. Lin, C.R. Field, R.I. Masel. "Nonthermal Current-Stimulated Desorption of Gases from Carbon Nanotubes." *Science* 2010, 329, 1327-1330.

4.1 Introduction

Single walled carbon nanotubes (SWNT) have been proposed for a wide range of applications[1-5], including as sensors for a variety of gases, or as a component in nanotube based electronics. In general SWNT based sensors have the key advantages of low power, high sensitivity, and very small size[5].

Figure 4.1 shows a diagram of our nanotube sensors. They consist of a nanotube network between two gold contacts. They are of a standard design, except that we use defected nanotubes to enhance sensitivity[6]. Our fabrication procedure also gives unusually small contact impedances[6, 7].

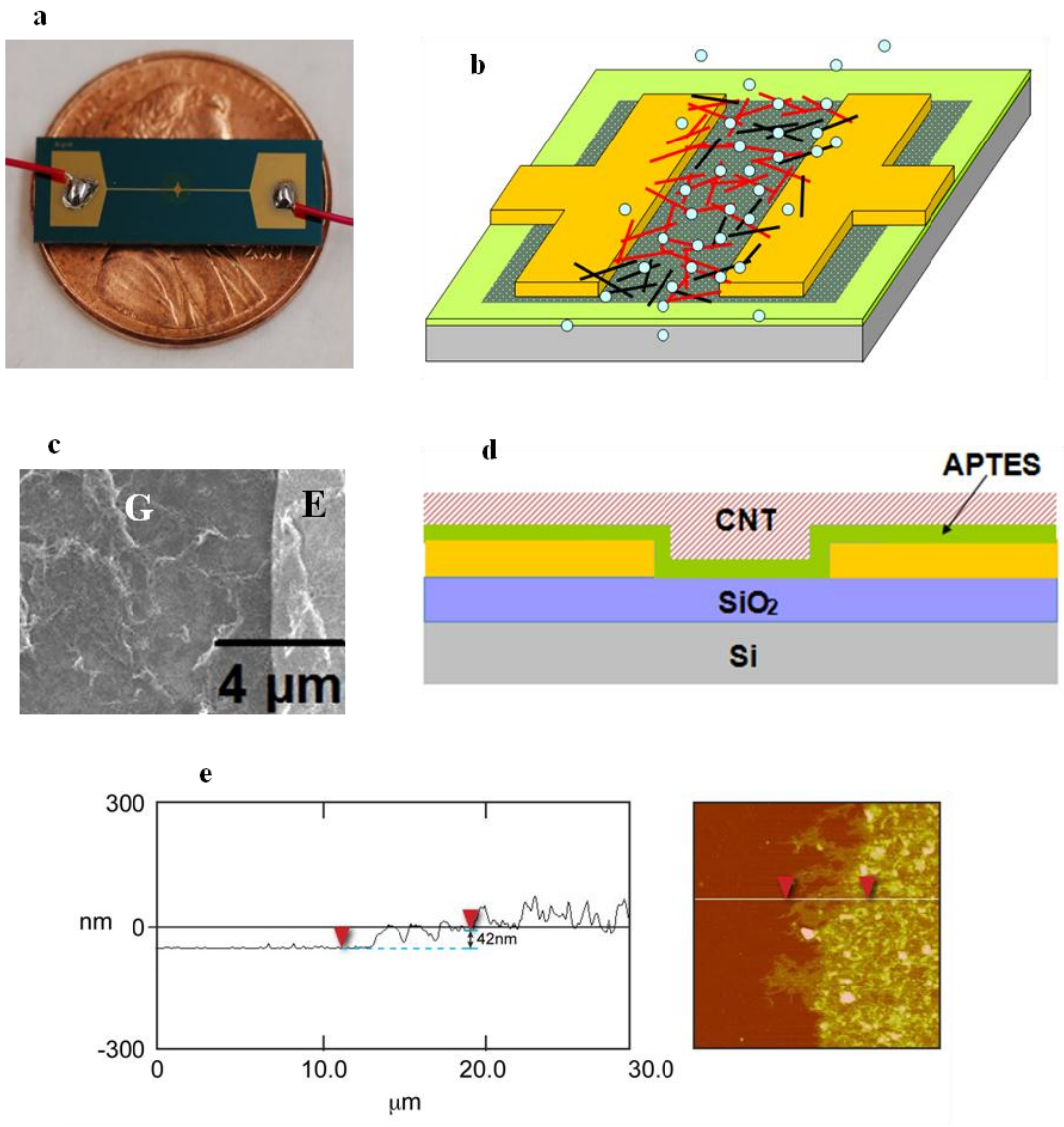

Figure 4.1: (A) Typical fabricated nanotube sensors using lift-off photolithography on a Si/SiO2 substrate. (B) Schematic of nanotube sensor. (C) SEM images of nanotube film (The gap zone and electrodes are labeled (G) and (E) in the SEM images, respectively). (D) The cross section of fabricated nanotube sensors. (E) A typical AFM characterization for nanotube sensor shows an average thickness of approximately 42 nm.

One of the challenges in SWNT-based sensor design is the slow recovery of the nanotube resistance after gases adsorb. Figure 4.2 shows the response of a typical bare nanotube sensor to a 100 millisecond pulse containing 10^{17} molecules of toluene in helium at 24 °C. Notice, the sensor shows an immediate step change in voltage. There is also an initial peak superimposed on the step. The step never recovers, even after a nearly 1 hour waiting period.

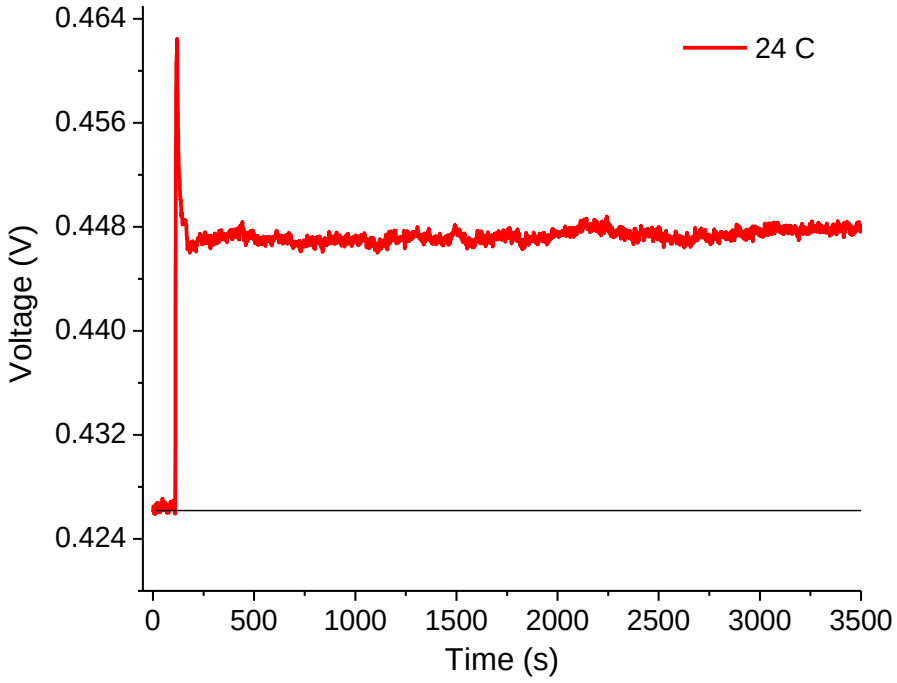

Figure 4.2: Shows typical response of a carbon nanotube sensor to toluene molecules. These were measured by applying 50 µA to the sensors and measuring the voltage drop across the sensors as a function of time. The response consists of two components a sharp peak and a step change.

Physically, toluene exhibits multiple binding modes at different sites on the carbon nanotubes[8]. Some of the molecules are irreversibly adsorbed at room temperature, where as others are only weakly bound. We attribute the step change in voltage to the toluene that

irreversibly adsorbs on the SWNTs. Such a step change could also in principle occur because of changes to contact impedance at the gold-nanotube contacts, but in our sensors the impedance is less than 0.002V[6] and does not change measurably when gas adsorbs or when a 12V potential is applied to the sensor. This step behavior is a hindrance to reuse of SWNT sensors. There are reports of accelerated recovery for a given class of molecules upon coating the sensor with polymers[9], but then other molecules irreversibly adsorb, and decrease sensitivity.

4.2 Objective

Here we demonstrate the removal of gases from nanotubes via a distinct process that we have termed current stimulated desorption (CSD). In CSD, a current applied through the sensor stimulates molecular desorption. Electron stimulated desorption (ESD) is a well known related process, but has only been demonstrated with an external source of electrons or photons [10-15].

This discovery arose through our study of the influence of electron transport mode on the performance of nanotube sensors [6]. Three main mechanisms of electron transport in nanotubes have been established: quantum tunneling [16-18], Schottky-Richardson conduction[19-22], and Poole-Frenkel conduction[23-27]. At low electric fields, quantum tunneling dominates. Electrons travel by tunneling between quantum states in the nanotube. Currents are small, but resistances are too. Increasing the electric field leads to Schottky-Richardson (S-R) conduction [19-22], in which transport occurs mainly within the conduction band of the nanotube. At higher voltages/currents, a third transport mechanism, called Poole-Frenkel (P-F) conduction, begins to dominate[23-27]. In this regime, electrons jump over defects in the surface of the nanotubes due to high local electric

fields and then continue along the nanotube. Electrons can also skip between molecules adsorbed onto a nanotube.

Our objective was to see if Poole-Frenkel conduction could be used to stimulate molecules to desorb. Madey and Yates [10, 13] demonstrated that desorption can be induced by electronic excitations of an adsorbate, at energies of 2 to 5 eV. There are also reports of photodesorption of molecules from carbon nanotubes [28-33]. Generally a 2 or 3 eV photon is sufficient to desorb molecules from surfaces although there is one case where a 1.2 eV photon was sufficient [33]. One can also get desorption if one excites the molecule vibrationally so it enters a repulsive state. Poole-Frankel conduction operates in a comparable energy regime, so seemed a plausible alternative.

4.3 Experimental Procedures

Fabrication and design of the sensor. Carbon nanotube sensors were fabricated using standard lift-off photolithography. A silicon substrate with a thermal oxide layer (500/0.5 µm Si/SiO_2) was patterned with chromium and gold (10/100 nm Cr/Au) for source and drain electrodes separated by a 6 µm gap. 1% 3-aminopropyltriethoxysilane (APTES) (Gelest, Inc) was utilized as a supportive coating to enhance the interaction between the SWNT film and the silicon substrate as described in detail elsewhere.

SWNT preparation and deposition on silicon substrate. A highly concentrated SWNT suspension (400 mg/L) was made from 10 mg of SWNT powder (Unidym, High Purity HIPCO) (Figure 4.3) and 1% (w/v) sodium dodecyl sulfate (SDS) in water. Multiple sets of 10-minute, low-powered ultrasonication (at 40% power and 90% frequency), 1-hour stirring and 3-hours

centrifugation (at 2800 g or 4100 RPM) were performed to homogenize and uniformly disperse the suspension (Figure 4.4). The highly concentrated, homogeneous SWNT suspension was then diluted to 3 mg/L in 25 mL solution before being vacuum filtered with mixed cellulose ester (MCE) membranes (Millipore, 0.22 micron pore size) (Figure 4.5). After the SWNT was successfully deposited onto the membranes, the wet MCE-SWNT membrane was dried out for at least 2 hours under a vacuum of 381 mm mercury (50796 pa) before multiple rinsing with approximately 80 mL of purified and deionized water (Millipore, MilliQ water). Multiple rinsing was intended to completely remove the SDS residue from the MCE-SWNT membrane. Finally, a stamp technique was used to transfer homogeneous, randomly aligned CNT films to the APTES treated silicon surface.

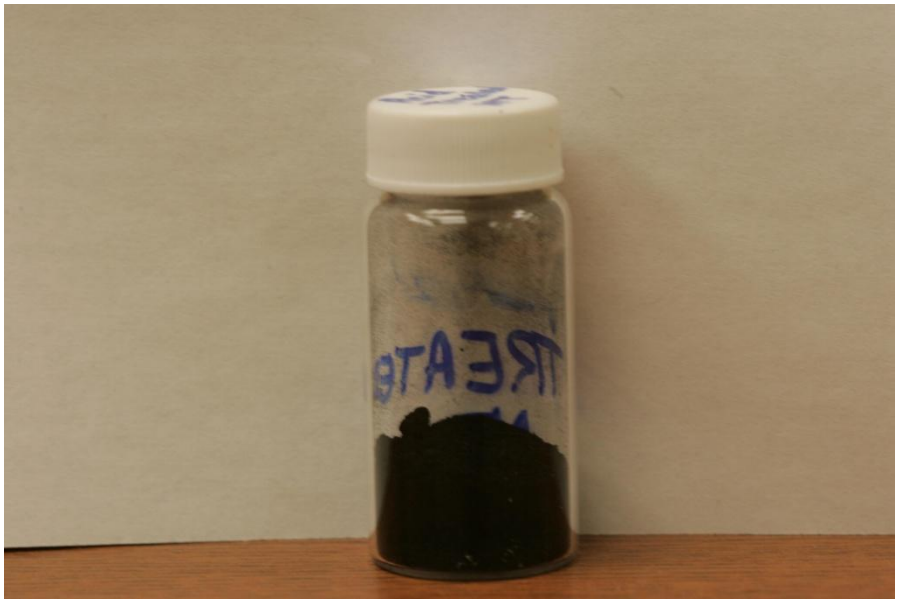

Figure 4.3: Photograph showing the starting material single-walled carbon nanotubes.

Figure 4.4: Photograph showing the vial of dispersion of single-walled carbon nanotubes in 1% SDS-water solution after centrifuge and decanting.

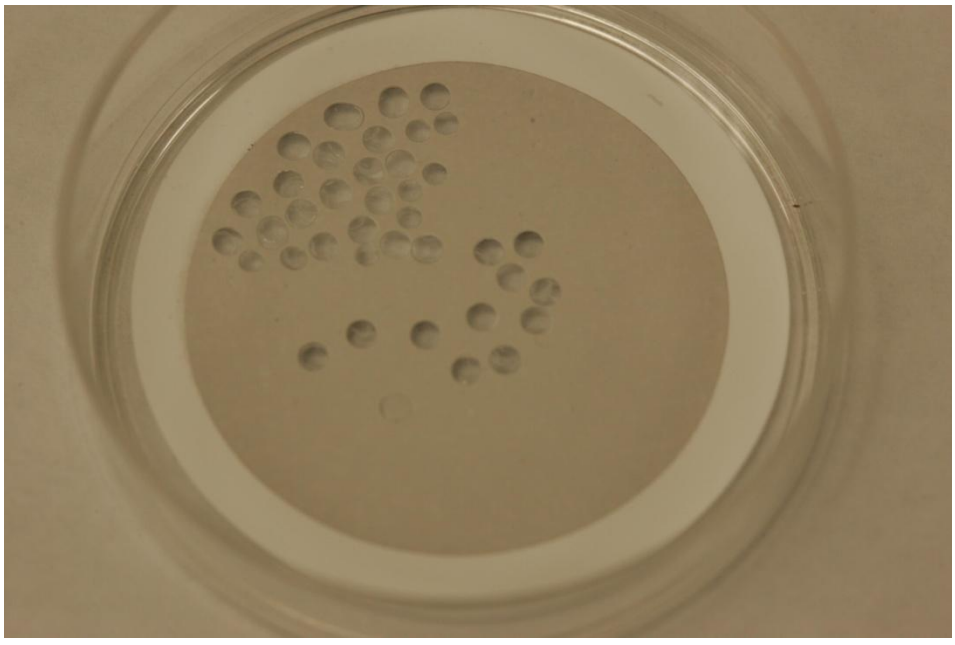

Figure 4.5: Photograph showing the randomly aligned single-walled carbon nanotube film.

Sensor testing and measurement. Sensors were placed in a custom built PEEK (polyaryletheretherketone) flow cell and a fused silica passivated capillary was used to connect to a Gas Chromatograph (GC) inlet. An Agilent 6893N GC/FID-MS with 7683B auto-sampler with a pulse of 100 ms was used to deliver target gas molecules to the sensors at pressure of 3.6 psi for all experiments. Ultra pure helium gas was used as a carrier gas at fixed flow rate. We heated the sensors either in a GC oven or in a heated box. The latter gave more stable behavior. VoltaLab 10 potentiostat (PGZ100) was used to monitor the change in potential on the CNT sensors upon exposure to trace gas vapors.

Infrared Temperature Measurement. Measurements of the temperature rise were made using a QFI InfraScope II thermal mapping system with a resolution of 0.5°C and working distance of 1.5 cm with 15×objective. The nanotube array was opened for these measurements and there was no gas flowing. At zero current a radiance reference image was acquired at the base temperature. The thermal images of the sensor were then taken under various applied currents up to 3 mA. We used a stage temperature of 84°C based on QFI (quantum Focus Instruments Corporation) recommendation for back stage temperature of metal electrodes (80-90°C for Au).

4.4 Results on Current-Stimulated Desorption Process

To test this hypothesis, we applied varied current and then measured desorption, via recovery of the nanotube sensor after exposure to a pulse of gas [6]. We chose this method because the adsorbate layers are too unstable to be probed by electron spectroscopy and adsorbate coverages were too low for optical probes.

In Figure 4.6, the current induced voltage was too low to stimulate significant Poole-Frenkel conduction[6]. In Figure 4.7, there is some Poole-Frenkel conduction, but insufficient voltage to excite electronic transitions. Figure 4.8 is an intermediate case, where voltages (3.77V) are just above the threshold for electronic transitions, and in Figure 4.9 there is substantial Poole-Frankel conduction and the voltages (>12V) are high enough to desorb many molecules. The sensor shows an irreversible response in Figures 4.6 and 4.7, some recovery in 4.8, and complete recovery in Figure 4.9. Finally, Figure 4.10 demonstrates that CSD can be effectively applied 3 hours after the initial exposure and return the sensor rapidly to baseline.

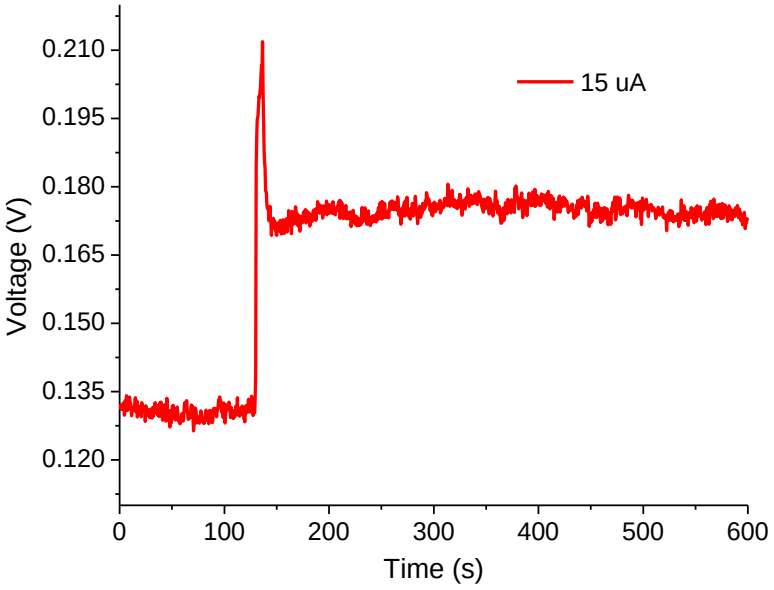

Figure 4.6: The response of carbon nanotube sensor to toluene molecules at applied 15 µA currents at 24 °C. At low currents, there are two parts to the response; a rapidly changing part of the response, and a part that takes hours or days to recover.

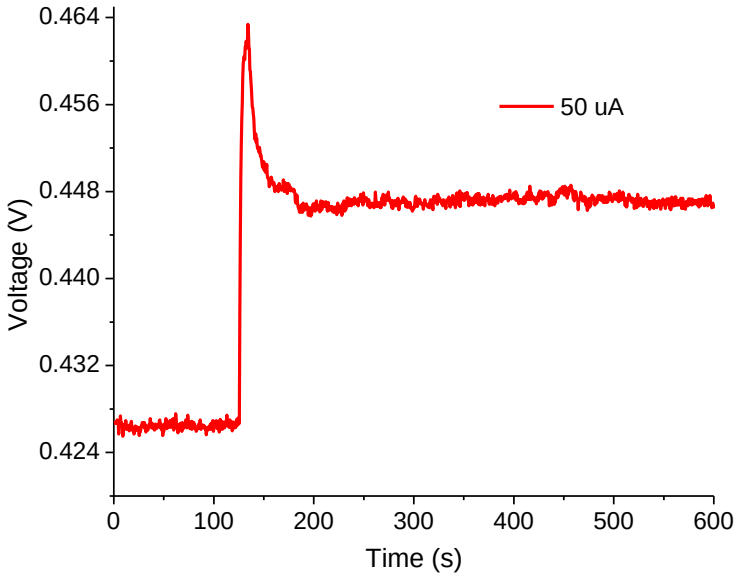

Figure 4.7: The response of carbon nanotube sensor to toluene molecules at applied 50 µA currents at 24 °C. At low currents, there are two parts to the response; a rapidly changing part of the response, and a part that takes hours or days to recover.

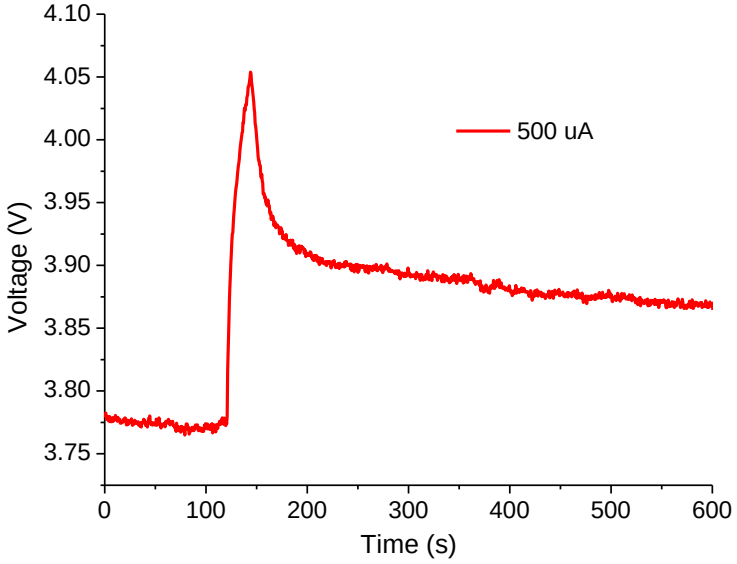

Figure 4.8: The response of carbon nanotube sensor to toluene molecules at applied 500 µA currents at 24 °C. Partial recovery is observed.

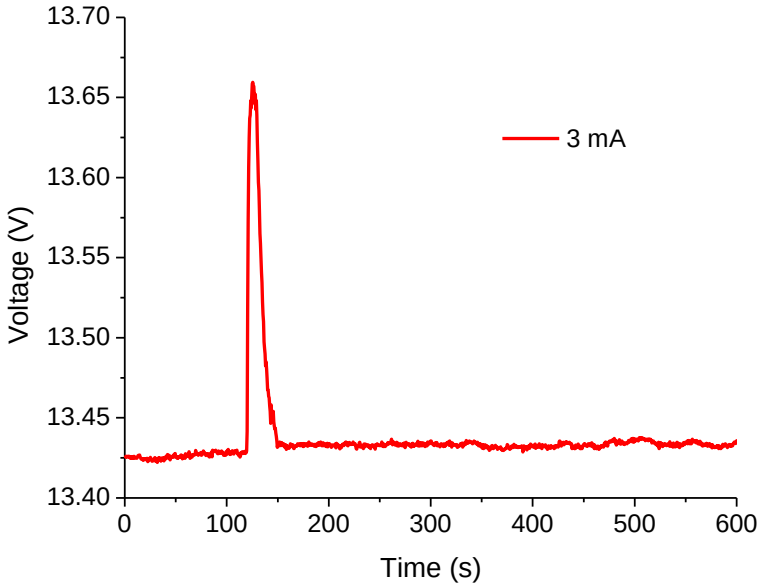

Figure 4.9: The response of carbon nanotube sensor to toluene molecules at applied 3 mA currents at 24 °C. As the current through the carbon nanotube rises to a point where Poole-Frenkel conduction is expected, the recovery speeds up so it takes about 10s of seconds for the response to recover.

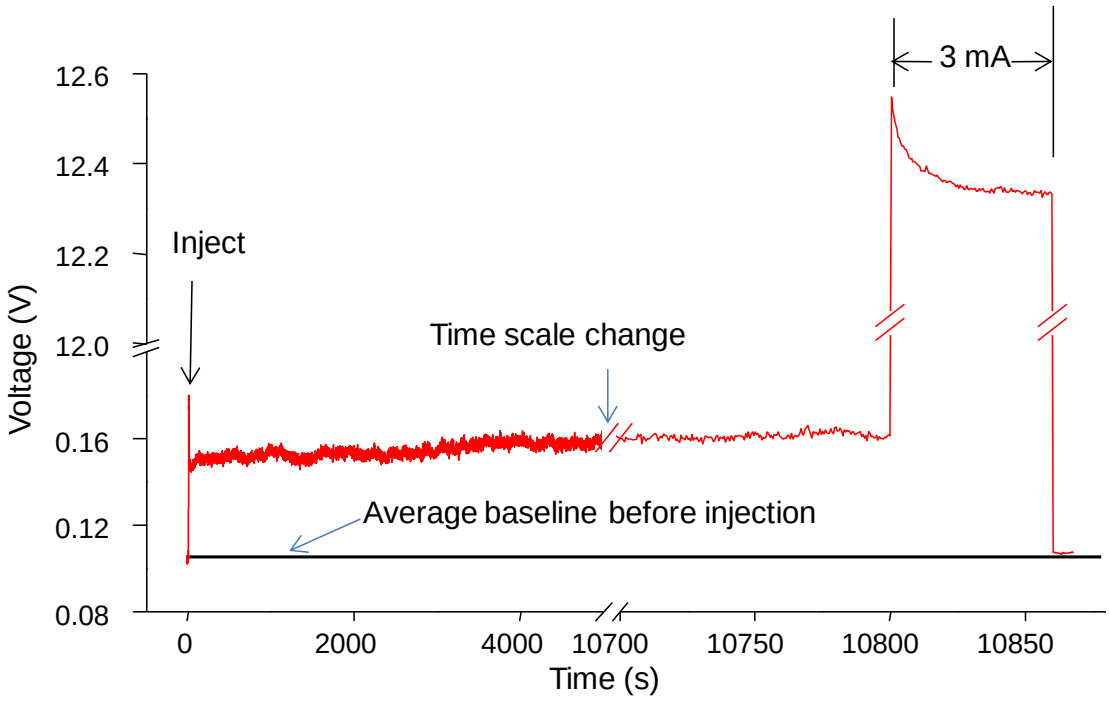

Figure 4.10: A test where toluene is injected and a 15 µA current is maintained for 10800 seconds (3 hours) then the current is raised to 3 mA for 60 seconds and then the current is lowered to 15 µA again. The horizontal line in the figure is the average baseline before the process starts. Notice that current almost completely recovers. Note: there is a horizontal scale change in this graph before 10700 seconds.

We have reproduced these results with more than ten different sensors. All show the same slow recovery at low currents and fast response at high currents. We have also observed the effect with a number of other gases. We have demonstrated the effect with methanol, ethanol, 1-propanol, 1-butanol, isopentanol, 1-hexanol, 1-heptanol, dimethyl methylphosphonate (DMMP), tributylphosphate (TBP) and 1,2-dichlorobenzene. The TBP results were notable because TBP has a vapor pressure of less than 0.1 mm Hg, thus CSD is able to remove involatile molecules from the nanotubes.

4.5 Effects of Heating from CSD process

Of course one has to carefully consider how heating of the nanotubes may have affected the results in Figures 4.6 to 4.10. The experiments reported here were designed to minimize heating during the experiment. First, our sample preparation procedure was previously shown to minimize contact resistance, thereby minimizing heating at the contacts [6]. Sensors were also fabricated on a silicon wafer with a monolayer of 3-aminopropyltriethoxysilane (APTES) applied to improve the thermal contact between the nanotubes and the silicon. Silicon's high thermal conductivity served to further minimize heating of the nanotubes. Calculations indicate that the temperature of the nanotubes should not have risen substantially under these conditions[34-36].

We also conducted two different experiments to measure the temperature change. First, an infrared imager was used to detect any local temperature rise in the nanotube sensor as current was applied. Figure 4.11 shows the results. The infrared measurements indicated a less than 4°C temperature rise at the highest currents explored here, and negligible rises at lower currents. An Infrascope II, thermal imaging system was used to get a measure of the temperature rise of the sensors. The sensor was mounted in the Infrascope, current was allied with no gas flow, and thermal images were taken. Figure 4.11 shows an image taken at an applied current of 3 mA with no air flow over the sensor. The image shows that the temperature at the center of the nanotube sensor increases by about 3 °C when the 3 mA is applied. One needs to be careful with this measurement, because the nanotubes are transparent in the IR, and so the image is really measuring the temperature of the silicon directly under the nanotube.

One can use a heat balance to estimate the true temperature rise of the nanotubes (Figure 4.12). We calculated thermal resistance: (i) nanotube-SiO_2 interface based on reported thermal contact resistance per unit area of 1-2×10^{-8} m^2K/W;[37] (ii) the SiO_2 layer from $R_{SiO2}=B/(k_{SiO2}WL)$ where k_{SiO2} =1.4 $Wm^{-1}K^{-1}$ and B,W,L are thickness, width and length of SiO_2 layer under nanotube film;[38] and (iii) Si substrate from $R_{Si}=1/(2k_{Si}(WL)^{1/2})$ where k_{Si}=50 $Wm^{-1}K^{-1}$.[39] The corresponding thermal resistances were calculated as 1.6 K/W, 71 K/W and 129 K/W, respectively. Due to negligible thermal resistance in nanotube-SiO_2 interface, we can express the ratio of relative temperature rise in SiO_2 layer over that of Si substrate (in the circuit shown above) as $(T_{CNT}-T_{Si})/T_{Si}=R_{SiO2}/R_{Si}$. This calculation estimates the ratio of temperature rise of nanotube film over Si to be 1.55, and predicts a 3°C temperature rise in nanotube film when 3 mA was applied to the sensor.

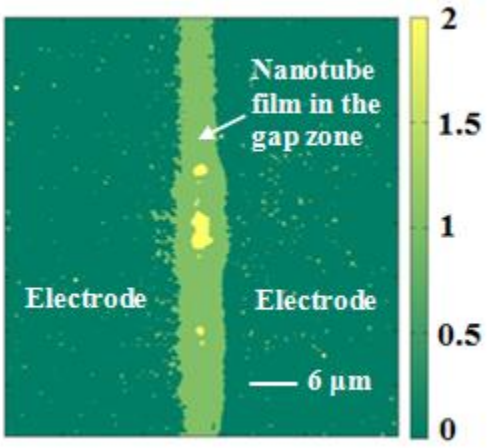

Figure 4.11: Infrared (IR) microscopy image of carbon nanotube sensor at a current of 3 mA.

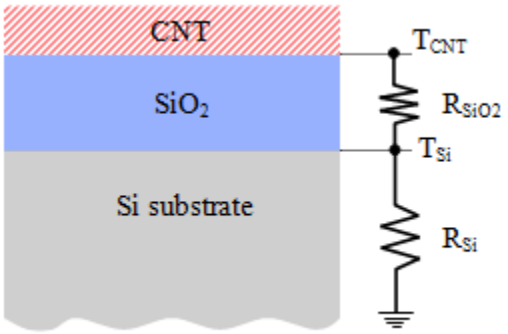

Figure 4.12: Equivalent thermal circuit for carbon nanotube sensor.

Second, Raman spectroscopy was used to confirm the lack of a temperature rise. Zhou et al.[40] showed that the intensity of the G and D bands of the nanotube spectrum are sensitive to temperature, we did not observe any intensity changes or wavelength shifts of the G and D bands as the current was raised (Figure 4.13). The intensity of the G and D bands should decrease by 0.5%/K between 300 and 400 K, while the position of the bands should shift by 0.015 cm^{-1}/K. Figure 4.13 shows the data. Experimentally, the peak intensities are within 1% of each other at all currents. The peak maxima are all within 0.2 cm^{-1} of each other (our measurement limit). Based on the intensity data we can conclude that the average temperature of the nanotubes does not rise more than 2 °C. The peak position place an upper bound on the temperature rise of 13 °C.

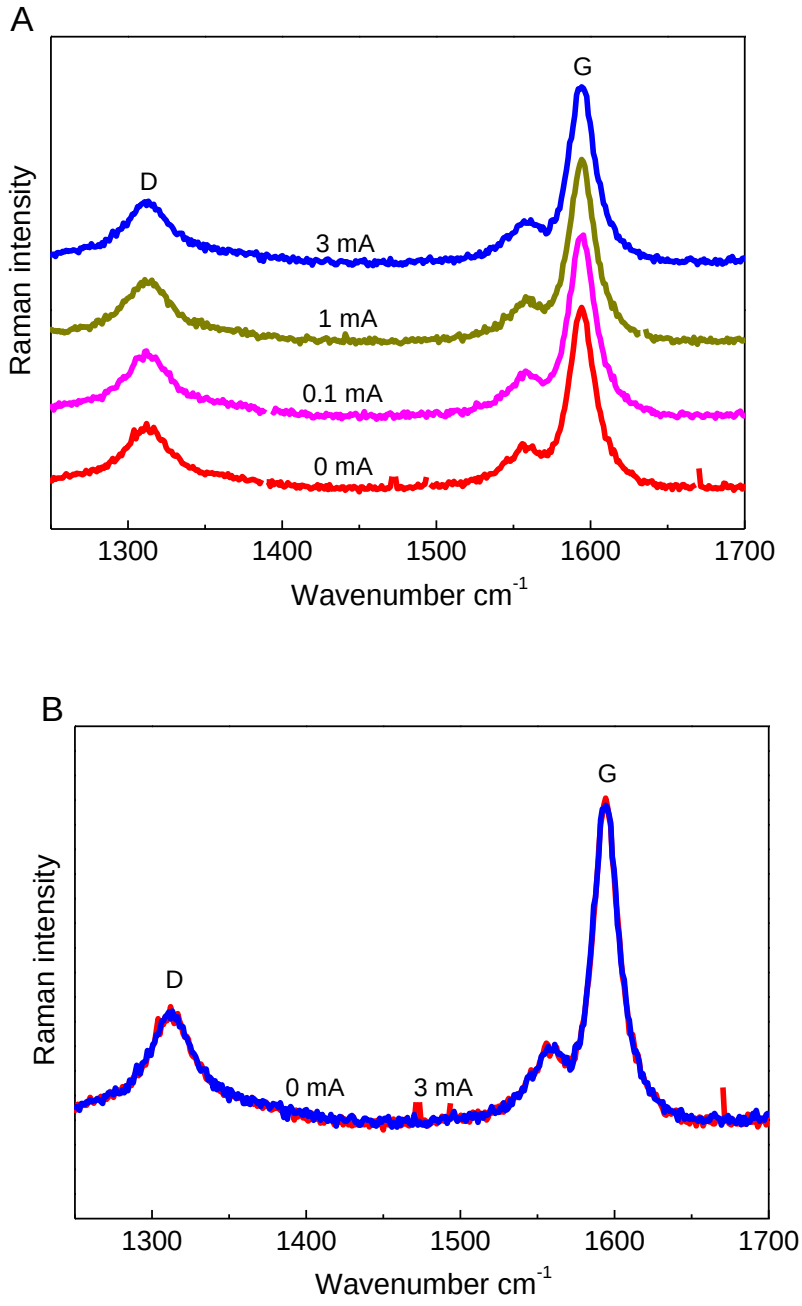

Figure 4.13: (A) The Raman spectra of our sensors at different applied currents. (B) the 0 mA and 3 mA curves overlaid.

4.6 Thermal Experiments on Carbon Nanotube Sensors

Next we performed experiments to see if a 13°C change in the nanotubes could cause an observable change in sensor recovery rate. Figure 4.14 shows how the sensor response varied as the temperature was raised from 24°C to 115°C. Increasing the temperature up to 80°C raises the baseline, since the resistance of the sensor increases with temperature, (changes in resistance cause voltage changes in constant current measurements), but there is still an irreversible component of the response. In addition, the sensor shows slow degradation, as indicated by the slope of the plot. The irreversible component of the response disappears when the sensor degrades severely, as manifested by the continuously rising baseline. The stability of the baseline in Figure 4.9 clearly shows that simply applying a current of 3 mA does not induce such thermal behavior. We were never able to reproduce the CSD response by heating the sensor to any temperature.

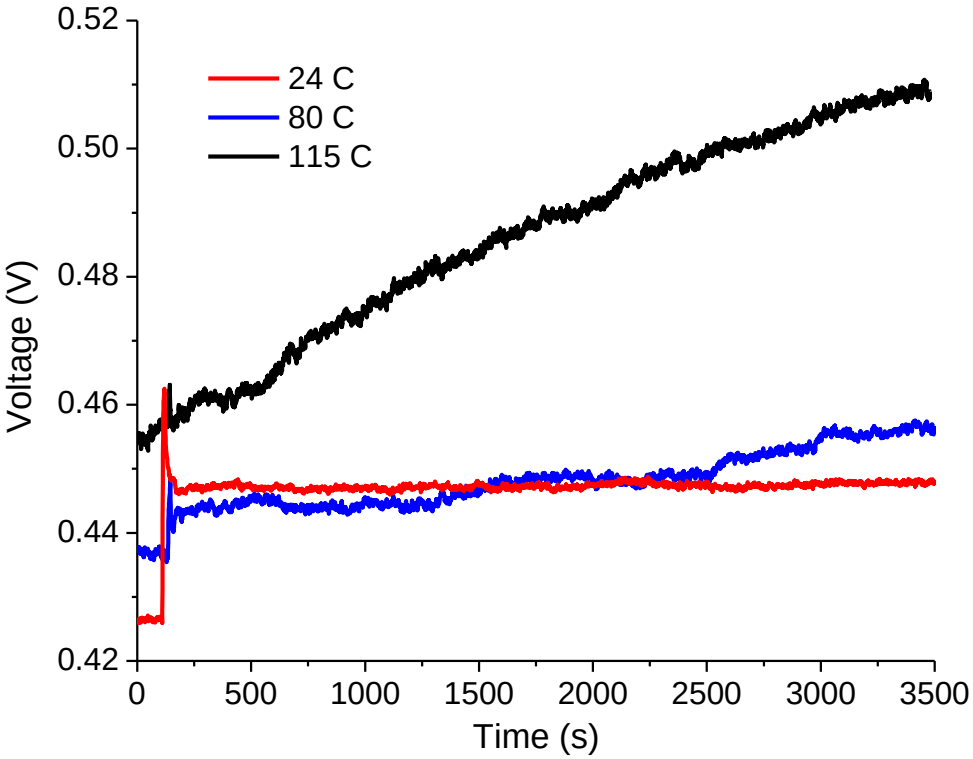

Figure 4.14: Typical response of a cabon nanotubes sensor to toluene molecules, measured by applying 50 µA to the sensors and measuring the voltage drop across them as a function of time. Even at 80°C the voltage does not return to baseline after 3500 seconds. The response does recover at 115 °C, but the sensor quickly degrades at that temperature. The degradation causes the slope shown in the figure. An expanded view of the data is shown in Figure 4.15.

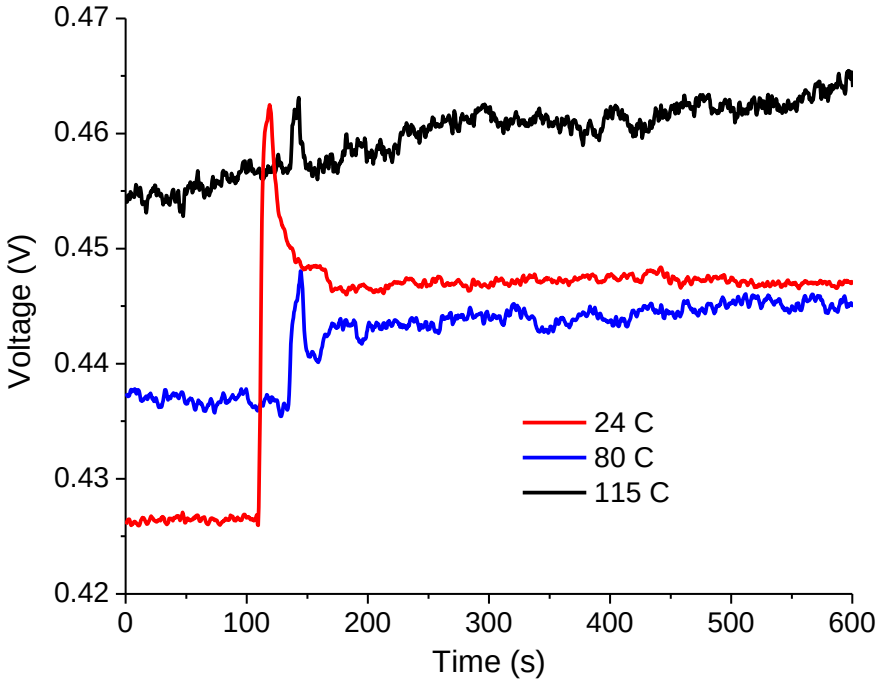

Figure 4.15: Expanded results of Figure 4.14. The peak for 24℃ was slightly shifted to the left to avoid overlapping of peaks.

4.7 Conclusion

Furthermore, local temperature changes greater than 80^{o}C can be ruled out. Kumar et al. have shown with thorough calculations [36] that the thermal conductivity of SWNTs is sufficiently high to quickly dissipate a 50°C temperature gradient across the length of our sensors. Thus, if there were a hot spot created in the sensor, an extensive portion of the sensor would heat up, a result not supported by the infrared imaging and spectroscopic data.

Finally desorption is not a local phenomenon in our data. If molecules were being thermally desorbed only from small regions of the nanotube network, then only those areas would manifest fast recovery, while the rest of the sensor recovered slowly. We observe fast

recovery over the entire sensor, implying that desorption is occurring over the entire surface of the network, and could not be associated with local hot spots.

Consequently, we conclude that the accelerated recovery time observed in Figure 4.9 is not due to heating of the nanotubes. Instead, it must be due to a non-thermal process whereby the analyte is removed from the nanotube surface in response to the current.

4.8 References

1. Snow, E. S.; Perkins, F. K.; Houser, E. J.; Badescu, S. C.; Reinecke, T. L., Chemical Detection with a Single-Walled Carbon Nanotube Capacitor. *Science* **2005,** *307* (5717), 1942-1945.
2. Robinson, J. A.; Snow, E. S.; BÇŽdescu, Å. C.; Reinecke, T. L.; Perkins, F. K., Role of Defects in Single-Walled Carbon Nanotube Chemical Sensors. *Nano Lett.* **2006,** *6* (8), 1747-1751.
3. Kong, J.; Franklin, N. R.; Zhou, C.; Chapline, M. G.; Peng, S.; Cho, K.; Dai, H., Nanotube Molecular Wires as Chemical Sensors. *Science* **2000,** *287* (5453), 622-625.
4. Bondavalli, P.; Legagneux, P.; Pribat, D., Carbon Nanotubes Based Transistors as Gas Sensors: State of the Art and Critical Review. *Sens. Actuators, B* **2009,** *B140* (1), 304-318.
5. Goldoni, A.; Petaccia, L.; Lizzit, S.; Larciprete, R., Sensing Gases with Carbon Nanotubes: A Review of the Actual Situation. *J. Phys.: Condens. Matter* **2010,** *22* (1), 013001/1-013001/8.

6. Salehi-Khojin, A.; Field, C. R.; Yeom, J.; Shannon, M. A.; Masel, R. I., Sensitivity of Nanotube Chemical Sensors at the Onset of Poole-Frenkel Conduction *Appl. Phys. Lett.* **2010,** *96*, 163110-163113.

7. Field, C. R.; Yeom, J.; Salehi-Khojin, A.; Masel, R. I., Robust Fabrication of Selective and Reversible Polymer Coated Carbon Nanotube-Based Gas Sensors. *Sens. Actuators, B* **2010,** *148* (1), 315-322.

8. Agnihotri, S.; Rood, M. J.; Rostam-Abadi, M., Adsorption Equilibrium of Organic Vapors on Single-Walled Carbon Nanotubes. *Carbon* **2005,** *43* (11), 2379-2388.

9. Lee, Chang Y.; Sharma, R.; Radadia, Adarsh D.; Masel, Richard I.; Strano, Michael S., On-Chip Micro Gas Chromatograph Enabled by a Noncovalently Functionalized Single-Walled Carbon Nanotube Sensor Array13. *Angewandte Chemie* **2008,** *120* (27), 5096-5099.

10. Madey, T. E.; Yates, J. T., Electron-Stimulated Desorption as a Tool for Studies of Chemisorption - Review. *Journal of Vacuum Science & Technology* **1971,** *8* (4), 525-&.

11. Ramsier, R. D.; Yates, J. T., Electron-Stimulated Desorption - Principles and Applications. *Surface Science Reports* **1991,** *12* (6-8), 243-378.

12. Sanche, L., Electronic Aging and Related Electron Interactions in Thin-Film Dielectrics. *IEEE transactions on electrical insulation* **1993,** *28* (5), 789-819.

13. Madey, T. E., History of Desorption Induced by Electronic-Transitions. *Surface Science* **1994,** *299* (1-3), 824-836.

14. Bass, A. D.; Sanche, L., Reactions Induced by Low Energy Electrons in Cryogenic Films (Review). *Low Temperature Physics* **2003,** *29* (3), 202-214.

15. Menzel, D., Electronically Induced Surface Chemistry: Localised Bond Breaking Versus Delocalisation. *Surface and Interface Analysis* **2006,** *38* (12-13), 1702-1711.

16. Kim, D.-H.; Huang, J.; Shin, H.-K.; Roy, S.; Choi, W., Transport Phenomena and Conduction Mechanism of Single-Walled Carbon Nanotubes (Swnts) at Y- and Crossed-Junctions. *Nano Lett.* **2006,** *6* (12), 2821-2825.

17. Lee, K. U.; Cho, Y. H.; Petty, M. C.; Ahn, B. T., Electrical Conductivity of Single-Wall Carbon Nanotube Film Deposited by Electrostatic Layer-by-Layer Assembly with the Aid of Polyelectrolytes. *Carbon* **2009,** *47* (2), 475-481.

18. Ounaies, Z.; Park, C.; Wise, K. E.; Siochi, E. J.; Harrison, J. S., Electrical Properties of Single Wall Carbon Nanotube Reinforced Polyimide Composites. *Composites Science and Technology* **2003,** *63* (11), 1637-1646.

19. Behnam, A.; Johnson, J. L.; Choi, Y.; Ertosun, M. G.; Okyay, A. K.; Kapur, P.; Saraswat, K. C.; Ural, A., Experimental Characterization of Single-Walled Carbon Nanotube Film-Si Schottky Contacts Using Metal-Semiconductor-Metal Structures. *Appl. Phys. Lett.* **2008,** *92* (24), 243116/1-243116/3.

20. Peng, N.; Zhang, Q.; Chow, C. L.; Tan, O. K.; Marzari, N., Sensing Mechanisms for Carbon Nanotube Based Nh3 Gas Detection. *Nano Lett.* **2009,** *9* (4), 1626-1630.

21. Suehiro, J.; Imakiire, H.; Hidaka, S.-i.; Ding, W.; Zhou, G.; Imasaka, K.; Hara, M., Schottky-Type Response of Carbon Nanotube No2 Gas Sensor Fabricated onto Aluminum Electrodes by Dielectrophoresis. *Sens. Actuators, B* **2006,** *B114* (2), 943-949.

22. Yamada, T., Equivalent Circuit Model for Carbon Nanotube Schottky Barrier: Influence of Neutral Polarized Gas Molecules. *Appl. Phys. Lett.* **2006,** *88* (8), 083106/1-083106/3.

23. Perello, D.; Yu, W.-J.; Bae, D.-J.; Chae, S.-J.; Kim, M.-J.; Lee, Y.-H.; Yun, M.-H., Pool-Frenkel Emission and Hopping Conduction in Semiconducting Carbon Nanotube Transistor. *Proc. SPIE* **2009,** *7399* (Carbon Nanotubes, Graphene, and Associated Devices II), 739907/1-739907/6.

24. Perello, D. J.; Yu, W. J.; Bae, D. J.; Chae, S. J.; Kim, M. J.; Lee, Y. H.; Yun, M., Analysis of Hopping Conduction in Semiconducting and Metallic Carbon Nanotube Devices. *J. Appl. Phys.* **2009,** *105* (12), 124309/1-124309/5.

25. Venet, C.; Pearson, C.; Jombert, A. S.; Mabrook, M. F.; Zeze, D. A.; Petty, M. C., The Morphology and Electrical Conductivity of Single-Wall Carbon Nanotube Thin Films Prepared by the Langmuir-Blodgett Technique. *Colloids Surf., A* **2010,** *354* (1-3), 113-117.

26. Jombert, A. S.; Coleman, K. S.; Wood, D.; Petty, M. C.; Zeze, D. A., Poole-Frenkel Conduction in Single Wall Carbon Nanotube Composite Films Built up by Electrostatic Layer-by-Layer Deposition. *J. Appl. Phys.* **2008,** *104* (9), 094503/1-094503/7.

27. Mabrook, M. F.; Pearson, C.; Jombert, A. S.; Zeze, D. A.; Petty, M. C., The Morphology, Electrical Conductivity and Vapour Sensing Ability of Inkjet-Printed Thin Films of Single-Wall Carbon Nanotubes. *Carbon* **2009,** *47* (3), 752-757.

28. Chen, R. J.; Franklin, N. R.; Kong, J.; Cao, J.; Tombler, T. W.; Zhang, Y.; Dai, H., Molecular Photodesorption from Single-Walled Carbon Nanotubes. *Appl. Phys. Lett.* **2001,** *79* (14), 2258-2260.

29. Miyamoto, Y.; Jinbo, N.; Nakamura, H.; Rubio, A.; Tomanek, D., Photodesorption of Oxygen from Carbon Nanotubes. *Phys. Rev. B: Condens. Matter Mater. Phys.* **2004,** *70* (23), 233408/1-233408/4.

30. Shim, M.; Siddons, G. P.; Jeong, J. K.; Merchin, D., Photo- and Thermal Annealing-Induced Processes in Carbon Nanotube Transistors. *Mater. Res. Soc. Symp. Proc.* **2004,** *789* (Quantum Dots, Nanoparticles and Nanowires), 397-402.

31. Karthigeyan, A.; Minami, N.; Iakoubovskii, K., Highly Sensitive, Room-Temperature Gas Sensors Prepared from Cellulose Derivative Assisted Dispersions of Single-Wall Carbon Nanotubes. *Jpn. J. Appl. Phys.* **2008,** *47* (9, Pt. 1), 7440-7443.

32. Liu, Z.; Liu, G.; Zhao, Y.; Zheng, K.; Huang, H.; Yang, Y.; Wang, C.; Gu, C.; Xie, S.; Sun, L., Oxygen Desorption from Single-Walled Carbon Nanotubes by Camera Flash. *J. Nanosci. Nanotechnol.* **2009,** *9* (2), 1354-1356.

33. Nanjo, D.; Shibamoto, K.; Korenaga, T., Visible and near-Infrared Laser Desorption Ionization Mass Spectrometry Using Single Wall Carbon Nanotubes. *Chem. Lett.* **2009,** *38* (2), 142-143.

34. Kuroda, M. A.; Leburton, J. P., High-Field Electrothermal Transport in Metallic Carbon Nanotubes. *Physical Review B* **2009,** *80* (16).

35. Kuroda, M. A.; Leburton, J. P., Self-Consistent Simulation of Electrical Nonlinearities and Thermal Transport in Metallic Carbon Nanotubes. *Journal of Computational and Theoretical Nanoscience* **2009,** *6* (8), 1937-1947.

36. Kumar, S.; Alam, M. A.; Murthy, J. Y., Computational Model for Transport in Nanotube-Based Composites with Applications to Flexible Electronics. *Journal of Heat Transfer* **2007,** *129* (4), 500-508.

37. Pop, E.; Mann, D. A.; Goodson, K. E.; Dai, H., Electrical and Thermal Transport in Metallic Single-Wall Carbon Nanotubes on Insulating Substrates. *Journal of Applied Physics* **2007,** *101* (9).

38. Lee, S. M.; Cahill, D. G., Heat Transport in Thin Dielectric Films. *Journal of Applied Physics* **1997,** *81* (6), 2590-2595.

39. Asheghi, M.; Kurabayashi, K.; Kasnavi, R.; Goodson, K. E., Thermal Conduction in Doped Single-Crystal Silicon Films. *Journal of Applied Physics* **2002,** *91* (8), 5079.

40. Zhou, Z.; Dou, X.; Ci, L.; Song, L.; Liu, D.; Gao, Y.; Wang, J.; Liu, L.; Zhou, W.; Xie, S.; Wan, D., Temperature Dependence of the Raman Spectra of Individual Carbon Nanotubes. *Journal of Physical Chemistry B* **2006,** *110* (3), 1206-1209.

Chapter 5: Ultra Fast Carbon Nanotube GC Detectors for Multi-Component Gas Mixtures

Highly sensitive and completely reversible detectors based on carbon nanotubes (CNTs) were fabricated for multi-component gas analysis. CNT detector was used in a series configuration with a gas chromatography column and exposed to a mixture of nine different compounds. It is shown that CNT based GC detectors are able to show responses to each individual component of the mixture when the detector operates in current stimulated desorption (CSD) mode. This is the first demonstration of a CNT based GC detector to analyze multi-component gas mixtures providing a new sensing approach for online air quality control and health monitoring applications. This chapter contains an expanded version of a possible future publication: A. Salehi-Khojin, Kevin Y. Lin, C.R. Field, R.I. Masel. "Carbon Nanotube Chemiresistor Based GC Detectors for Multi-Component Gas Chemical Mixtures."

5.1 Background on Carbon Nanotube Detectors

The development of miniaturized portable gas detectors that can detect toxic gas analytes in real time is a great issue in environmental pollution, medical diagnostics, military security, and other applications. In this respect, carbon nanotubes (CNT) have attracted great attention to be utilized as the active element of these detectors.[1-9] CNT being a quasi-one-dimensional material comprises of only surface atoms. Gas detectors based on CNT offer lower power consumption mainly due to their large carrier mobilities and smaller size.[10] CNT detectors also offer fast response and high sensitivity to the change in gas molecules interacting with the

surface. The central problems to CNT detectors are the lack of selectivity and irreversibility. These make it difficult to use CNT detectors for multi-component gas analysis.

5.2 Previous Works with Carbon Nanotubes Functionalization

Recent efforts in the community have been to functionalize carbon nanotubes with analyte specific entities. The two main approaches for surface functionalization of CNTs are covalent and non-convalent functionalization depending on how the functional groups get attached to the CNTs. Covalent functionalization is based on the approach to modify the end groups or the side walls on the CNTs.[11-13] For single-walled carbon nanotubes (SWNTs), this approach permanently changes the electronic properties of CNTs which is what makes them interesting in the first place.[11, 14] An alternative approach was to use multi-walled carbon nanotubes (MWNTs) and only modify the outer shell while leaving the inner core pristine.[15] However, the long recovery time is the main drawback of this approach since the target molecule is strongly attached to the functional groups on the CNTs. This makes it difficult for use in continuous and real-time detection.

On the other hand, non-covalent polymer functionalizations of CNTs can be done without affecting the electronic properties of CNTs. The sensing comes from degrees of swelling of the polymers through various adsorptive and wrapping forces such as van der waals and pi-stacking interactions.[16, 17] Problems with this approach include long term stability of the polymer as the polymer coatings phase separated, so that the sensors are not stable over a long time. Further, the amount of water in the ambient environment might interfere with the amount of swelling on the films.

One should notice that aforementioned methods all share the same mechanism which is based on the signal transduction. In essence, analytes in the vapor phase is adsorbed onto the transducer, and the differential adsorption of different analytes into arrays of detector in turn would generate a distinctive pattern. This must be analyzed via post-processing of collected data. The complexity of the required data analysis and data reduction algorithms along with aforementioned problems renders them unuseful for real-time applications.

5.3 Objective

Our approach is to use combination of a gas chromatography (GC) column to separate the mixture of gas molecules and use the specially tuned carbon nanotubes via newly discovered current stimulated desorption (CSD) mechanism[18] which provides reversible responses within seconds. Our experiment is to put a GC column and a CNT detector in a series configuration as shown schematically in Figure 5.1.A , inject a mixture of nine different chemical compounds into the GC column and measure the change in resistance of the CNT detector upon exposure to each individual compound. We overcome the selectivity issue using a GC column for separation. This allows detection of multiple components in a gas mixture with a single detector, given the CNT interacts with each component separately. The GC column allows different retention times for each molecule depending on its affinity to the column stationary phase. To the best of our knowledge, this is the first demonstration of using a CNT detector to analyze a multi-component gas mixture providing a new sensing approach for an online air quality control and health monitoring applications. In this study, we will provide a guideline for the design of CNT detectors for multi-component analysis.

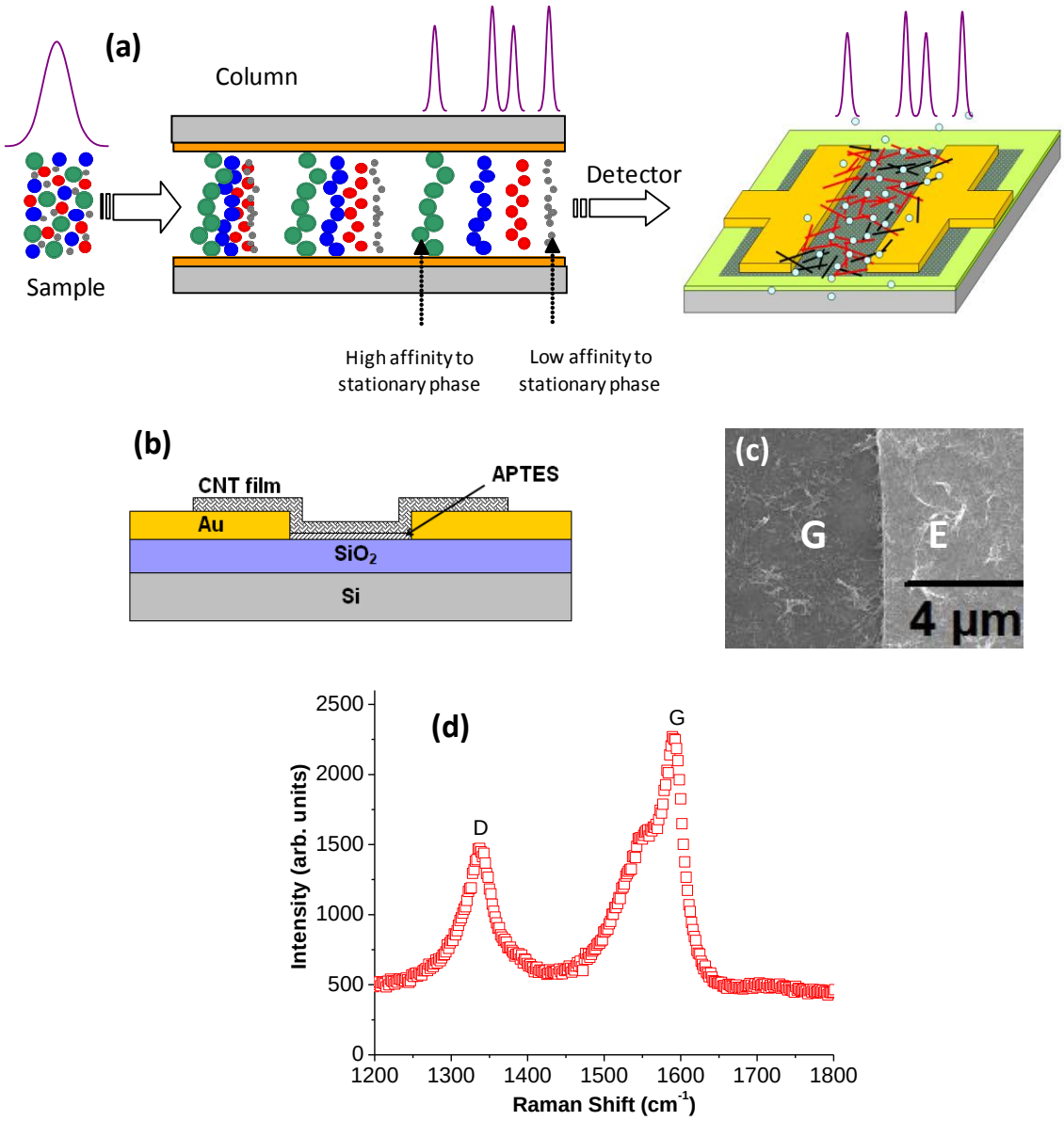

Figure 5.1: Shows (A) the schematic of experimental set up, (B) the cross section of the detectors, (C) SEM image of the nanotube detector (the gap zone and electrodes are labeled (G) and (E) in the SEM images, respectively), and (D) Raman spectrum of the nanotube network that include the intensity ratios of D/G of 0.67.

5.4 Results on Multi-Component Gas Detection via CNT GC Detector

Our CNT detectors consist of a carbon nanotube network between two gold contacts separated by 6 µm. Vacuum filtration method was used to produce uniform CNT films. The stamp printing method was then used to transfer carbon nanotubes to silicon substrate.[18-20] Figure 5.1.B and 5.1.C shows the cross section and scanning electron microscopy (SEM) image of the device, respectively. Figure 5.1.D also shows the Raman spectra of the carbon nanotube network.

Figure 5.2.A shows the response of our CNT detector to nine different chemical compounds separated by a GC column. The injected mixture was 10^{14} molecules of methanol, ethanol, 2-propanol, 1-propanol, 2-butanol, benzene, 1-butanol, 3-methyl-1-butanol, and toluene. We also did a similar experiment with a commercially available Flame Ionization Detector (FID) for verification and comparison. The chromatogram for the FID experiment is shown in Figure 5.2.B.

From the chromatograms in Figure 5.2, the CNT detector's performance is comparable to the FID. All nine peaks in the FID were also detected by the CNT detector. Interestingly, the FID did not fully resolve peaks 8 and 9, but the CNT detector was able to detect peaks 8 and 9 with greater resolution and no shoulder. Clearly, the CNT detector was capable of detecting all nine peaks and shows a comparable performance to the FID, which has not been previously demonstrated. The results open up the possibility of using inexpensive penny size CNT detectors as a promising alternative to FID system. Add to this, CNT detectors are non-destructive in contrast to FID detector. Moreover, nanotubes respond to most of the chemical compounds, while FID essentially can only detect components which can be burned.

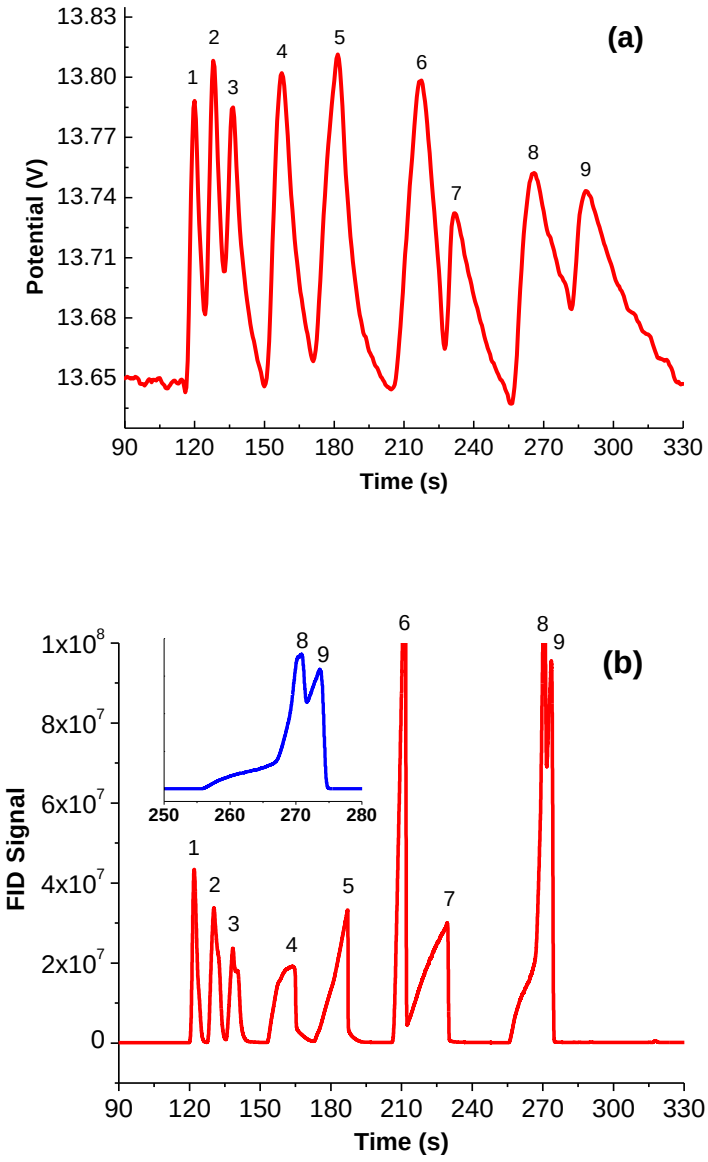

Figure 5.2: Shows (A) gas chromatograph of nine different compounds of a mixture using unfunctionalized nanotube detector at the CSD regime, and (B) a similar experiment with a FID. The components corresponding to peaks 1-9 shown on Figures 5.2.A and 5.2.B are Methanol, Ethanol, 2-Propanol, 1-Propanol, 2-Butanol, Benzene, 1-Butanol, 3-Methyl-1-Butanol, and Toluene respectively. Reproducible results from CNT detectors were observed.

5.5 Operation Theory

Key to this advance is the operation of the CNT detector in electron hopping (Poole-Frenkel) conduction regime.[20] Typically, three main mechanisms of electron transport in nanotubes have been established: quantum tunneling,[21-23] Schottky-Richardson conduction,[24-27] and Poole-Frenkel conduction.[28-32] At low electric fields, quantum tunneling dominates. Electrons travel by tunneling between quantum states in the nanotube. Currents are small, but resistances are too. Increasing the electric field leads to Schottky-Richardson (S-R) conduction,[24-27] in which transport occurs mainly within the conduction band of the nanotube. At higher voltages/currents, a third transport mechanism, called Poole-Frenkel (P-F) conduction, begins to dominate.[28-32] In this regime, high energy electrons jump over defects on the surface of the nanotubes and then continue along the nanotube. One can easily increase the energy of these electrons via increasing the applied voltage/current to the sensors. When these high energy electrons collide with molecules on nanotube surface, they transfer excess energy to them, and take them off the nanotube surface. Figure 5.3 demonstrates the schematic of this process which is called current stimulated desorption (CSD),[18] and Figures 5.2.A and 5.4 show the effectiveness of this approach for multi-component detection.

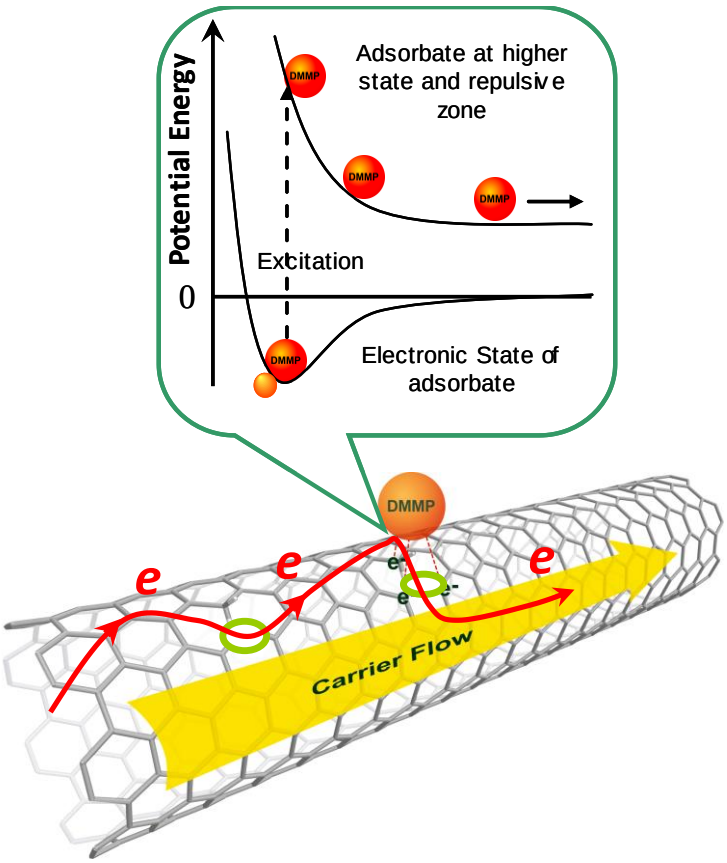

Figure 5.3: Shows a schematic representation of the current stimulated desorption (CSD) mechanism at the Poole-Frenkel conduction regime. The large yellow arrow highlights the electron carrier flow, and the red arrow illustrates Poole-Frenkel conduction, where high energy electrons jump between defect sites shown as green circles. When a high energy electron impacts the physio-adsorbed gas molecules on the surface of a nanotube, the electron excites the adsorbate into a repulsive state which ejects molecules from the nanotube surface.

We used two steps in order to promote CNT detectors to the electron hopping and CSD regime. First, we introduced intense defects on the CNT networks (see Figure 5.1.C) and applied high electric field (above 12V) to the detector. The high energy electrons of this conduction regime are then used to eject gas molecules from the nanotube surface. Defects were

reproducibly introduced in the fabrication process via high intensity ultrasound. Second, we fabricated detectors with negligible contact resistance.[18-20] Our fabricated detectors by vacuum filtration and stamp printing techniques exhibit negligible contact resistance. This is also an important step toward CSD since it eliminates the source of heating in the CNT detectors, thereby move the desorption process into electronic stimulation rather than thermal stimulation. Further, smaller contact resistance reduces the Schottky-Richardson barrier in the contact region and will accelerate the electric transport transition from Schottky-Richardson to Poole-Frenkel (electron hopping) regime.

5.6 Mott's Variable Range Hopping Mechanism

We performed an additional experiment to verify the electron hopping regime in our sensors. The experiment was to measure resistance of CNT sensors versus temperature in the range of 100-400 K, and use Mott's variable range hopping (VRH) model to explain the order of hopping in our highly defected network. Figure 5.4 shows the temperature-dependent resistance of the sensor fitted to the following Mott's VRH model:

$$R(T) = R_0 \exp\left[-\left(T_0/T\right)^n\right]$$

Where R_0 is a constant, T_0 is the characteristic temperature and n is the (dimensionality + 1) of hopping in Mott's variable range hopping (VRH) model. The plot of Ln R vesus $T^{-0.5}$ for our sensors show a linear fitting as shown in the inset of Figure 5.4. This confirms that the electron transport in our sensors is consistent with 1-D hopping mechanism. This is also consistent with our previously reported network analysis.[33] We have shown that in a network with highly

defected CNTs, the modulation of nanotube themselves has significant effect on the response of CNT networks, while modulation of junctions has little effect. In such a case, nanotube defects form low-energy sorption sites for chemical vapors, and consequently an inherent potential to significantly influence the electrical response of sensors for a broad spectrum of chemical vapors. However, the level of contribution from the defect sites on the conductance change is directly related to amount of detrapped charges from these sites to the electron carrier flow. This necessitates the operation of CNTs in the electron hopping regime (hopping through defect sites) for high sensitive detection of analyte molecules. One can easily increase the energy of these electrons to above 12 V to stimulate the gas molecules to desorb from nanotube surface. It should be noticed that in pristine nanotubes, only junctions contribute to the response of sensors.[33] In such a case, in principle, no electron hoping regime (Poole-Frenkel conduction) can be occured to promote CSD regime in the sensors.

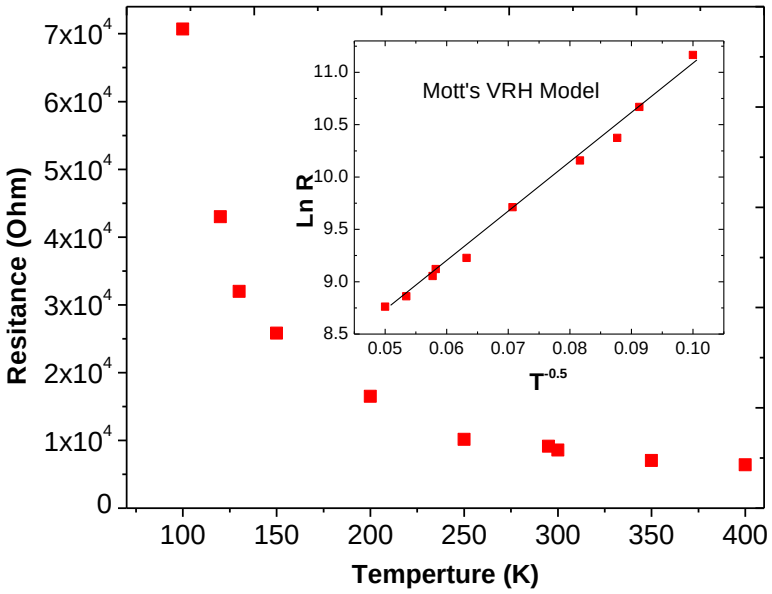

Figure 5.4: Shows temperature-dependent resistance of highly defected nanotube sensors. The inset shows the fitting of Ln *R* to $T^{-0.5}$ according to the Mott's VRH model.

5.7 NON-CSD Operation

It is also remarked that we were not able to repeat the results in Figure 5.2.A with a thermal desorption process.[18] We increased the sensor temperature up to 115°C where we observed the first reversible response of the sensor. However, at this temperature, the response of the nanotubes was a lot smaller than that in the CSD regime. Furthermore, the sensor start to degrade severely due to a continuously rising the baseline.

Figure 5.5 shows data taken from a similar experiment, but the CNT detector operates at a lower current, where the potential is too low to have the CSD mechanism. A close look at the results shows that the detector is not reliable for real applications, since it is not fast enough to separate different molecules i.e. benzene from 1-butanol (peaks 6 and 7) and 3-methyl-1-butanol from toluene molecules (peaks 8 and 9) as shown in Figure 5.2. Further, the detector shows a big drift indicating that the detector did not recovered well. We observed that the sensor fails after few runs.

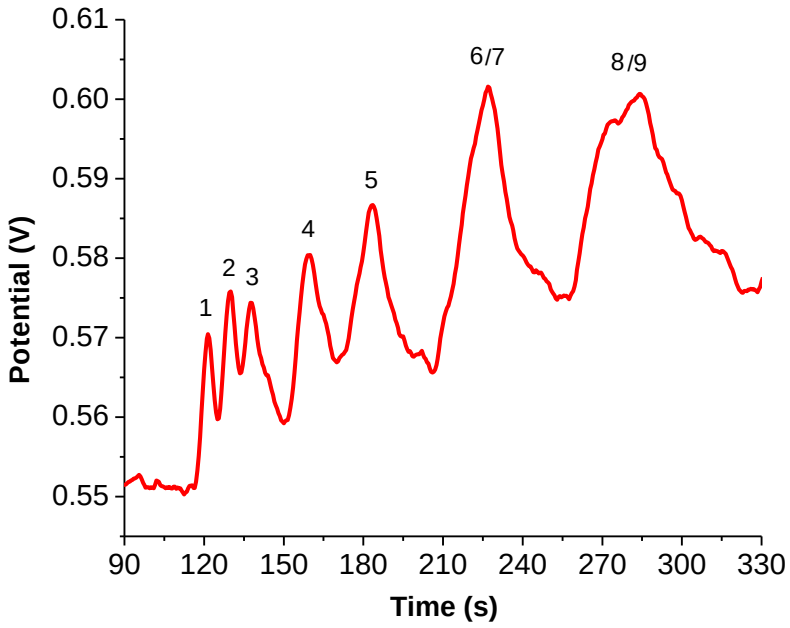

Figure 5.5: Shows the gas chromatograph of nine different compounds of a mixture using unfunctionalized nanotube detector operating at lower currents, i.e. not in the CSD regime. The components corresponding to peaks 1-9 shown on Figures 5.4 are Methanol, Ethanol, 2-Propanol, 1-Propanol, 2-Butanol, Benzene, 1-Butanol, 3-Methyl-1-Butanol, and Toluene respectively.

5.8 Conclusion

In summary, we used CNT detectors in a series configuration with a GC column and injected mixtures of nine different gas molecules into the column. When a pulse of a mixture of gases goes through the column, each gas is separated depending on its affinity towards the column stationary phase. The one factor that controls the success with this method is the fast and reversible nature of the CNT detector. It was shown that in order to detect each individual component of the mixture via CNT detector, one need to run the detector in the CSD mode.

Three conditions must meet for this effect to occur. First CNTs must have large density of defects rather than pristine structures. Second the detector must operate with a high voltage (>12V). Third the detector must fabricate with negligible contact resistance.

The approach proposed in this work is similar to a FID and a thermal conductivity detector (TCD), but the difference is that a nanotube detector is used to differentiate the compounds. This will be useful if one wishes to fabricate a cheap, small, and simple CNT-based detector for portable applications, and open up a new sensing approach for online air quality control and health monitoring applications.

5.9 References

1. Baughman, R. H.; Zakhidov, A. A.; De Heer, W. A., Carbon Nanotubes - the Route toward Applications. *Science* **2002,** *297* (5582), 787-792.
2. Kong, J.; Franklin, N. R.; Zhou, C.; Chapline, M. G.; Peng, S.; Cho, K.; Dai, H., Nanotube Molecular Wires as Chemical Sensors. *Science* **2000,** *287* (5453), 622-625.
3. Li, J.; Lu, Y.; Ye, Q.; Cinke, M.; Han, J.; Meyyappan, M., Carbon Nanotube Sensors for Gas and Organic Vapor Detection. *Nano Lett.* **2003,** *3* (7), 929-933.
4. Modi, A.; Koratkar, N.; Lass, E.; Wei, B.; Ajayan, P. M., Miniaturized Gas Ionization Sensors Using Carbon Nanotubes. *Nature* **2003,** *424* (6945), 171-174.
5. Peng, G.; Track, E.; Haick, H., Detecting Simulated Patterns of Lung Cancer Biomarkers by Random Network of Single-Walled Carbon Nanotubes Coated with Nonpolymeric Organic Materials. *Nano Lett.* **2008,** *8* (11), 3631-3635.

6. Qi, P.; Vermesh, O.; Grecu, M.; Javey, A.; Wang, Q.; Dai, H.; Peng, S.; Cho, K. J., Toward Large Arrays of Multiplex Functionalized Carbon Nanotube Sensors for Highly Sensitive and Selective Molecular Detection. *Nano Lett.* **2003,** *3* (3), 347-351.

7. Robinson, J. A.; Snow, E. S.; BÇŽdescu, Å. C.; Reinecke, T. L.; Perkins, F. K., Role of Defects in Single-Walled Carbon Nanotube Chemical Sensors. *Nano Lett.* **2006,** *6* (8), 1747-1751.

8. Snow, E. S.; Perkins, F. K.; Houser, E. J.; Badescu, S. C.; Reinecke, T. L., Chemical Detection with a Single-Walled Carbon Nanotube Capacitor. *Science* **2005,** *307* (5717), 1942-1945.

9. Someya, T.; Small, J.; Kim, P.; Nuckolls, C.; Yardley, J. T., Alcohol Vapor Sensors Based on Single-Walled Carbon Nanotube Field Effect Transistors. *Nano Lett.* **2003,** *3* (7), 877-881.

10. Lee, C. Y.; Sharma, R.; Radadia, A. D.; Masel, R. I.; Strano, M. S., On-Chip Micro Gas Chromatograph Enabled by a Noncovalently Functionalized Single-Walled Carbon Nanotube Sensor Array. *Angewandte Chemie - International Edition* **2008,** *47* (27), 5018-5021.

11. Chen, J.; Hamon, M. A.; Hu, H.; Chen, Y.; Rao, A. M.; Eklund, P. C.; Haddon, R. C., Solution Properties of Single-Walled Carbon Nanotubes. *Science* **1998,** *282* (5386), 95-98.

12. Hamon, M. A.; Hu, H.; Bhowmik, P.; Niyogi, S.; Zhao, B.; Itkis, M. E.; Haddon, R. C., End-Group and Defect Analysis of Soluble Single-Walled Carbon Nanotubes. *Chemical Physics Letters* **2001,** *347* (1-3), 8-12.

13. Riggs, J. E.; Guo, Z.; Carroll, D. L.; Sun, Y.-P., Strong Luminescence of Solubilized Carbon Nanotubes. *Journal of the American Chemical Society* **2000,** *122* (24), 5879-5880.

14. Yao, Z.; Braidy, N.; Botton, G. A.; Adronov, A., Polymerization from the Surface of Single-Walled Carbon Nanotubes Âˆ’ Preparation and Characterization of Nanocomposites. *Journal of the American Chemical Society* **2003,** *125* (51), 16015-16024.

15. Kalita, G.; Adhikari, S.; Aryal, H. R.; Ghimre, D. C.; Afre, R.; Soga, T.; Sharon, M.; Umeno, M., Fluorination of Multi-Walled Carbon Nanotubes (Mwnts) Via Surface Wave Microwave (Sw-Mw) Plasma Treatment. *Physica E: Low-dimensional Systems and Nanostructures* **2008,** *41* (2), 299-303.

16. Star, A.; Stoddart, J. F.; Steuerman, D.; Diehl, M.; Boukai, A.; Wong, E. W.; Yang, X.; Chung, S.-W.; Choi, H.; Heath, J. R., Preparation and Properties of Polymer-Wrapped Single-Walled Carbon Nanotubes. *Angewandte Chemie* **2001,** *113* (9), 1771-1775.

17. Xia, H.; Wang, Q.; Qiu, G., Polymer-Encapsulated Carbon Nanotubes Prepared through Ultrasonically Initiated in Situ Emulsion Polymerization. *Chemistry of Materials* **2003,** *15* (20), 3879-3886.

18. Salehi-Khojin, A.; Lin, K. Y.; Field, C. R.; Masel, R. I., Nonthermal Current-Stimulated Desorption of Gases from Carbon Nanotubes. *Science* **2010,** *329* (5997), 1327-1330.

19. Field, C. R.; Yeom, J.; Salehi-Khojin, A.; Masel, R. I., Robust Fabrication of Selective and Reversible Polymer Coated Carbon Nanotube-Based Gas Sensors. *Sens. Actuators, B* **2010,** *148* (1), 315-322.

20. Salehi-Khojin, A.; Field, C. R.; Yeom, J.; Masel, R. I., Sensitivity of Nanotube Chemical Sensors at the Onset of Poole-Frenkel Conduction. *Appl. Phys. Lett.* **2010,** *96* (16).

21. Kim, D.-H.; Huang, J.; Shin, H.-K.; Roy, S.; Choi, W., Transport Phenomena and Conduction Mechanism of Single-Walled Carbon Nanotubes (Swnts) at Y- and Crossed-Junctions. *Nano Lett.* **2006,** *6* (12), 2821-2825.

22. Lee, K. U.; Cho, Y. H.; Petty, M. C.; Ahn, B. T., Electrical Conductivity of Single-Wall Carbon Nanotube Film Deposited by Electrostatic Layer-by-Layer Assembly with the Aid of Polyelectrolytes. *Carbon* **2009,** *47* (2), 475-481.

23. Ounaies, Z.; Park, C.; Wise, K. E.; Siochi, E. J.; Harrison, J. S., Electrical Properties of Single Wall Carbon Nanotube Reinforced Polyimide Composites. *Composites Science and Technology* **2003,** *63* (11), 1637-1646.

24. Behnam, A.; Johnson, J. L.; Choi, Y.; Ertosun, M. G.; Okyay, A. K.; Kapur, P.; Saraswat, K. C.; Ural, A., Experimental Characterization of Single-Walled Carbon Nanotube Film-Si Schottky Contacts Using Metal-Semiconductor-Metal Structures. *Appl. Phys. Lett.* **2008,** *92* (24), 243116/1-243116/3.

25. Peng, N.; Zhang, Q.; Chow, C. L.; Tan, O. K.; Marzari, N., Sensing Mechanisms for Carbon Nanotube Based Nh3 Gas Detection. *Nano Lett.* **2009,** *9* (4), 1626-1630.

26. Suehiro, J.; Imakiire, H.; Hidaka, S.-i.; Ding, W.; Zhou, G.; Imasaka, K.; Hara, M., Schottky-Type Response of Carbon Nanotube No2 Gas Sensor Fabricated onto Aluminum Electrodes by Dielectrophoresis. *Sens. Actuators, B* **2006,** *B114* (2), 943-949.

27. Yamada, T., Equivalent Circuit Model for Carbon Nanotube Schottky Barrier: Influence of Neutral Polarized Gas Molecules. *Appl. Phys. Lett.* **2006,** *88* (8), 083106/1-083106/3.

28. Jombert, A. S.; Coleman, K. S.; Wood, D.; Petty, M. C.; Zeze, D. A., Poole-Frenkel Conduction in Single Wall Carbon Nanotube Composite Films Built up by Electrostatic Layer-by-Layer Deposition. *Journal of Applied Physics* **2008,** *104* (9), 094503/1-094503/7.

29. Mabrook, M. F.; Pearson, C.; Jombert, A. S.; Zeze, D. A.; Petty, M. C., The Morphology, Electrical Conductivity and Vapour Sensing Ability of Inkjet-Printed Thin Films of Single-Wall Carbon Nanotubes. *Carbon* **2009,** *47* (3), 752-757.

30. Perello, D.; Yu, W.-J.; Bae, D.-J.; Chae, S.-J.; Kim, M.-J.; Lee, Y.-H.; Yun, M.-H., Pool-Frenkel Emission and Hopping Conduction in Semiconducting Carbon Nanotube Transistor. *Proc. SPIE* **2009,** *7399* (Carbon Nanotubes, Graphene, and Associated Devices II), 739907/1-739907/6.

31. Perello, D. J.; Yu, W. J.; Bae, D. J.; Chae, S. J.; Kim, M. J.; Lee, Y. H.; Yun, M., Analysis of Hopping Conduction in Semiconducting and Metallic Carbon Nanotube Devices. *Journal of Applied Physics* **2009,** *105* (12), 124309/1-124309/5.

32. Venet, C.; Pearson, C.; Jombert, A. S.; Mabrook, M. F.; Zeze, D. A.; Petty, M. C., The Morphology and Electrical Conductivity of Single-Wall Carbon Nanotube Thin Films Prepared by the Langmuir-Blodgett Technique. *Colloids Surf., A* **2010,** *354* (1-3), 113-117.

33. Salehi-Khojin, A.; Khalili-Araghi, F.; Kuroda, M. A.; Lin, K. Y.; Leburton, J.-P.; Masel, R. I., On the Sensing Mechanism in Carbon Nanotube Chemiresistors. *ACS Nano* **2010,** *5* (1), 153-158.

Chapter 6: On the Sensing Mechanism in Carbon Nanotube Chemiresistors

There has been recent controversy whether the response seen in carbon nanotube (CNT) chemiresistors is associated with a change in the resistance of the individual nanotubes or changes in the resistance of the junctions. In this study, we carry out a network analysis to understand the relative contributions of the nanotubes and the junctions on the change in resistance of the nanotube network. We find that the dominant mode of detection in nanotube networks changes according to the conductance level (defect level) in the nanotubes. In networks with perfect nanotubes, changes in the junctions between adjacent nanotubes and junctions between the contacts and the CNT's can make a detectable change in the resistance of the nanotube networks, while adsorption on the nanotubes has a smaller effect. In contrast, in networks with highly defected nanotubes, the changes in the resistance of the individual nanotubes make a detectable change in the overall resistance of a chemiresistor network, while changes in the junctions have smaller effects. The combinational effect is also observed for the case in between. The results show that the sensing mechanism of a nanotube network can change according to the defect levels of the nanotubes, which may explain the apparently contradictory results in the literature. This chapter contains an expanded version of an already published paper: A. Salehi-Khojin, F. Khalili-Araghi, M.A. Kuroda, Kevin Y. Lin, J.P. Leburton, R.I. Masel. "On the Sensing Mechanism in Carbon Nanotube Chemiresistors." *ACS Nano* 2011, 5 (1), 153-158.

6.1 Introduction

Interpenetrating network of metallic-semiconducting carbon nanotubes (CNTs) have been increasingly used as one of the key electronic materials for new classes of chemiresistors.[1-9] They consist of arrays of nanotubes between two gold contacts, and produce highly-sensitive response compared to other solid state gas chemiresistors. At this point, there is some controversy whether the response arise from the modulation of nanotube themselves, modulation of the junctions between gold and nanotubes or modulation of the junctions between two adjacent nanotubes. For example, K. Bradley *et al.*[10] showed that NH_3 mainly interact with carbon nanotubes themselves. In contrast, N. Peng *et al.*[11] suggested that the modulation of nanotube-metal electrode junctions influence the response to NH_3. In another experiment, Liu *et al.*[12] observed that both nanotube channels and nanotube-gold junctions play a role in the detection process of NH_3.

6.2 Objective

The objective of our work was to do calculations to see if we can understand why different sets of careful experiments give different results. In particular we were interested in determining whether changes in the properties of the nanotubes could change the dominant sensing mechanism. Recall that Gomez-Navarro *et al.*[13] found that the resistance of a nanotube changes by 3 orders of magnitude as defects form on the nanotube surface. We were interested if such changes were sufficient to switch the dominant mode of sensing.

6.3 Approaches in Simulation of Sensing Mechanism for Carbon Nanotubes

Our results show that the dominant sensing mechanism is highly dependent on the resistance of the nanotube. In particular, we show that in networks consisting of highly conductive (perfect) nanotubes, the chemiresistor response is determined by the junctions between adjacent metal nanotubes and the junctions between the nanotubes and the gold. However, in network with low conductive (heavily defected) nanotubes, the chemiresistor response is determined by modulations in the resistance of the nanotubes themselves. The combinational effect is also observed for the case in between.

This conclusion arises from a detailed systematic network electric transport analysis considering both metallic and semiconducting CNTs, and corresponding homogeneous-heterogeneous junctions. We did such an analysis and asked the question "How do changes in the resistance of the metal nanotubes, the semiconducting nanotubes and the junctions between them influence the response of a nanotube network". Our numerical technique is to vary the resistance of metallic and semiconducting nanotubes, and corresponding homogeneous-heterogeneous junctions one at a time within the experimental range, and determine the overall change of network conductance. We also considered a similar resistance for junctions between gold electrode and nanotube and junctions between two adjacent metallic nanotubes.

In detail, each CNT was modeled as a stick of length L that is randomly positioned on a 2D surface. One end of the tube is positioned randomly on the surface and its other end is determined after picking an arbitrary orientation with a uniform probability distribution between -180 and 180 degrees. Coordinates of the CNT junctions (nodes) are determined and a connectivity matrix (that identifies pairs of nodes that are connected to each other with a finite

resistance) is defined to represent the CNT network. In the produced network, the resistance arises because of two contributions: the resistance of the individual CNT and the resistance of junctions. Based on Gomez-Navarro *et al.*'s[13] work we choose three different scenarios in our simulation for CNTs; (i) perfect tube, (ii) slightly defected nanotubes, and (iii) heavily defected nanotubes. The resistance of each tube was calculated using the expression in Ref.[14] with a prefactor of $f\,(1 \le f \le 1000)$[13] for defects part as follow:

$$R = f\,\frac{R_0}{2}\left[1+\frac{L}{\lambda_{eff}}\right] \qquad (1)$$

in terms of the quantum resistance $R_0 = h/(2e^2)$ (where e is the electron charge and h is the Planck's constant) and the effective carrier mean free path λ_{eff}. In the case of metallic CNTs, the effective mean free path used in the computation was of the order of 600nm after accounting for the contribution of both acoustic and optical phonons.[14] In the case of intrinsic semiconducting nanotubes, their low carrier loading prevents the electrical conduction in the absence of doping, and their effective resistance becomes more than four orders of magnitude larger than their metallic counterparts. The junction resistances were assigned to 15.38 R_0 for metal-metal junctions, $33.3R_0$ for semiconducting-semiconducting junctions and 100 times higher than that of metal-metal for metal-semiconducting junctions.[15] Applying Kirchhoff's laws to the resulting network of resistors, the overall conductance of the network was calculated. The simulations corresponding to a certain network loading were repeated between 300 and 1000 times (depending on the CNT loading), and average values for the conductance of the network over these repetitions are reported.

6.4 Simulation of Carbon Nanotube Conductance

Figure 6.1 displays the nanotube networks' conductance obtained from simulation for the nanotube loadings per unit area up to 6 μm^{-2}. This is equivalent to 4 mg/L nanotube in solution that will be discussed later. We define *P* as the probability of finding at least one conducting path in the network. The inset of this figure shows the percolation probability of the chemiresistors, *P*, as a function of the CNT loading. The network conductivity, σ, dependence on CNT loading obtained from simulation are in accordance with the standard percolation theory described by $\sigma \propto (N - N_c)^{\alpha}$,where N is the volume loading of nanotube solution, N_c is the critical volume loading of the CNT corresponding to the percolation threshold (N_c=1/π(4.236/L_{tube})^2, and α is a critical fitting exponent. The best fit of $\sigma \propto (N - N_c)^{\alpha}$ to the theoretical curve shown in Figure 6.1 results in α = 1.92 which is close to the theoretical prediction of α=1.94.[16] Here we point out that the simulations performed in this study provides detailed information about nanotube networks, such as distribution of the current among metallic and semiconducting nanotubes, which cannot be accessed from experiment and analytical percolation equations.

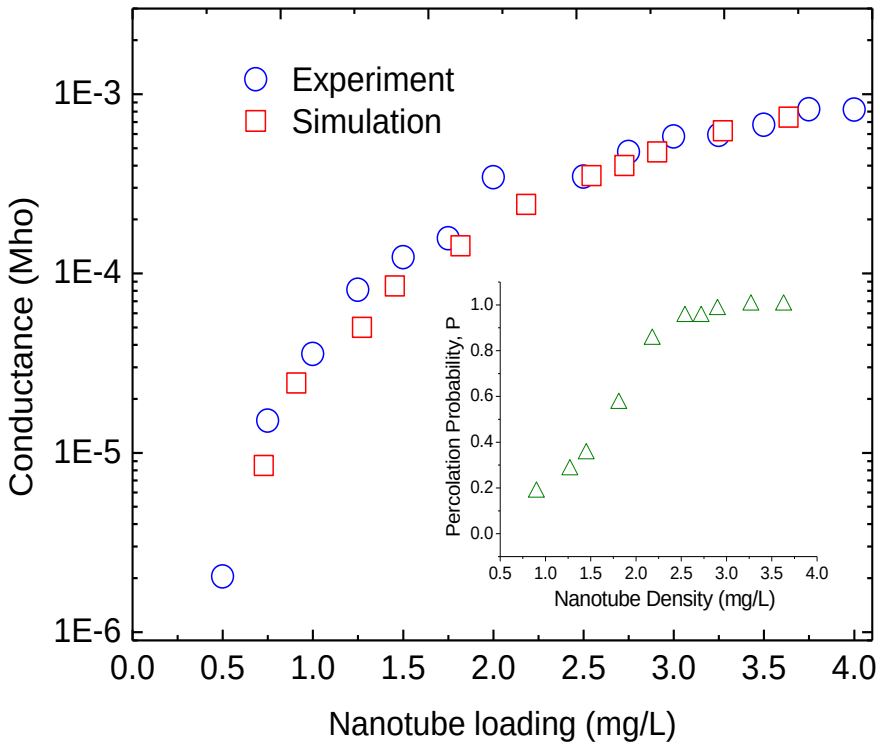

Figure 6.1: Experimental and simulated conductance vs. nanotube loading. The average conductance for the ensemble of networks fit very well to experimental results using a conversion factor of 0.66; the ratio of mass per unit volume of nanotube solution (mg/L) over nanotubes loading in unit area (μm^{-2}).

We also did experiments to verify the predictions of the computations. CNT networks were fabricated using liftoff photolithography as described in our previous papers[17] and the conductance shown in Figure 6.1 was measured. The average conductance measured for the network shows very good agreement with the simulations using a conversion factor of 0.66; the ratio of mass per unit volume of nanotube solution (mg/L) over nanotubes loading in unit area (μm^{-2}).

6.5 Simulation Results on Carbon Nanotubes Sensing Mechanism

Figure 6.2 shows the change in overall conductance of a network with equivalent loading of 1 mg/L by separately varying the resistance of the metallic nanotubes, the resistance of the semiconducting nanotubes, the resistance of the junctions between adjacent metal nanotubes, the resistance of junctions between adjacent semiconducting nanotubes, and the resistance of the junctions between adjacent metallic and semiconducting nanotubes. We did the analysis for three different conductance levels of nanotubes; (a) perfect nanotubes (f=1 in Eq. (1)), (b) heavily defected nanotubes (f=500), (c) slightly defected nanotubes (f=70). For perfect nanotubes (Figure 6.2.A), we found that if the resistance of the junctions between adjacent metallic nanotubes changes as one might expect if gas adsorbs, there is a large change in the conductance of the network. In contrast variations in the resistance of metallic nanotubes, semiconducting nanotubes and junctions between two adjacent semiconducting nanotubes and junction between the adjacent metallic-semiconducting nanotubes have little effect.

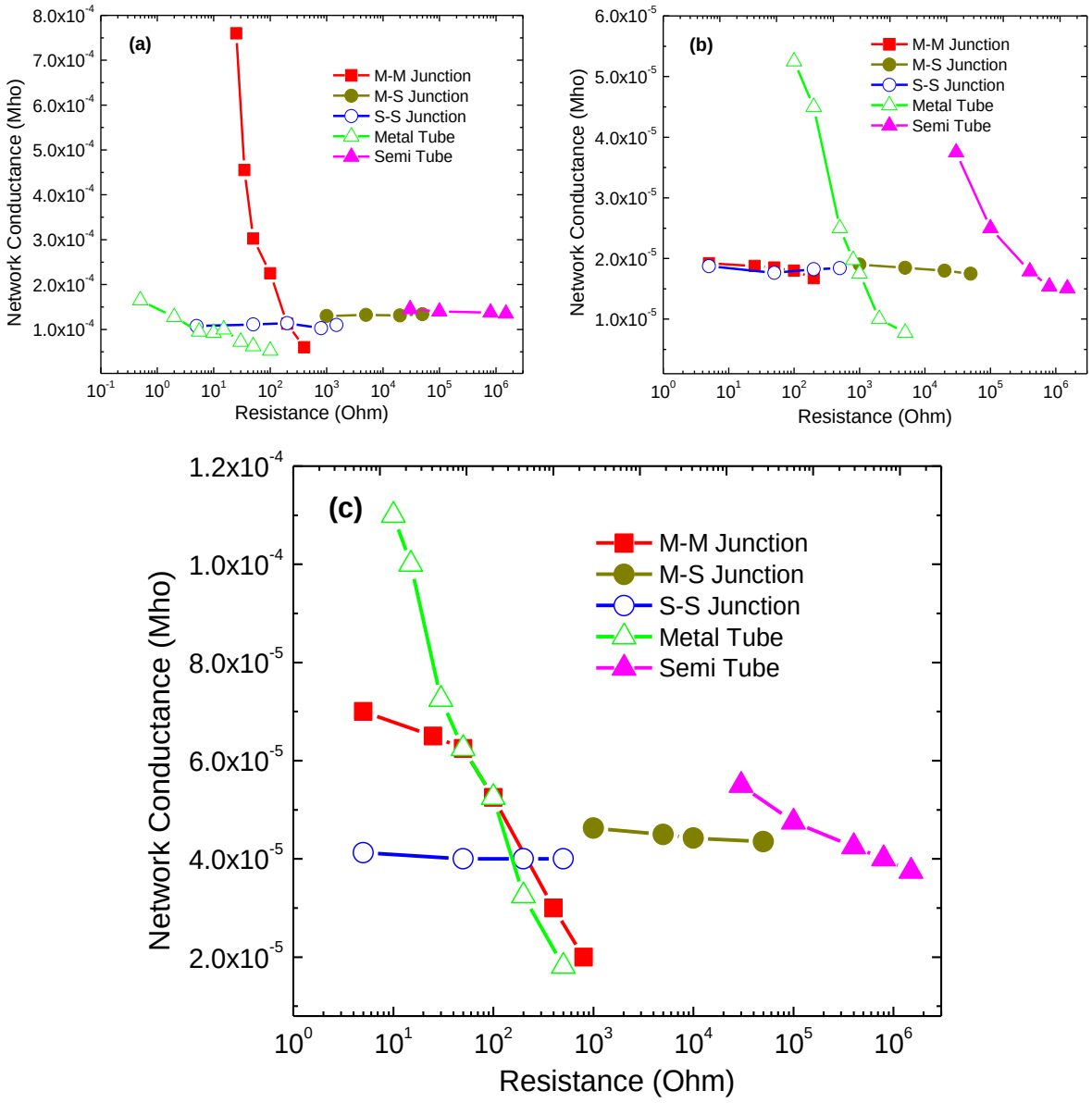

Figure 6.2: Variation of the nanotube network conductance as a function of the change in the resistance of metallic nanotubes, the change in the resistance of semiconducting nanotubes, and the change in the resistance of junctions between two adjacent nanotubes for the case of (A) perfect nanotube; *f*=1, (B) highly defected nanotubes; *f*=500, and (C) slightly defected nanotubes; *f*=70.

By comparison when the nanotubes are highly defective, changes in the resistance of the defected nanotubes have a significant effect on the overall conductance of the network. However, the variations in the resistance of all kinds of junctions have negligible effects. We also see the combinational effects for the case of slightly defected nanotubes as shown in Figure 6.2.C. These results clearly indicate that different conductance levels of nanotubes yield different sensing mechanisms in a network.

Physically, pristine nanotubes have a very low resistance. In such a case, the resistance of the nanotubes is low compared to the resistance of the junctions between adjacent nanotubes, so large percentage changes in the conductance of the nanotubes (*i.e.* changes larger than one would expect for gas adsorption) does not produce a significant change in the conduction of the network. The semiconducting nanotubes also have little effect because they have such high resistance that there is little or no current through them. Thus, only changes in the resistance of the junctions, either between adjacent nanotubes or between the nanotubes and the gold have a significant effect of the resistance on the network.

Defective nanotubes show the opposite effect. Defects can vary the resistivity of the nanotubes by 3 orders of magnitude.[13] In that case the resistance of the nanotubes is large compared to the resistance of the junctions. Hence, the changes in the resistance of the nanotubes have an important effect on the overall conduction of a network.

The analysis above only considered Shottkey-Richardson conduction in the nanotubes (*i.e.* conduction through the conduction band), but at higher voltages electron transport also occurs *via* Poole-Frenkel conduction if there are defects in the nanotube. If electrons are transported *via* Poole-Frenkel mechanism,[17-19] the electron hopping through nanotube defects can inject accumulated charges at the defect sites to the conduction band of nanotubes, which in turn

changes the conductance of the chemiresistor upon gas adsorption. That causes an enhancement in the sensitivity of the nanotubes because the analyte concentration is higher on defects than on pristine regions of the nanotubes. Details of such mechanism has been explained in Ref. [17]

6.6 Efficient Current for Pure Electron Hopping

To determine the efficient current required for achieving pure electron hopping, we considered the experimental condition where we applied a constant external current and obtained the histogram of currents passing through nanotube segments. Figure 6.3 shows the histogram results presented in the form of fraction of nanotubes that carry a specific current at each nanotube loading, while Figure 6.4 shows the sensitivity of the chemiresistors to adsorption of gas. The detail of experimental section has been explained in Refs.[17] In this calculation, we assumed that our network was made of highly defected nanotubes.

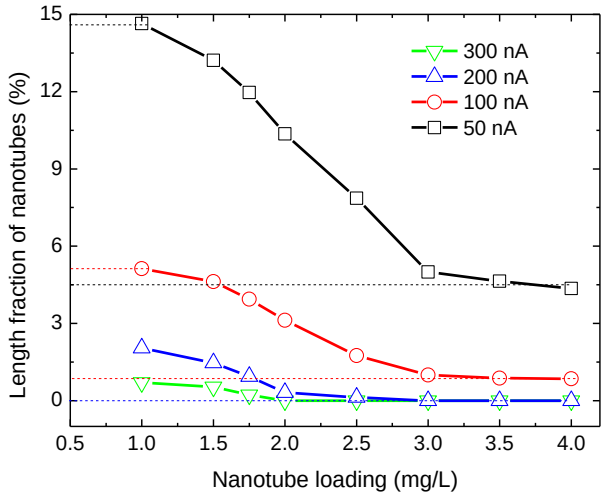

Figure 6.3: Length fraction of nanotubes that carries specific current vs. nanotube loading. 100 nA is the maximum current that the length fraction of all networks is able to carry it. Lower currents are not efficient and higher currents only exist in lower nanotube loadings.

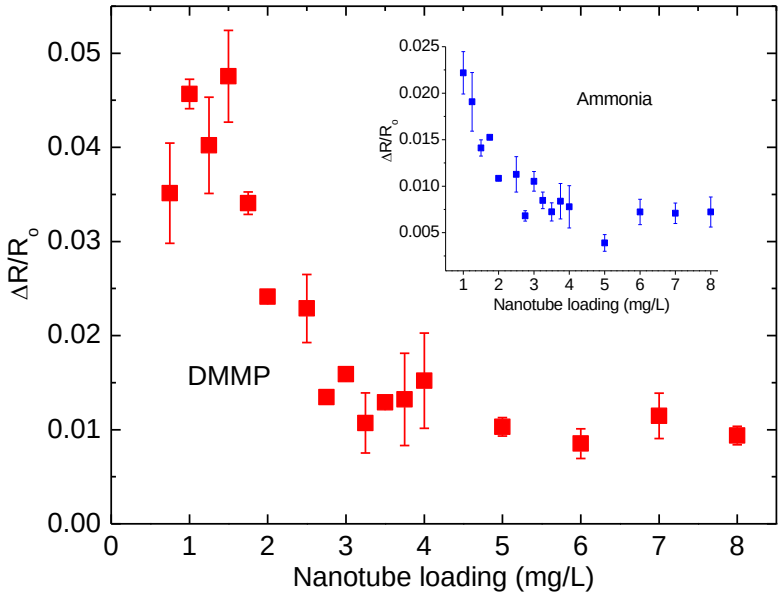

Figure 6.4: Shows typical the normalized response to 10 ppm DMMP gas molecules for nanotube chemiresistors with loadings 0.75 to 8 mg/L. The inset shows the response to ammonia molecules.

It is useful to compare Figures 6.3 and 6.4. We observe a similar trend for both sensitivity and fraction of nanotubes vs. nanotube loading for current equal or less than 100 nA. We also observe that there are no nanotube segments at higher loadings that carry currents higher than 100 nA. Results suggest that 100 nA is an upper limit for the minimum current required for the efficient electron hopping process.

6.7 Carbon Nanotubes 1/f noise level

Figure 6.3 also indicates that the fraction of nanotubes that carry a 100 nA current decreases with the increase in the network loading. This result suggests a similar trend in the electron hopping distance (or range) vs. nanotube loading. If this is the case, thus, one should

also expect a similar trend in the charge fluctuation and consequently in the 1/f noise level. To check this hypothesis, we measured the 1/f noise level of our chemiresistors at three different applied currents for different nanotube loadings. Results are displayed on Figure 6.5. We attribute the increased 1/f noise level at lower nanotube loadings to higher charge fluctuations in these networks due to higher extent of electron hopping process. A diminished trend of 1/f noise with network loading is also consistent with the reduction in the electron hopping distance (or range) as shown in Figure 6.4. The results indicate that the electron hopping mechanism in Poole-Frenkel conduction well describes the sensitivity and noise level in highly defected nanotube chemiresistors.

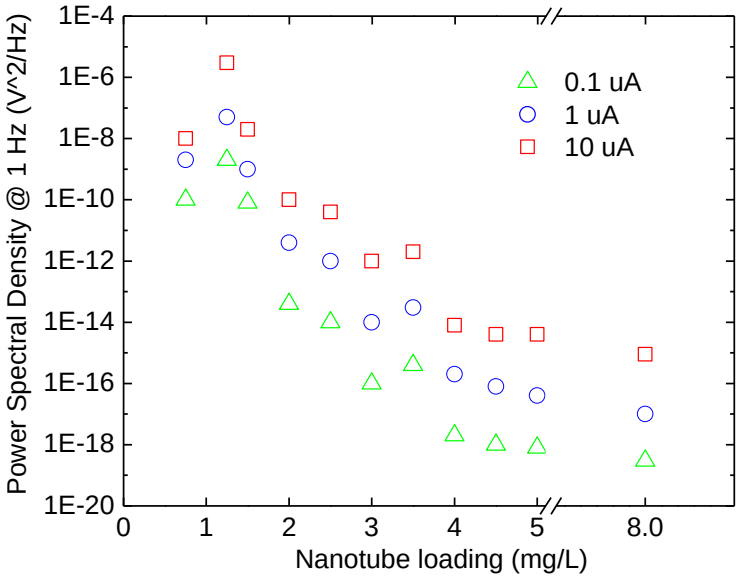

Figure 6.5: Measured noise density for nanotube chemiresistors with nanotube loadings ranging from 0.75 to 8 mg/L at three applied electric currents. The maximum noise level is at 1 mg/L. The noise level reduces with the network loading and then stayed fairly constant. A similar trend was observed in Figures 6.3 and 6.4.

6.8 Conclusion

To summarize, we performed network simulation to differentiate the sensing mechanism in nanotube chemiresistors. We found that the change in the resistance of nanotubes can modify the dominant detection mechanism in nanotube chemiresistors. Our results showed that networks with highly defective nanotubes were only influenced by change in the resistance of the nanotube themselves, while networks with pristine nanotubes were only modulated by modulation of the resistance of junctions. Clearly, in the latter case, among junctions between gold electrode and nanotubes, and junctions between adjacent metallic nanotubes, the one with higher resistance makes bigger contribution to the overall conductance of nanotube networks. Our results explain how seemingly identical studies done carefully on different nanotubes and with different fabrication techniques can reach different conclusions on the dominant sensing mechanism in nanotube networks, as reported by Bradley *et al.*[10], Peng *et al.*[11] and Liu *et al.*[12]

6.9 References

1. Kong, J.; Franklin, N. R.; Zhou, C.; Chapline, M. G.; Peng, S.; Cho, K.; Dai, H., Nanotube Molecular Wires as Chemical Sensors. *Science* **2000,** *287* (5453), 622-625.
2. Lee, Chang Y.; Sharma, R.; Radadia, Adarsh D.; Masel, Richard I.; Strano, Michael S., On-Chip Micro Gas Chromatograph Enabled by a Noncovalently Functionalized Single-Walled Carbon Nanotube Sensor Array13. *Angewandte Chemie* **2008,** *120* (27), 5096-5099.
3. Novak, J. P.; Snow, E. S.; Houser, E. J.; Park, D.; Stepnowski, J. L.; McGill, R. A. Nerve Agent Detection Using Networks of Single-Walled Carbon Nanotubes. 2003.

4. Peng, G.; Tisch, U.; Haick, H., Detection of Nonpolar Molecules by Means of Carrier Scattering in Random Networks of Carbon Nanotubes: Toward Diagnosis of Diseases Via Breath Samples. *Nano Letters* **2009,** *9* (4), 1362-1368.

5. Robinson, J. A.; Snow, E. S.; BÇŽdescu, Å. C.; Reinecke, T. L.; Perkins, F. K., Role of Defects in Single-Walled Carbon Nanotube Chemical Sensors. *Nano Letters* **2006,** *6* (8), 1747-1751.

6. Robinson, J. A.; Snow, E. S.; Perkins, F. K., Improved Chemical Detection Using Single-Walled Carbon Nanotube Network Capacitors. *Sensors and Actuators, A: Physical* **2007,** *A135* (2), 309-314.

7. Snow, E. S.; Perkins, F. K.; Houser, E. J.; Badescu, S. C.; Reinecke, T. L., Chemical Detection with a Single-Walled Carbon Nanotube Capacitor. *Science* **2005,** *307* (5717), 1942-1945.

8. Vichchulada, P.; Zhang, Q.; Lay, M. D., Recent Progress in Chemical Detection with Single-Walled Carbon Nanotube Networks. *Analyst (Cambridge, United Kingdom)* **2007,** *132* (8), 719-723.

9. Zribi, A.; Knobloch, A.; Rao, R., Co2 Detection Using Carbon Nanotube Networks and Micromachined Resonant Transducers. *Applied Physics Letters* **2005,** *86* (20), 203112/1-203112/3.

10. Bradley, K.; Gabriel, J. C. P.; Star, A.; GruÌˆner, G., Short-Channel Effects in Contact-Passivated Nanotube Chemical Sensors. *Applied Physics Letters* **2003,** *83* (18), 3821-3823.

11. Peng, N.; Zhang, Q.; Chow, C. L.; Tan, O. K.; Marzari, N., Sensing Mechanisms for Carbon Nanotube Based Nh3 Gas Detection. *Nano Letters* **2009,** *9* (4), 1626-1630.

12. Liu, X.; Luo, Z.; Han, S.; Tang, T.; Zhang, D.; Zhou, C., Band Engineering of Carbon Nanotube Field-Effect Transistors Via Selected Area Chemical Gating. *Applied Physics Letters* **2005,** *86* (24), 1-3.

13. Gomez-Navarro, C.; Pablo, P. J. D.; Gomez-Herrero, J.; Biel, B.; Garcia-Vidal, F. J.; Rubio, A.; Flores, F., Tuning the Conductance of Single-Walled Carbon Nanotubes by Ion Irradiation in the Anderson Localization Regime. *Nat Mater* **2005,** *4* (7), 534-539.

14. Kuroda, M. A.; Leburton, J. P., High-Field Electrothermal Transport in Metallic Carbon Nanotubes. *Physical Review B* **2009,** *80* (16).

15. Fuhrer, M. S.; Nyg; aring; rd, J.; Shih, L.; Forero, M.; Yoon, Y.-G.; Mazzoni, M. S.; nbsp; C; Choi, H. J.; Ihm, J.; Louie, S. G.; Zettl, A.; McEuen, P. L., Crossed Nanotube Junctions. *Science* **2000,** *288* (5465), 494-497.

16. Stauffer, G., Introduction to Percolation Theory. *Taylor & Francis:London* **1985**.

17. Salehi-Khojin, A.; Field, C. R.; Yeom, J.; Shannon, M. A.; Masel, R. I., Sensitivity of Nanotube Chemical Sensors at the Onset of Poole-Frenkel Conduction *Applied Physics Letters* **2010,** *96*, 163110-163113.

18. Jombert, A. S.; Coleman, K. S.; Wood, D.; Petty, M. C.; Zeze, D. A., Poole-Frenkel Conduction in Single Wall Carbon Nanotube Composite Films Built up by Electrostatic Layer-by-Layer Deposition. *Journal of Applied Physics* **2008,** *104* (9), 094503/1-094503/7.

19. Suehiro, J.; Imakiire, H.; Hidaka, S.-i.; Ding, W.; Zhou, G.; Imasaka, K.; Hara, M., Schottky-Type Response of Carbon Nanotube No2 Gas Sensor Fabricated onto Aluminum Electrodes by Dielectrophoresis. *Sensors and Actuators, B: Chemical* **2006,** *B114* (2), 943-949.

Chapter 7: Perfectly Imperfect: Polycrystalline Graphene Ribbons as Chemiresistors

We explore the role of two-dimensional conduction and one-dimensional defects on the response of graphene chemiresistors, and uncover unexpected effects. Adsorption of isolated analyte molecules or adsorption on point defects has minimal effect on graphene resistance because current pathways form around the adsorbate. In contrast, analytes adsorbing on line defects lead to significant changes in resistance. We find that polycrystalline graphene easily obtained through chemical vapor deposition (CVD) contains line defects, offering a scalable path to 50x more sensitive chemiresistors than exfoliated crystalline graphene. Moreover, when we confine current flow by cutting the polycrystalline graphene into ribbons, the sensitivity increases by another factor of four. Parts per billion (pbb) sensitivity is obtained, exceeding that of carbon nanotube chemiresistors. These results show that graphene chemiresistors must be perfectly imperfect: *i.e.* polycrystalline graphene has extraordinary sensitivity, achieved through geometry and linear defect density. This chapter contains an expanded version of a future publication: A. Salehi-Khojin, D. Estrada, Kevin Y. Lin, M. Bae, F. Xiong, E. Pop, R.I. Masel. "Polycrystalline Graphene Ribbons as Chemiresistors."

7.1 Background on Graphene Properties

Graphene is a two-dimensional semimetal with zero band gap that exhibits excellent electrical properties.[1-8] Through the delocalized pi bonds, graphene's charge carriers can have high mobility ballistic conduction effects.[9, 10] Its unique band structure results in high carrier mobilities for both electrons and holes, reportedly as high as 2×10^5 $cm^2/V\cdot s$ for freely suspended

graphene and on the order of 10^4 for graphene on SiO_2.[11] The charge carriers also behave as chiral Dirac fermions and display the quantum Hall effects and Klein tunneling.[9, 12-14] Other benefits for its two dimensional nature include the ability to screen charge fluctuations, more so than the comparative 1- dimensional carbon nanotubes.[15]

Recent studies have suggested that graphene might be an interesting chemiresistor material.[16-28] Electric transport through graphene can be sensitive to the adsorption of analyte molecules. Further, graphene exhibits lower 1/f noise level compared to other solid state sensors.[25, 29-32] While, these features show excellent potential for graphene as a chemical sensor, prior to this study, the sensitivity of graphene chemiresistors for many analytes has been below that of carbon nanotube chemiresistors (CNT).[17-28] However, Schedin has shown graphene being capable of detecting individual gas molecules as they adsorbed onto the material either by donating or accepting an electron and thus changing the sensor's conductivity.[15]

7.2 Objective

The objective of this work was to understand why graphene had not proven to be a sensitive chemiresistor material, and to determine what could be done to improve the sensitivity. We focused on the idea that while graphene shares several similarities with CNTs, graphene is a two-dimensional conductor while CNTs are essentially one-dimensional conductors. Could this difference in dimensionality be responsible for the difference in behavior?

Further, at this point, the physical mechanisms of interaction between adsorbed species and graphene are not as fully understood as in CNT sensors. We have recently shown that point defects in carbon nanotubes are what contribute to the highly sensitive response towards target

analytes.[33] While much of the research within the graphene electronics community is geared towards producing large-scale and defect free graphene, only recently have linear defects in graphene emerged as a focused area of research.[34-38] The question we then ask is, "Are linear defects necessary to enhance the chemical sensitivity in two-dimensional systems such as graphene?"

7.3 Experimental Procedures

Fabrication of Mechanically Exfoliated Graphene. Graphene was deposited by a mechanical exfoliation method from natural graphite with adhesive tape onto a thermally oxidized Si substrate with 100 nm thick SiO_2. The substrate was annealed at 400 ^oC for 35 minutes in Ar/H_2 mixture in a furnace to remove glue residue. The number of the graphene layers was confirmed by optical contrast and Raman spectroscopy. To define source and drain metal electrodes on the graphene sheet, we deposit 40 nm thick Pd with an adhesive layer of 0.5 nm thick Cr on the graphene by using electron beam lithography, electron beam evaporation and lift-off processes. One more e-beam lithography step was used to form a 1 μm wide graphene channel, followed by an oxygen plasma etch, to yield the device shown in Figure 7.4.A.

Fabrication of CVD Graphene Sensors. Cr (10 nm)/Au (100 nm) electrodes are first patterned onto Si/SiO_2 substrates using standard lithographic techniques. Graphene films were grown using an Etamota chemical vapor deposition (CVD) system, on 1.4 mil copper foils purchased from Basic Copper. The foils are annealed under Ar/H_2 flow for 45 minutes and graphene is grown under a $CH_4/H_2/Ar$ flow (17:1:3 ratio) at 1000 ℃ for 30 min. The resulting Cu/graphene substrates are cooled to room temperature under the same gas flow at a rate of ≈ 20

℃/min. Graphene is subsequently transferred to the sensor electrodes by coating the graphene with PMMA, removing the backside graphene in an O_2 plasma, and then etching the backside copper in a 1M $FeCl_3$ solution (Figure 7.1 and 7.2). Extended graphene film and micro-ribbons are then defined with standard photolithography and graphene is patterned by O_2 plasma etching (Figure 7.3). Raman spectra were collected using a Renishaw confocal microscope with 633 nm excitation laser and spot size ~1 µm.

We then measured the resistance of all of the sensors, and selected the ones with low resistance. The measured resistance was between 60 and 70 ohms for all but one of the samples. The resistance of the graphene itself was measured with a four point probe and it was in the same range.

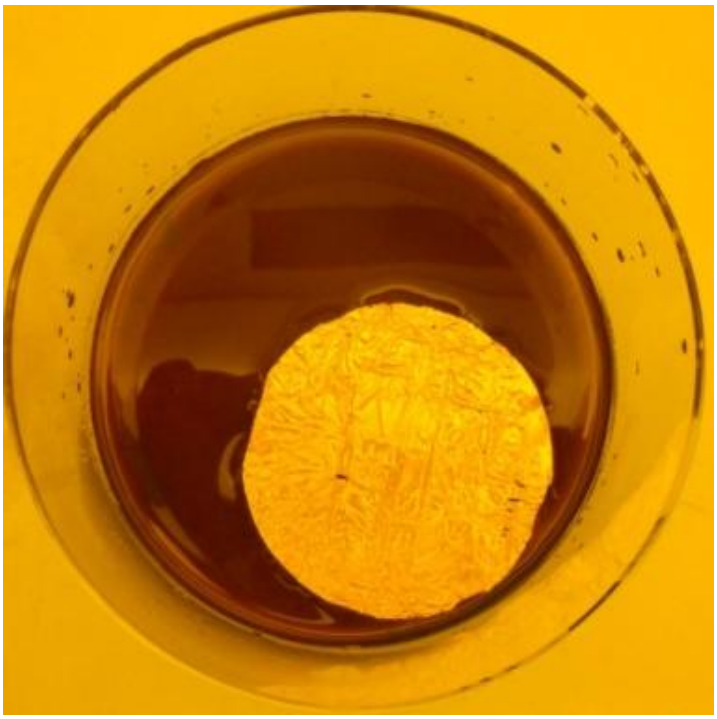

Figure 7.1: Photograph showing CVD grown graphene on copper foil and in copper etching solution $FeCl_3$.

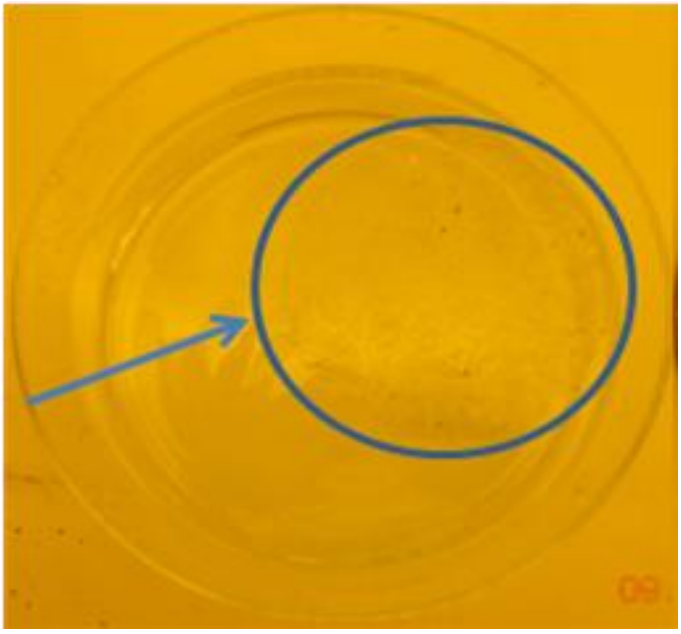

Figure 7.2: Photograph showing CVD grown graphene with PMMA as back support in DI water after copper etching.

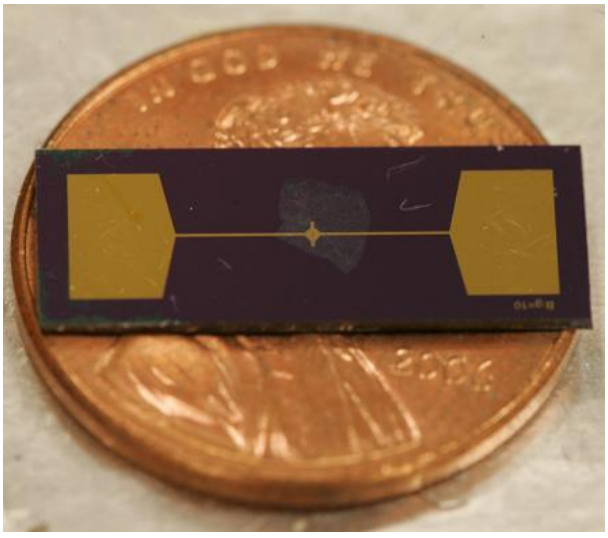

Figure 7.3: Photograph showing CVD grown graphene deposited on silicon substrate.

Fabrication of Single Walled Carbon Nanotube (SWNT) Sensors. A commercially available SWNT solution was obtained from NanoIntegris. The SWNT solution was then diluted

to desired concentration in 25 mL solution of 1% (w/v) sodium dodecyl sulfate (SDS) in water before being vacuum filtrated with mixed cellulose ester (MCE) membranes (Millipore, 0.22 micron pore size). After the SWNTs were successfully deposited onto the membranes, the wet MCE-SWNT membrane was dried for at least 2 hours under 15 in-Hg gauge pressure before multiple rinsing with approximately 80 mL of purified and deionized water (Millipore, MilliQ water). Multiple rinsing was intended to completely remove the SDS residue from the MCE-SWNT membrane. Finally, a stamp technique was used to transfer homogeneous, randomly aligned CNT films to predefined Cr/Au sensor electrodes (10, 100 nm).

Sensor Testing and Measurement. Sensors were placed in a custom built PEEK (polyaryletheretherketone) flow cell and a fused silica passivated capillary was used to connect to a Gas Chromatograph (GC) inlet. An Agilent 6893N GC/FID-MS with 7683B auto-sampler with a pulse of 100 ms was used to deliver target gas molecules to the sensors at pressure of 3.6 psi for all experiments. Ultra pure helium gas was used as a carrier gas at fixed flow rate. A VoltaLab 10 potentiostat (PGZ100) was used to monitor the change in potential on the sensors upon exposure to trace gas vapors.

7.4 Characterization of Graphene Samples Used

Next, we produced graphene films with both pristine and defective structures. Pristine graphene was obtained by mechanical exfoliation and defective graphene was produced by chemical vapor deposition (CVD) on copper substrates. The sensors were exposed to 100 milliseconds of toluene (an electron donor) and of 1,2-dichlorobenzene (an electron acceptor), and the change in the conductance is measured upon exposure to trace gas vapors. Our

experiments were designed to compare the response of a series of graphene chemiresistors made *via* different procedures so that we could vary the types of defects and determine their role.

The experiments used what we called "pristine" and "defective" samples. Figure 7.4.A shows an atomic force microscope (AFM) image of the pristine sample. This chemiresistor was fabricated using mechanical exfoliation and electron-beam patterning.[39] No evident line defects are found either on the AFM image, or by Raman analysis (Figure 7.4.G). However, scanning tunneling microscopy (STM) data of similar samples indicate the presence of a few point defects.[35]

By contrast, Figures 7.4.B and 7.4.C show AFM images of defective polycrystalline graphene grown by chemical vapor deposition (CVD), a method which creates line defects[40-42] similar to those previously reported by An *et al.*[43] and Lahiri *et al*.[34] The linear defects form two different patterns on the graphene surfaces. A few regions of the sample had 10 μm long well-aligned line defects, like those shown in Figure 7.4.B. However, the majority of the sample had randomly oriented line defects with an average length of about 0.7 μm. Raman spectra of both samples are shown in Figure 7.4.G. The pristine graphene sample does not show a D band, suggesting that the overall concentration of defects is low and the sample is monocrystalline.[44] By contrast, the CVD graphene sample shows a large D band, from which we can estimate the grain size in our polycrystalline graphene.[45] We find our sample varies between mono and bilayer graphene (Figure 7.4.D), with an average grain size of ~80 nm (Figure 7.4.E). In all cases, the regions between the line defects looked almost pristine. We have not detected many isolated point defects on our defective graphene samples.[35] Figure 7.5 shows the SEM picture of the extended CVD graphene. Figure 7.6 shows the SEM picture of the CVD graphene ribbons and Figure 7.7 shows the zoom-in SEM picture from one of the graphene ribbon. Figure 7.8

shows the Raman spectrum of the graphene ribbon sample and Figure 7.9 shows the D and G band intensities from Raman spectroscopy across the sample. Figure 7.10 shows the AFM picture of the extended graphene sample and Figure 7.11 shows the AFM topography of the sample across three different line scans identified on Figure 7.10. Figure 7.12 shows the close-up view of the AFM of extended graphene sample.

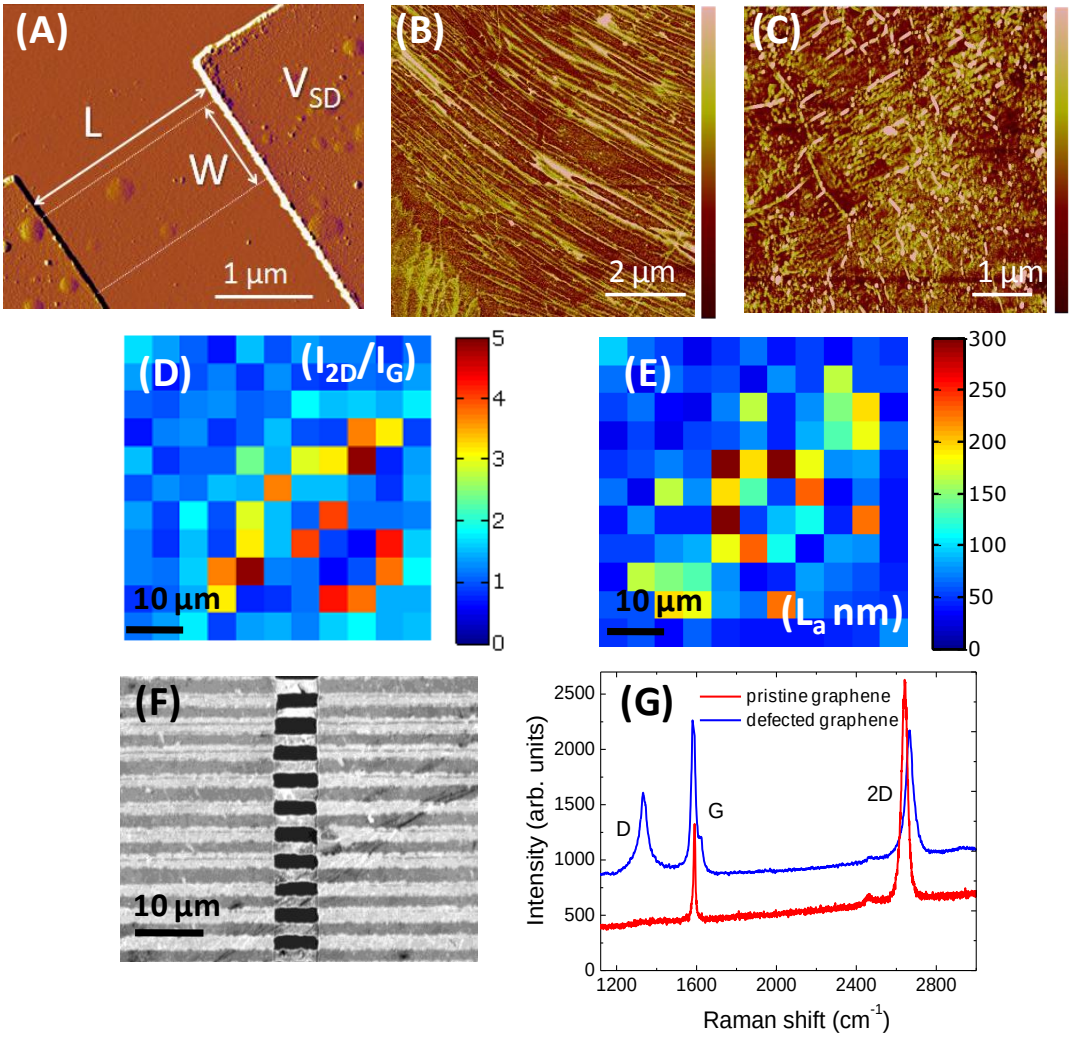

Figure 7.4: (A) AFM image of typical mechanically exfoliated ("pristine") graphene sensor, (B and C) AFM images of CVD graphene used for sensors, color scales are 10 and 5 nm, respectively, (D) map of I_{2D}/I_G ratio indicative of mono and bilayer graphene, (E) map of crystallite size indicative of 30 to >300 nm distance between line defects with an average of 80 nm, (F) SEM image of CVD graphene ribbons, and (G) Raman spectra of pristine and CVD-based defective grphene samples. The sheet resistance of extended pristine is 6×10^{-6} Ω.cm and defective graphene is 3×10^{-4} Ω.cm.

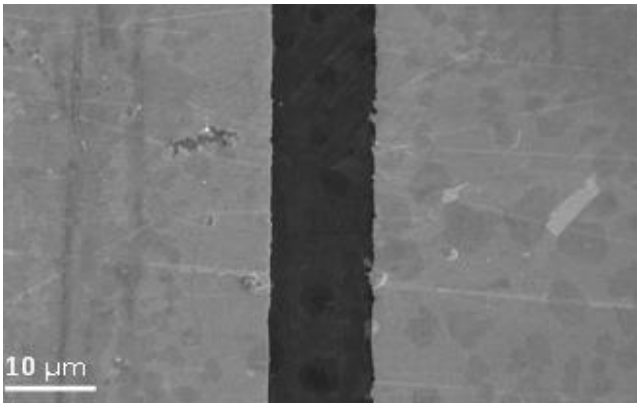

Figure 7.5: Shows zoom-in SEM image of extended graphene sensor (middle channel) and two electrodes (sides).

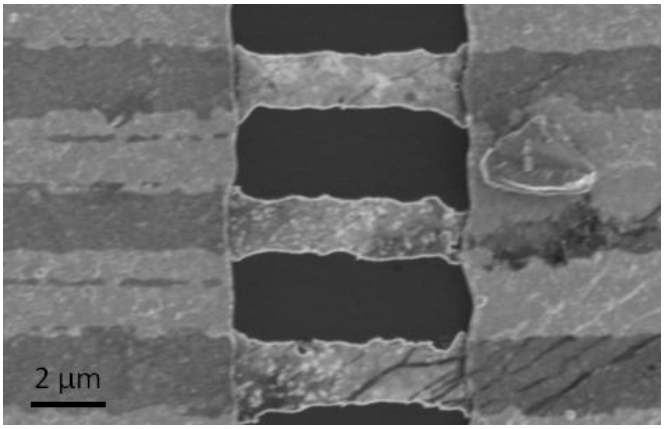

Figure 7.6: Shows SEM images of graphene ribbon sensors.

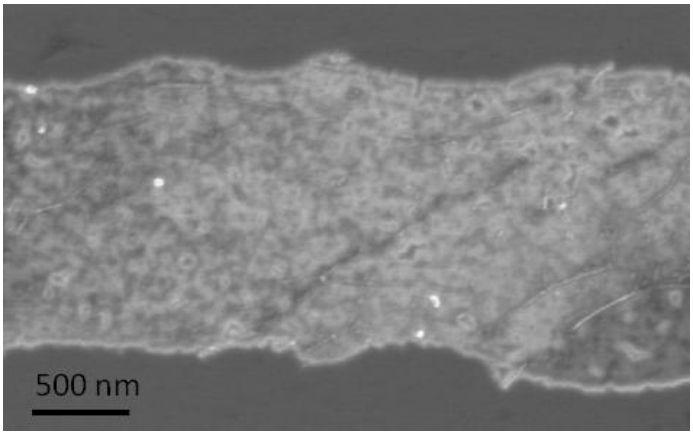

Figure 7.7: Shows zoom-in SEM image of single ribbon.

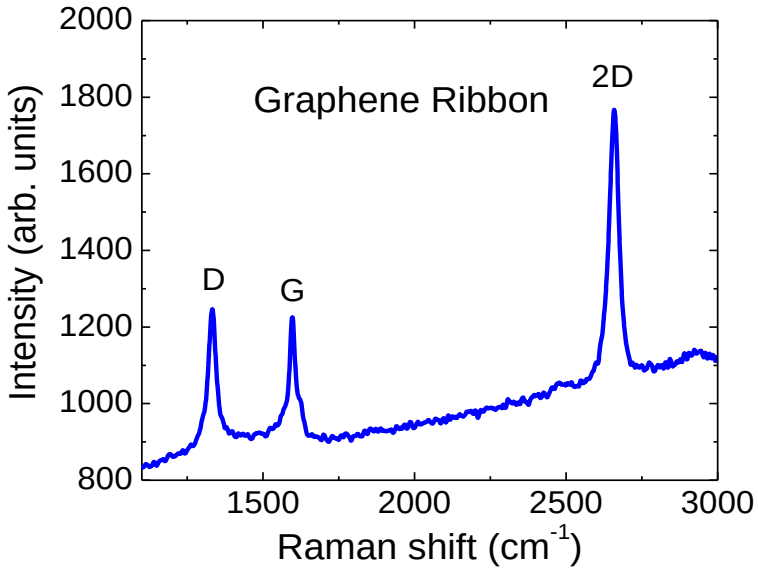

Figure 7.8: Shows Raman spectrum of graphene ribbon.

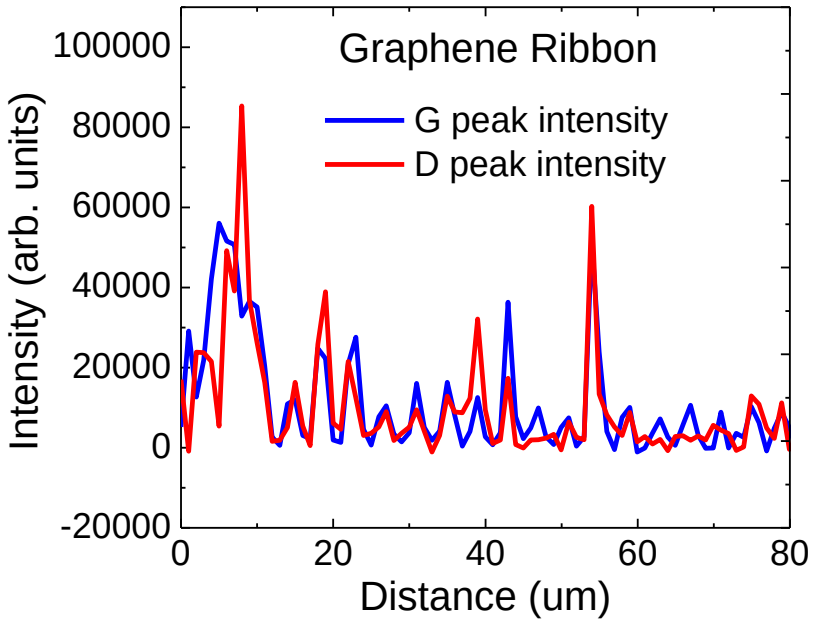

Figure 7.9: Shows typical line scan results for the G and D peak intensities for graphene ribbon sensor.

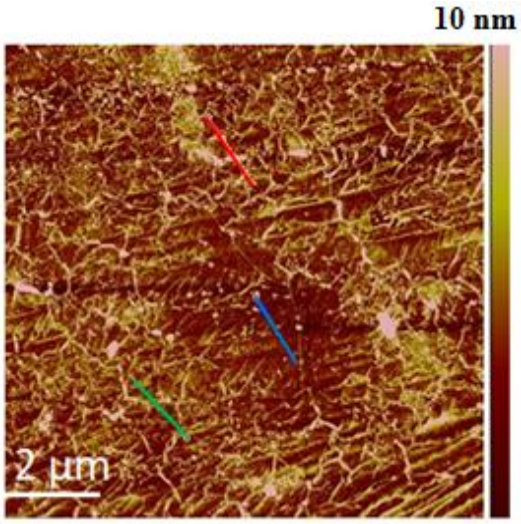

Figure 7.10: Shows an AFM image of the CVD based extended graphene.

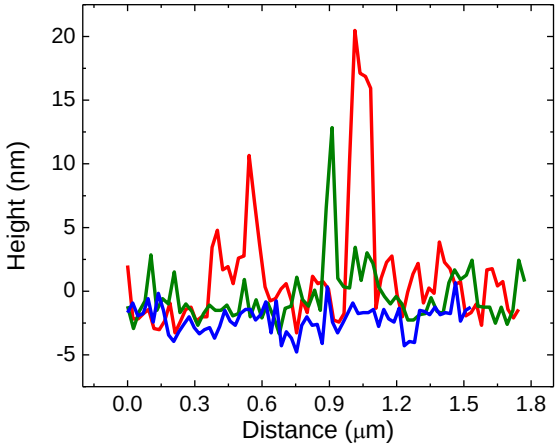

Figure 7.11: Shows profile of topography along three red, blue and green lines in Figure 7.10.

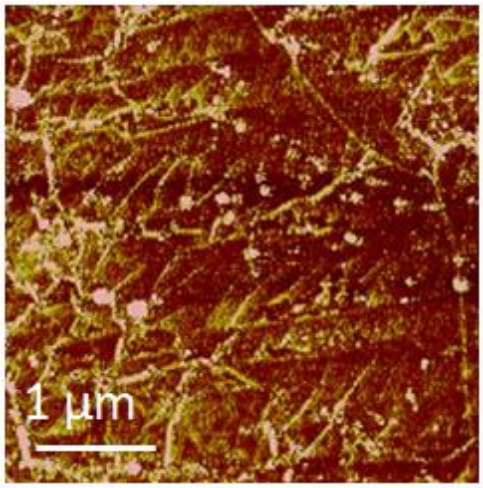

Figure 7.12: Shows close view of AFM image for CVD based extended graphene.

7.5 Evaluate the Effect of PMMA on Sensing Response of CVD Graphene

Studies done have shown that polymer residues could unintentionally functionalize graphene sensors by providing a surface phase in which the gas molecules can adsorb and influence charge transfer from the gas to the graphene or vice versa.[15, 46, 47] The polymer residue is fairly common when lithographic resists (PMMA) are used. Studies[46] were done to confirm the effects of polymer residues on graphene gas sensors using mechanically exfoliated graphene before and after removal of PMMA residues. Commonly, PMMA were rid of by resist stripper or acetone. However, it has been confirmed the residues left behind after processing. It has been suggested further cleaning procedure can get rid of PMMA completely and leaving the graphene surface clean. The process[46] is through heating graphene to 400 Celsius in a reducing H_2/Ar

atmosphere for 1 hr. The electrical quality of the devices improved as carrier mobility increased by four times and the doped carrier density was reduced by nearly 70%.

Experiments were set up to evaluate the effect of PMMA residue after processing on the gas sensing performances for CVD extended graphene and graphene ribbons. One set of sensors undergo normal acetone dissolving PMMA clean process (PMMA/Graphene) and the other set with extended cleaning procedure of thermal treatment at 400 Celsius in H_2/Ar atmosphere for 1 hour (P-type Graphene).

Figure 7.13 and 7.14 compares the response of the two different chemiresistors to a 100 millisecond pulse of toluene (an electron donor) and of 1,2-dichlorobenzene (an electron acceptor). In each case, we chose the number of molecules in the pulse to be similar to the number of molecules produced by our preconcentrator[48] with sampling air containing 300 ppb of analyte. Notice that we find little or no response with the pristine graphene sample, but a large response (up to a 50x improvement) with the defective and polycrystalline samples. Clearly, the addition of line defects (and perhaps point defects) has enhanced the sensor response.

Adsorbed water is a surface impurity on graphene based gas sensors as it can cause indirect doping of graphene by water from the ambient. Therefore, even if water not initially present on graphene, the water molecules might diffuse into graphene upon exposure to humid air. Thereby resulting in P-type doping of graphene by ambient water molecules.[49] Our results on Figure 7.13 and 7.14 confirmed the sensors are indeed P-type as both Toluene and 1,2-dichlorobenzene exposure lead to further increase in conductivity.

From Figure 7.13, it appears that PMMA residue increased the sensitivity of the PMMA/graphene sensor greatly when the sensor were exposed with toluene gas. From Figure 7.14, PMMA residue did not lead to increase in sensitivity as both P-type graphene sensors (patch and ribbons) exhibit larger sensitivity compared to PMMA/graphene ones. Previous study[17] used pristine mechanically exfoliated graphene samples for testing against various molecules on the effect of PMMA residue. It was not surprising that they did not observe any response with cleaned graphene sensors and concluded PMMA was the reason for the sensor responses. However, our graphene samples have defect sites to allow molecules to be adsorbed, so it was not surprising to observe sensor responses with our graphene sensors.

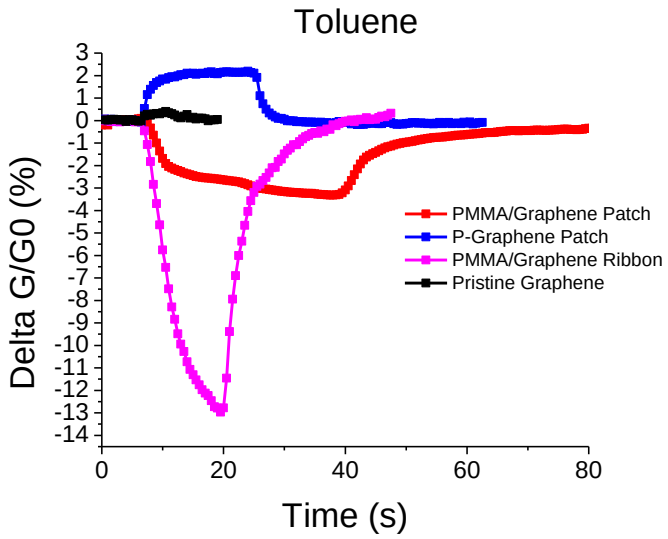

Figure 7.13: Typical response of P-type cleaned extended (CVD-grown defective) graphene and PMMA residue graphene (PMMA/graphene), P-type graphene ribbon and PMMA/graphene ribbon, and a 5 µm wide pristine graphene sensors to 10^{14} molecules of toluene. The pulses are similar to those produced by a preconcentrator[48] sampling air containing 300 ppb of analyte.

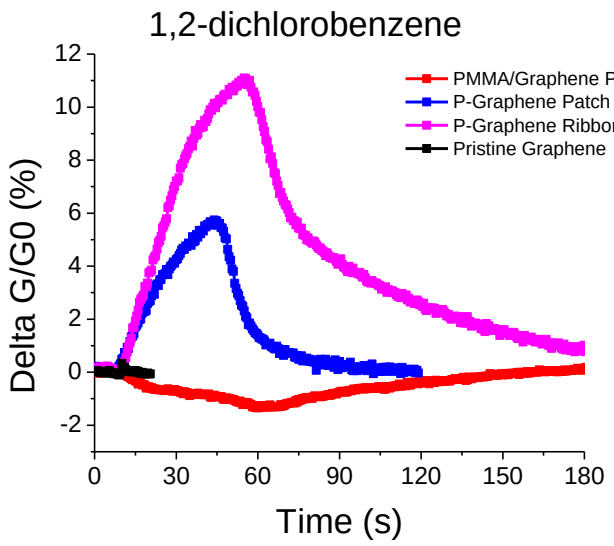

Figure 7.14: Typical response of P-type cleaned extended (CVD-grown defective) graphene and PMMA residue graphene (PMMA/graphene), P-type graphene ribbon and PMMA/graphene ribbon, and a 5 µm wide pristine graphene sensors to 10^{15} molecules of 1,2-dichlorobenzene. The pulses are similar to those produced by a preconcentrator[48] sampling air containing 300 ppb of analyte.

7.6 Evaluate the Effect of Edges on Sensing Response of CVD Graphene Ribbons

We have demonstrated the effect of PMMA residue during processing on the sensor performance of graphene sensors. Now we want to eliminate the PMMA variable. Therefore, experiments were done with only cleaned graphene samples after following the extra cleaning procedure with thermal treatments. We wanted to further elucidate the role of line defects on the behavior of our sensors. The experiment was to cut the sample into ribbons that were 2 to 5 µm across, as shown in Figure 7.4.F. By way of background, when a graphene sheet is cut into ribbons with dimensions similar to those of the line defects, edges are created that cross the line

defects as illustrated in Figure 7.16.C. The edges have a high resistance, so very little current flows through them. Consequently, when an edge crosses a line defect, the leakage current around the sides of the line defect is eliminated. Instead, electric field lines bunch up around the line defect as illustrated in Figure 7.16.C. Thus, the edge should enhance the effects of the line defects, provided the length of the line defects is similar to the distance between the edges. Point defects should be hardly affected since most of the point defects are far away from the edges. Further, very little current flows through the edges, so edges alone should only have a small effect on the sensor response unless adjacent edges are within the electron mean free path.

Our pristine (crystalline) graphene ribbon chemiresistor is only ~1 μm wide, yet we observe negligible response showing that the combination of narrowly spaced edges and a few point defects is insufficient to cause a significant sensor response. In contrast, when the defective graphene sheets with existing line defects are cut into 2 μm wide ribbons the chemiresistor response increases by a factor of 2 to 4 as shown in Figures 7.13, 7.14 and 7.15. The sensitivity is enhanced into the parts per billion (ppb) range. Clearly, the combination of edges and line defects enhances the response of the sensor, compared to edges or line defects alone. Further, this experiment proves that in our samples the line defects have a large effect on the response because cutting the graphene into ribbons should only affect the line defects and not the point defects.

Figure 7.15 also compares the response of the graphene micro-ribbon chemiresistors to CNT chemiresistors. In each case we plot the average response of five different sensors. Notice that the sensor response exceeds that of CNT chemiresistors, showing that graphene sensors with confined line defects are superior.

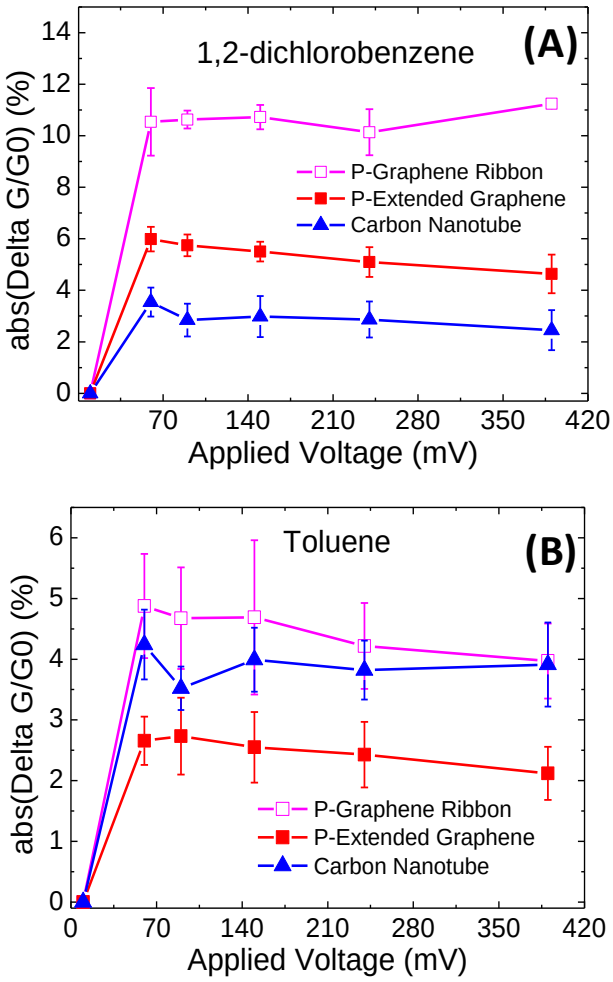

Figure 7.15: (A-B) display the expanded response of P type graphene ribbon, P type extended graphene, and CNT sensors to 1,2-dichlorobenzene and toluene molecules, respectively, as a function of applied voltage. It is seen that the sensor does not show any detectable response at low voltage, but it turns on when the applied voltage exceeds 50 mV. Details of the jump in sensitivity have been described previously[50]. The P type graphene ribbon shows the response to 1,2-dichlorobenzene is 3-4 times higher than that of CNT sensors and 2 times higher than that of P type extended graphene sensors. The ribbon sensors also show higher response to toluene molecules compared to CNT based and extended graphene sensors.

7.7 COMSOL Finite Element Simulation of Electric Field on Graphene Sheet

Calculations were done to understand how conduction in a two-dimensional conductor would be affected by the adsorption of an analyte. Figure 7.16.A shows the results of a COMSOL finite element simulation of the electric field in a graphene sheet with one hundred 30 nm wide islands containing analyte. We assumed that the analyte would increase the local resistance of the graphene by 200 times (*i.e.* much more than that one might expect), and did calculations to determine whether there was a significant change in the resistance of the overall device. Surprisingly there was very little effect. The electric field lines hardly changed, and there was little change in the overall resistance of the device.

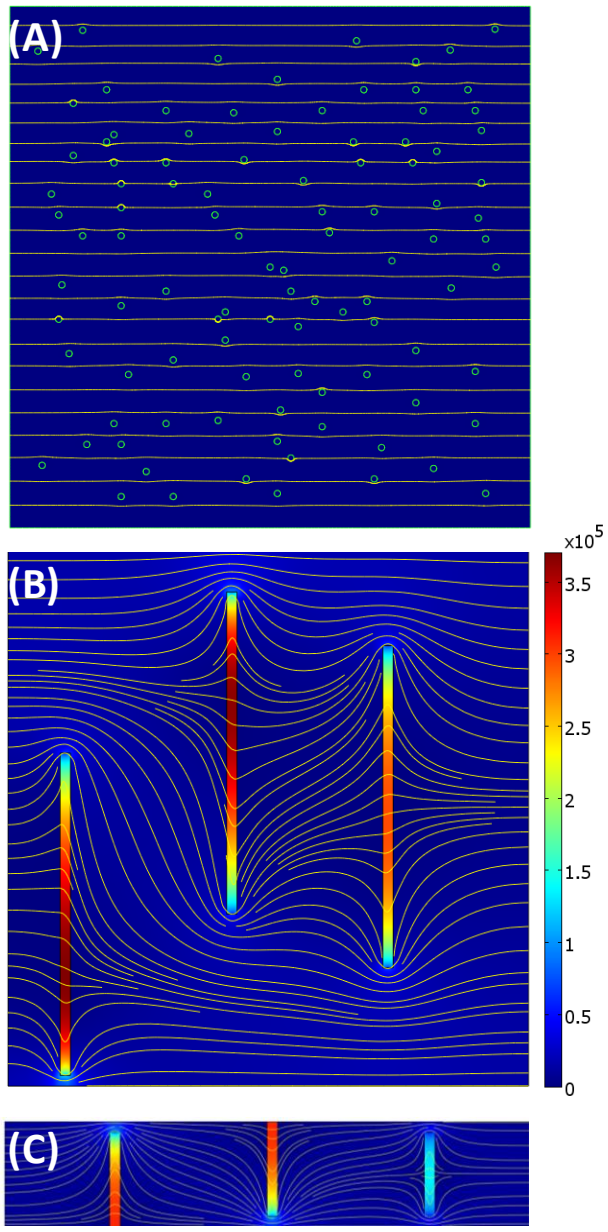

Figure 7.16: Finite-element simulation of electric field distribution in: (A) 5×5 µm graphene sample with 100 point defects of 30 nm size, (B) same graphene sample as in (A) with 3 line defects of 0.1×3 µm, and, (C) 1×5 µm graphene ribbon with two line defects of 0.1×0.9 µm and a third of 0.1×0.8 µm. The graphene sheet resistance is 6×10^{-6} Ω·cm and defect resistance is 200 times higher. The color bar shows the electric field strength, whereas the streamlines indicate the current density.

Physically, electrons take the path of lowest resistance in carbon devices,[33] as in other materials. An isolated point defect or other localized chemisorption site does not lead to a significant change in the resistance of the chemiresistor because there is still a low resistance pathway for electron conduction in analyte-free regions of the graphene. In effect the low resistance pathways short-circuit the analyte. As a result, according to our calculations, a localized change in the graphene resistance due to adsorption of an analyte will not have a significant effect on the chemiresistor response unless the analyte concentration is very high. This explains why pristine graphene (*i.e.* monocrystalline and without defects) is insensitive to analytes.

Next we considered what could be done to enhance the sensitivity. Point defects are known to enhance the sensitivity on CNT chemiresistors[33, 50-52] but point defects can also be short circuited in graphene, in a matter similar to that shown in Figure 7.16.A. According to the calculations of Jafri *et al.*,[53] changing the concentrations of point defects from 0.01 to 0.05 does not make a substantial difference in the resistance of graphene. Consequently, even if one changed half of the point defects *via* gas adsorption, it may not make a large difference to the overall resistance of a graphene chemiresistor.

On the other hand, line defects, such as those observed by previous investigators[34, 36-38, 43] could have a much stronger effect on the resistance of graphene. An *et al.*[43] showed that analytes bind strongly to line defects and the pathways around the defects are long enough that it would be difficult to short circuit. Figure 7.16.B shows a simulation of the effect of line defects on the current flow through the chemiresistor. Notice that, according to the calculations, the presence of line defects or a closely spaced line of point defects greatly perturbs the conduction through the chemiresistor. Line defects are needed because graphene is a two-dimensional conductor.

Theoretically, one would expect anything that changes the resistance of the line defect, such as adsorption on the line, to have an important effect on the resistance of the chemiresistor.

The results in Figure 7.16.A and 7.16.B provide the basis for our understanding of the graphene chemiresistor response. According to this model, pristine graphene or graphene with only point defects should be insensitive to the adsorption of gas, because adsorbed molecules or point defects are easily short circuited given the two-dimensional nature of graphene. In contrast, line defects should be quite effective in promoting chemiresistor response.

7.8 Conclusion

The implications of our results are that the best graphene chemiresistors are perfectly imperfect with the right types of defects to promote a fast response. Pristine graphene is largely insensitive to analyte molecules because adsorbates bind to point defects,[43] but at the typical defect concentrations in graphene chemiresistors, there are low resistance pathways around such defects. As a result, adsorption at point defects only has a small effect on the overall resistance of the device.[53] On the other hand, micron-sized line defects or continuous lines of point defects are different because no easy conduction paths exist around such defects, so the resistance change after adsorption is significant. Therefore, we conclude that the two-dimensional nature of defective, CVD-grown graphene chemiresistors causes them to behave differently than CNT chemiresistors. Moreover, this sensitivity is further improved by cutting the graphene into ribbons of width comparable to the line defect dimensions (microns). Thus, the best graphene sensors are perfectly imperfect, *i.e.* line defects and edges can be engineered to significantly enhance the graphene chemiresistor sensitivity.

7.9 References

1. Soldano, C.; Mahmood, A.; Dujardin, E., Production, Properties and Potential of Graphene. *Carbon* **2010,** *48* (8), 2127-2150.
2. Rao, C. N. R.; Sood, A. K.; Voggu, R.; Subrahmanyam, K. S., Some Novel Attributes of Graphene. *J. Phys. Chem. Lett.* **2010,** *1* (2), 572-580.
3. Mucciolo, E. R.; Lewenkopf, C. H., Disorder and Electronic Transport in Graphene. *J. Phys.: Condens. Matter* **2010,** *22* (27), 273201/1-273201/12.
4. Das, S. S.; Adam, S.; Hwang, E. H.; Rossi, E., Electronic Transport in Two Dimensional Graphene. *arXiv.org, e-Print Arch., Condens. Matter* **2010**, 1-85, arXiv:1003.4731v1 [cond-mat.mes-hall].
5. Allen, M. J.; Tung, V. C.; Kaner, R. B., Honeycomb Carbon: A Review of Graphene. *Chem. Rev. (Washington, DC, U. S.)* **2010,** *110* (1), 132-145.
6. Abergel, D. S. L.; Apalkov, V.; Berashevich, J.; Ziegler, K.; Chakraborty, T., Properties of Graphene: A Theoretical Perspective. *Adv. Phys.* **2010,** *59* (4), 261-482.
7. Wakabayashi, K.; Takane, Y.; Yamamoto, M.; Sigrist, M., Electronic Transport Properties of Graphene Nanoribbons. *New J. Phys.* **2009,** *11* (Sept.), 095016.
8. Rao, C. N. R.; Sood, A. K.; Subrahmanyam, K. S.; Govindaraj, A., Graphene: The New Two-Dimensional Nanomaterial. *Angew. Chem., Int. Ed.* **2009,** *48* (42), 7752-7777.
9. Novoselov, K. S.; Geim, A. K.; Morozov, S. V.; Jiang, D.; Katsnelson, M. I.; Grigorieva, I. V.; Dubonos, S. V.; Firsov, A. A., Two-Dimensional Gas of Massless Dirac Fermions in Graphene. *Nature* **2005,** *438* (7065), 197-200.

10. Geim, A. K.; Novoselov, K. S., The Rise of Graphene. *Nature Materials* **2007,** *6* (3), 183-191.

11. Bolotin, K. I.; Sikes, K. J.; Jiang, Z.; Klima, M.; Fudenberg, G.; Hone, J.; Kim, P.; Stormer, H. L., Ultrahigh Electron Mobility in Suspended Graphene. *Solid State Communications* **2008,** *146* (9-10), 351-355.

12. Novoselov, K. S.; McCann, E.; Morozov, S. V.; Fal'ko, V. I.; Katsnelson, M. I.; Zeitler, U.; Jiang, D.; Schedin, F.; Geim, A. K., Unconventional Quantum Hall Effect and Berry's Phase of 2ï€ in Bilayer Graphene. *Nature Physics* **2006,** *2* (3), 177-180.

13. Stander, N.; Huard, B.; Goldhaber-Gordon, D., Evidence for Klein Tunneling in Graphene P-N Junctions. *Physical Review Letters* **2009,** *102* (2).

14. Young, A. F.; Kim, P., Quantum Interference and Klein Tunnelling in Graphene Heterojunctions. *Nature Physics* **2009,** *5* (3), 222-226.

15. Schedin, F.; Geim, A. K.; Morozov, S. V.; Hill, E. W.; Blake, P.; Katsnelson, M. I.; Novoselov, K. S., Detection of Individual Gas Molecules Adsorbed on Graphene. *Nature Materials* **2007,** *6* (9), 652-655.

16. Geim, A. K., Graphene: Status and Prospects. *Science* **2009,** *324* (5934), 1530-1534.

17. Dan, Y.; Lu, Y.; Kybert, N. J.; Luo, Z.; Johnson, A. T. C., Intrinsic Response of Graphene Vapor Sensors. *Nano Lett.* **2009,** *9* (4), 1472-1475.

18. Fowler, J. D.; Allen, M. J.; Tung, V. C.; Yang, Y.; Kaner, R. B.; Weiller, B. H., Practical Chemical Sensors from Chemically Derived Graphene. *ACS Nano* **2009,** *3* (2), 301-306.

19. Huang, B.; Li, Z.; Liu, Z.; Zhou, G.; Hao, S.; Wu, J.; Gu, B.-L.; Duan, W., Adsorption of Gas Molecules on Graphene Nanoribbons and Its Implication for Nanoscale Molecule Sensor. *J. Phys. Chem. C* **2008,** *112* (35), 13442-13446.

20. Joshi, R. K.; Gomez, H.; Alvi, F.; Kumar, A., Graphene Films and Ribbons for Sensing of O2, and 100 Ppm of Co and No2 in Practical Conditions. *J. Phys. Chem. C* **2010,** *114* (14), 6610-6613.

21. Moradian, R.; Mohammadi, Y.; Ghobadi, N., Investigation of Gas Sensing Properties of Armchair Graphene Nanoribbons. *J. Phys.: Condens. Matter* **2008,** *20* (42), 425211/1-425211/12.

22. Shao, Y.; Wang, J.; Wu, H.; Liu, J.; Aksay, I. A.; Lin, Y., Graphene Based Electrochemical Sensors and Biosensors: A Review. *Electroanalysis* **2010,** *22* (10), 1027-1036.

23. Yang, W.; Ratinac, K. R.; Ringer, S. P.; Thordarson, P.; Gooding, J. J.; Braet, F., Carbon Nanomaterials in Biosensors: Should You Use Nanotubes or Graphene? *Angew Chem Int Ed Engl* **2010,** *49* (12), 2114-38.

24. Zhang, Y.-H.; Chen, Y.-B.; Zhou, K.-G.; Liu, C.-H.; Zeng, J.; Zhang, H.-L.; Peng, Y., Improving Gas Sensing Properties of Graphene by Introducing Dopants and Defects: A First-Principles Study. *Nanotechnology* **2009,** *20* (18), 185504/1-185504/8.

25. Robinson, J. T.; Perkins, F. K.; Snow, E. S.; Wei, Z.; Sheehan, P. E., Reduced Graphene Oxide Molecular Sensors. *Nano Letters* **2008,** *8* (10), 3137-3140.

26. Cheng, Z.; Li, Q.; Li, Z.; Zhou, Q.; Fang, Y., Suspended Graphene Sensors with Improved Signal and Reduced Noise. *Nano Lett* **2010,** *10* (5), 1864-8.

27. Guo, C. X.; Lu, Z. S.; Lei, Y.; Li, C. M., Ionic Liquid-Graphene Composite for Ultratrace Explosive Trinitrotoluene Detection. *Electrochem. Commun.* **2010,** *12* (9), 1237-1240.

28. Ratinac, K. R.; Yang, W.; Ringer, S. P.; Braet, F., Toward Ubiquitous Environmental Gas Sensors-Capitalizing on the Promise of Graphene. *Environ. Sci. Technol.* **2010,** *44* (4), 1167-1176.

29. Capone, S.; Forleo, A.; Francioso, L.; Rella, R.; Siciliano, P.; Spadavecchia, J.; Presicce, D. S.; Taurino, A. M., Solid State Gas Sensors: State of the Art and Future Activities. *Journal of Optoelectronics and Advanced Materials* **2003,** *5* (5), 1335-1348.

30. Kong, J.; Franklin, N. R.; Zhou, C.; Chapline, M. G.; Peng, S.; Cho, K.; Dai, H., Nanotube Molecular Wires as Chemical Sensors. *Science* **2000,** *287* (5453), 622-625.

31. Moseley, P. T., Solid State Gas Sensors. *Measurement Science and Technology* **1997,** *8* (3), 223-237.

32. Zettl, A., Extreme Oxygen Sensitivity of Electronic Properties of Carbon Nanotubes. *Science* **2000,** *287* (5459), 1801-1804.

33. Salehi-Khojin, A.; Khalili-Araghi, F.; Kuroda, M.; Lin, K. Y.; Jean-Pierre Leburton; Masel, R. I., On the Sensing Mechanism in Carbon Nanotube Chemical Sensors *ACS Nano* **2010,** (Submitted).

34. Lahiri, J.; Lin, Y.; Bozkurt, P.; Oleynik, I. I.; Batzill, M., An Extended Defect in Graphene as a Metallic Wire. *Nat Nano* **2010,** *5* (5), 326-329.

35. Koepke, J.; Estrada, D.; Wood, J. D.; Pop, E.; Joseph, L. In *Scanning Tunneling Microscopy Study of Grain Boundaries in Graphene Grown by Chemical Vapor Deposition on Copper Foil*, American Physical Society March Meeting, 2011.

36. Liu, Y.; Yakobson, B. I., Cones, Pringles, and Grain Boundary Landscapes in Graphene Topology. *Nano Letters* **2010,** *10* (6), 2178-2183.

37. Huang, P. Y.; Ruiz-Vargas, C. S.; van der Zande, A. M.; Whitney, W. S.; Levendorf, M. P.; Kevek, J. W.; Garg, S.; Alden, J. S.; Hustedt, C. J.; Zhu, Y.; Park, J.; McEuen, P. L.; Muller, D. A., Grains and Grain Boundaries in Single-Layer Graphene Atomic Patchwork Quilts. *Nature 469* (7330), 389-392.

38. Kim, K.; Lee, Z.; Regan, W.; Kisielowski, C.; Crommie, M. F.; Zettl, A., Grain Boundary Mapping in Polycrystalline Graphene. *ACS Nano,* null-null.

39. Dorgan, V. E.; Bae, M.-H.; Pop, E., Mobility and Saturation Velocity in Graphene on Sio2. *Appl. Phys. Lett.* **2010,** *97* (8), 082112/1-082112/3.

40. Bae, S.; Kim, H.; Lee, Y.; Xu, X.; Park, J.-S.; Zheng, Y.; Balakrishnan, J.; Lei, T.; Ri Kim, H.; Song, Y. I.; Kim, Y.-J.; Kim, K. S.; Ozyilmaz, B.; Ahn, J.-H.; Hong, B. H.; Iijima, S., Roll-to-Roll Production of 30-Inch Graphene Films for Transparent Electrodes. *Nat Nano* **2010,** *5* (8), 574-578.

41. Kim, K. S.; Zhao, Y.; Jang, H.; Lee, S. Y.; Kim, J. M.; Kim, K. S.; Ahn, J.-H.; Kim, P.; Choi, J.-Y.; Hong, B. H., Large-Scale Pattern Growth of Graphene Films for Stretchable Transparent Electrodes. *Nature* **2009,** *457* (7230), 706-710.

42. Li, X.; Cai, W.; An, J.; Kim, S.; Nah, J.; Yang, D.; Piner, R.; Velamakanni, A.; Jung, I.; Tutuc, E.; Banerjee, S. K.; Colombo, L.; Ruoff, R. S., Large-Area Synthesis of High-Quality and Uniform Graphene Films on Copper Foils. *Science* **2009,** *324* (5932), 1312-1314.

43. An, J.; Voelkl, E.; Suk, J.; Li, X.; Magnuson, C. W.; Fu, L.; Tiemeijer, P.; Bischoff, M.; Freitag, B.; Popova, E.; Ruoff, R. S., Domain (Grain) Boundaries and Evidence of Twin Like Structures in Cvd Grown Graph. *arXiv.org, e-Print Arch., Condens. Matter* **2010**, arXiv:1010.3905v1 [cond-mat.mtrl-sci].

44. Malard, L. M.; Pimenta, M. A.; Dresselhaus, G.; Dresselhaus, M. S., Raman Spectroscopy in Graphene. *Phys. Rep.* **2009,** *473* (5-6), 51-87.

45. Cancado, L. G.; Takai, K.; Enoki, T.; Endo, M.; Kim, Y. A.; Mizusaki, H.; Jorio, A.; Coelho, L. N.; Magalhaes-Paniago, R.; Pimenta, M. A., General Equation for the Determination of the Crystallite Size L[Sub a] of Nanographite by Raman Spectroscopy. *Applied Physics Letters* **2006,** *88* (16), 163106-3.

46. Dan, Y.; Lu, Y.; Kybert, N. J.; Luo, Z.; Johnson, A. T. C., Intrinsic Response of Graphene Vapor Sensors. *Nano Letters* **2009,** *9* (4), 1472-1475.

47. Ishigami, M.; Chen, J. H.; Cullen, W. G.; Fuhrer, M. S.; Williams, E. D., Atomic Structure of Graphene on Sio2. *Nano Letters* **2007,** *7* (6), 1643-1648.

48. Ni, Z.; Jerrell, J. P.; Cadwallader, K. R.; Masel, R. I., Metal-Organic Frameworks as Adsorbents for Trapping and Preconcentration of Organic Phosphonates. *Analytical Chemistry* **2007,** *79* (4), 1290-1293.

49. Romero, H. E.; Joshi, P.; Gupta, A. K.; Gutierrez, H. R.; Cole, M. W.; Tadigadapa, S. A.; Eklund, P. C., Adsorption of Ammonia on Graphene. *Nanotechnology* **2009,** *20* (24).

50. Salehi-Khojin, A.; Field, C. R.; Yeom, J.; Shannon, M. A.; Masel, R. I., Sensitivity of Nanotube Chemical Sensors at the Onset of Poole-Frenkel Conduction *Appl. Phys. Lett.* **2010,** *96*, 163110-163113.

51. Robinson, J. A.; Snow, E. S.; BÇŽdescu, Å. C.; Reinecke, T. L.; Perkins, F. K., Role of Defects in Single-Walled Carbon Nanotube Chemical Sensors. *Nano Lett.* **2006,** *6* (8), 1747-1751.

52. Salehi-Khojin, A.; Lin, K. Y.; Field, C. R.; Masel, R. I., Nonthermal Current-Stimulated Desorption of Gases from Carbon Nanotubes. *Science (Washington, DC, U. S.)* **2010,** *329* (5997), 1327-1330.

53. Jafri, S. H. M.; Carva, K.; Widenkvist, E.; Blom, T.; Sanyal, B.; Fransson, J.; Eriksson, O.; Jansson, U.; Grennberg, H.; Karis, O.; Quinlan, R. A.; Holloway, B. C.; Leifer, K., Conductivity Engineering of Graphene by Defect Formation. *J. Phys. D: Appl. Phys.* **2010,** *43* (4), 045404/1-045404/8.

Chapter 8: Room Temperature Gas Sensors Based on Randomly Stacked Oxide-Free Graphene Films

We explore the simple chemiresistor based gas sensors with randomly stacked oxide free graphene film fabricated using surfactant assisted exfoliation of graphite and tested for target gas molecule sensitivity. Vacuum filtration is used to produce various thickness of graphene films at different filtration volumes. Stamp printing technique was used to deposit graphene film on top of electrode gap in order to avoid polymer resist contaminates on the sensor. At low filtration volumes, oxide free randomly stacked graphene film sensors showed better sensitivity towards target molecules compared to polycrystalline/ribbon graphene and defective CNT gas sensors. As the graphene film thickness increases, there is a shift in conduction mechanism from 2D electron hopping to metallic like conduction which explains the drop in sensitivity as the filtration volume increases. This chapter contains an expanded version of a future publication: Kevin Y. Lin, A. Salehi-Khojin, D. Estrada, E. Pop, R.I. Masel. "Randomly Stacked Oxide-free Graphene Film as Chemiresistors."

8.1 Background on Graphene

Graphene has a basic structure of one atom thick two dimensional sheet of sigma bond covalently attached of carbon atoms packed in a honeycomb crystal lattice. Its delocalized pi bonds give rise to exceptional electronic properties.[1-14] Graphene shows potential for gas sensor

applications due to two main advantages as compared to other solid state sensors. Graphene has a two dimensional structure which gives rise to highest sensing area per unit volume as the entire surface atoms are exposed to the adsorbed gas molecules. Other benefit for its two dimensional nature includes the ability to screen charge fluctuations, more so than the comparative 1-dimensional carbon nanotubes.[15] Therefore Electric transport through graphene can be sensitive to the adsorption of analyte molecules. Further, graphene exhibits lower 1/f noise level compared to other solid state sensors.[16-20] Single molecule detection and low detection noise have been reported[15] with mono layer mechanically exfoliated graphene gas sensors making it possible to have low power and room temperature gas sensors.

Graphene can be produced via various physical and chemical routes. Mechanical cleaving of graphite gives near ideal pristine graphene crystal structure.[21] Epitaxial growth of graphene on SiC[22, 23] and chemical vapor deposition on metal substrates such as copper[24] and nickel[25] have all been reported to produce large area graphene films. However, the above mentioned methods all have disadvantages (inefficient process, high temperature and vacuum process, and contaminations during processing respectively) that render them not ideal in mass producing graphene based gas sensors. Recent efforts are on wet chemical based routes which can produce graphene in a cost effective manner and can be mass produced. The most popular is chemically modified graphene approach[26-28] where graphene oxide is first produced via oxidation through chemical exfoliation of graphite and then reduced to obtain graphene. However this process can produce oxygen and nitrogen based impurities which might be difficult to control.[29, 30] Additional variables include the methods used to reduce graphene oxide as chemical reducing agent and thermal reducing can produce different types of graphene films.

8.2 Previous Works on Graphene Based Gas Sensors

There have been reports on graphene based sensors made via mechanical exfoliation,[15, 31] epitaxial growth,[32] chemical vapor deposition[33] and graphene oxide routes.[16, 26-28] However, there have been no reports on graphene based sensors made from surfactant/solvent exfoliated method. Surfactant/solvent exfoliated graphene[34-36] is gaining traction as an alternative to graphene oxide method which produces no oxides on graphene film and requires no extreme temperature and harsh chemical reducing agents during processing. Vacuum filtration technique has been shown to produce uniform and controllable thickness thin graphene films.[35, 37, 38] It has been recently reported PMMA residues can have profound effects on gas sensing for graphene based gas sensors.[31] However, with stamp printing process,[39, 40] residual polymer contaminations can be avoided.

8.3 Objective

The objective of this work is the development of gas sensors from surfactant sodium cholate exfoliated graphene. The approach is to use vacuum filtration to create a randomly stacked oxide free graphene film and through stamp printing technique to deposit on the silicon substrates to give rise to the chemiresistor based gas sensors. It would be important to determine how charge transport occurs with this randomly stacked oxide free graphene film which is an electronically and structurally inhomogeneous system (overlapping graphene islands) as well as how such affects the gas sensing properties of the sensors.

8.4 Experimental Procedures

Materials. Graphite (flakes) and sodium cholate surfactant (BioXtra, ≥99%) were purchased from Sigma-Aldrich.

Fabrication and Design of the Sensor. Randomly stacked oxide free graphene sensors were fabricated using standard lift-off photolithography procedure. A silicon substrate with thermal oxide layer (500/0.5 µm Si/SiO_2) was patterned with chromium and gold (10/100 nm Cr/Au) as source and drain electrodes separated by a 6 µm gap. 1% 3-aminopropyltriethoxysilane (APTES) (Gelest, Inc) was utilized as a supportive coating to enhance the interaction between randomly stacked graphene film and silicon substrate (Figure 8.1).

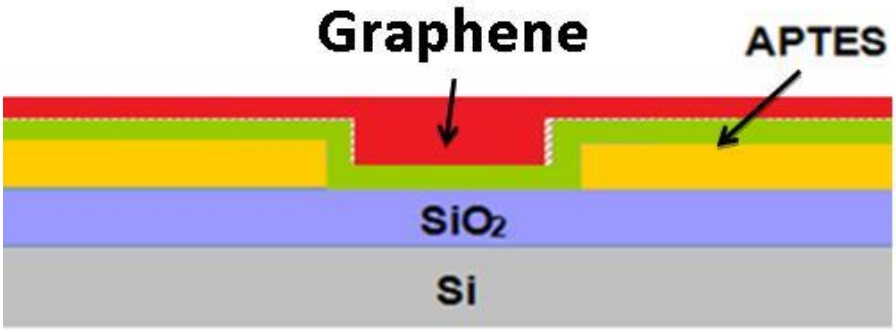

Figure 8.1: Schematic diagram depicting various layers on the gas sensor device.

Randomly Stacked Oxide Free Graphene Film Preparation and Deposition on Silicon Substrate. Excess graphite flakes (1.5 g) (Figure 8.2) was dispersed in 0.5% (w/v) sodium cholate in Millipore water (100 mL). 60-minutes low-powered ultrasonication was performed to

exfoliate graphite to graphene. After 90-minutes centrifugation (at 500 RPM), the top 80% of supernatant was decanted and retained for use (Figure 8.3).

Figure 8.2: Photograph showing the starting material natural graphite powder used.

Figure 8.3: Photograph showing the graphene dispersion after ultrasonication with the horn tip using surfactant sodium cholate assisted exfoliation of graphite (left vial) and graphene dispersion after centrifuge and decanting (right vial).

The resulting dispersions were vacuum filtrated at different volumes with mixed cellulose ester (MCE) membranes (Millipore, 0.22 micron pore size) to give a randomly stacked graphene films (Figure 8.4). After graphene was successfully deposited onto the membranes, the wet MCE-graphene membrane was dried out for at least 2 hours under 15 in-Hg gauge pressures before multiple rinsing with approximately 80 mL of purified and deionized water (Millipore, MilliQ water). Multiple rinsing was intended to remove the sodium cholate residue completely from the MCE-graphene membrane. Finally, stamp technique was used to transfer homogeneous and randomly stacked graphene films to the APTES treated silicon surface (Figure 8.5).

Figure 8.4: Photograph showing the 3 ml filtration volume randomly stacked oxide-free graphene film after vacuum filtration.

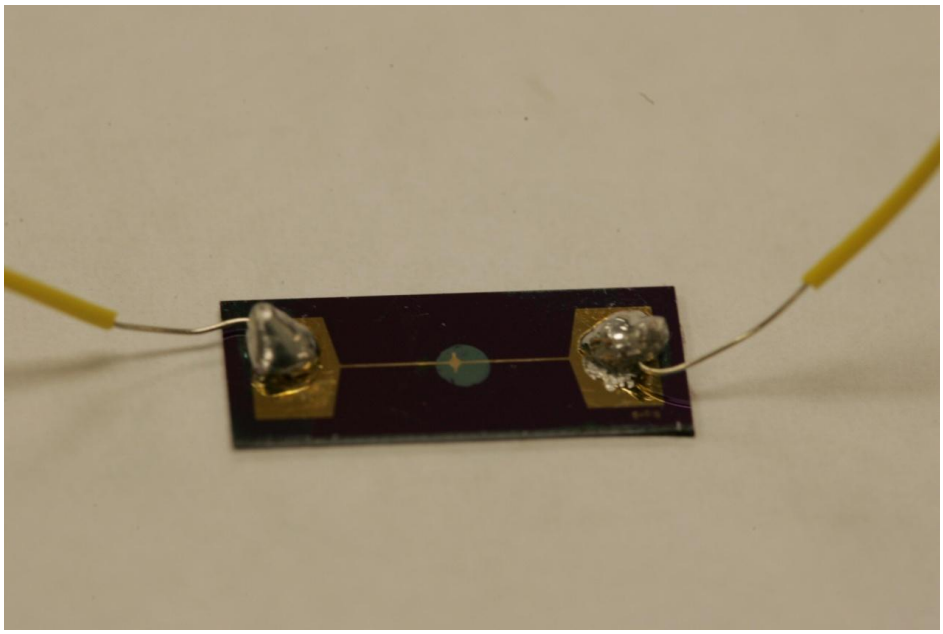

Figure 8.5: Photograph showing the 5 ml filtration volume randomly stacked oxide-free graphene gas sensor after stamp-printing technique to deposit thin graphene film onto of silicon substrate.

Raman spectra were collected using a Renishaw confocal microscope with 633 nm excitation laser.

Sensor Testing and Measurement. Sensors were placed in a custom built PEEK (polyaryletheretherketone) flow cell and a fused silica passivated capillary was used to connect to a Gas Chromatograph (GC) inlet. An Agilent 6893N GC/FID-MS with 7683B auto-sampler with a pulse of 100 ms was used to deliver target gas molecules to the sensors at pressure of 3.6 psi for all experiments. Ultra pure helium gas was used as a carrier gas at fixed flow rate. A VoltaLab 10 potentiostat (PGZ100) was used to monitor the change in potential on the sensors upon exposure to trace gas vapors.

8.5 Characterizations on Randomly Stacked Oxide-Free Graphene Films

Our graphene sensors consist of a randomly stacked oxide free graphene film deposited between two gold contacts separated by 6 µm. Vacuum filtration method was used to produce uniform graphene films at different filtration volume. The stamp printing method was then used to transfer randomly stacked oxide free graphene film to silicon substrate. Figure 8.1 shows the schematic of cross section of the randomly stacked oxide free graphene sensor. Figure 8.6, 8.7 and 8.8 shows the scanning electron microscopy (SEM) images of the graphene film at different filtration volume (3 ml, 5 ml, 10 ml), respectively. From the SEM images, it can be seen the films go from sparsely distributed to dense film as graphene concentrations increase. It has been reported that for thin carbon films less than 20 nm, it is common to get non-uniform film as it is more favorable to aggregate layer by layer sparsely rather than spread out to form a uniform film. As the thickness of the film increases, it is more common to obtain uniform dense films.

Figure 8.9 also shows the Raman spectrum of the graphene film at 5 ml filtration volume. From the Raman spectrum, it should be noted the defective nature of the graphene film from the profound D band. The defective nature of the graphene film arises from the disordered carbon atoms from the edges of individual graphene islands.

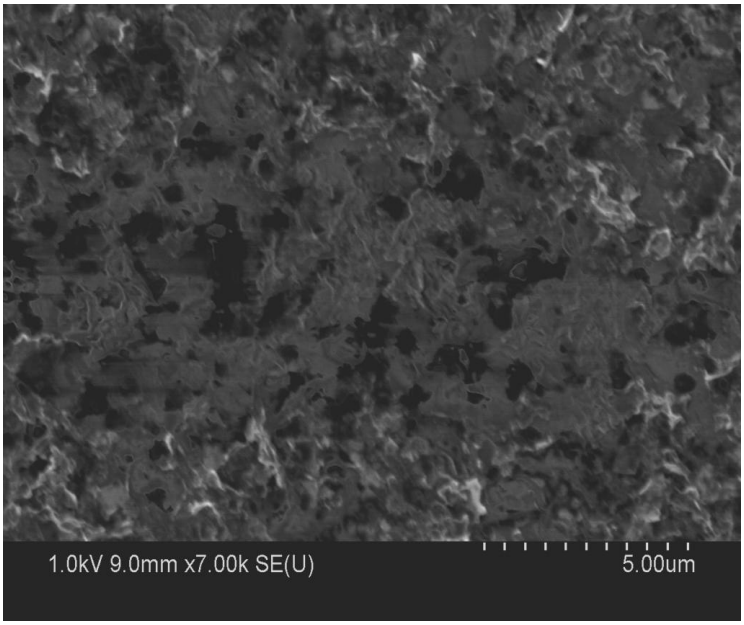

Figure 8.6: SEM picture showing the 3 ml filtration volume graphene film.

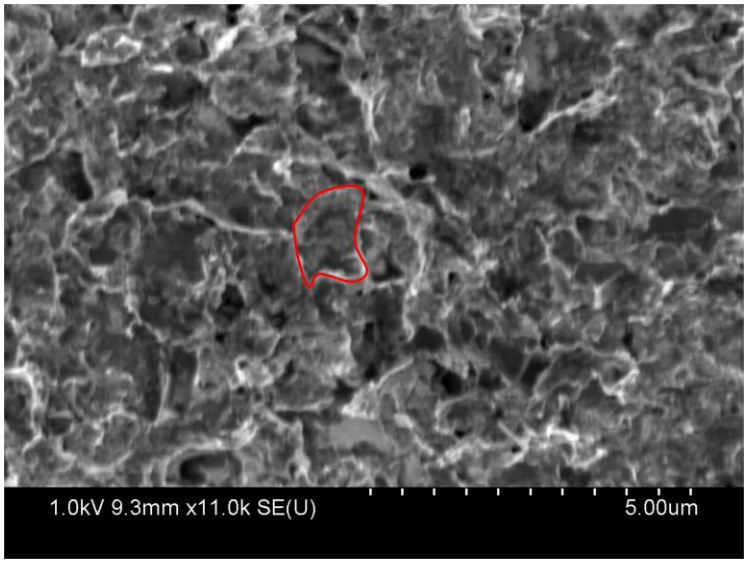

Figure 8.7: SEM picture showing the 5 ml filtration volume graphene film.

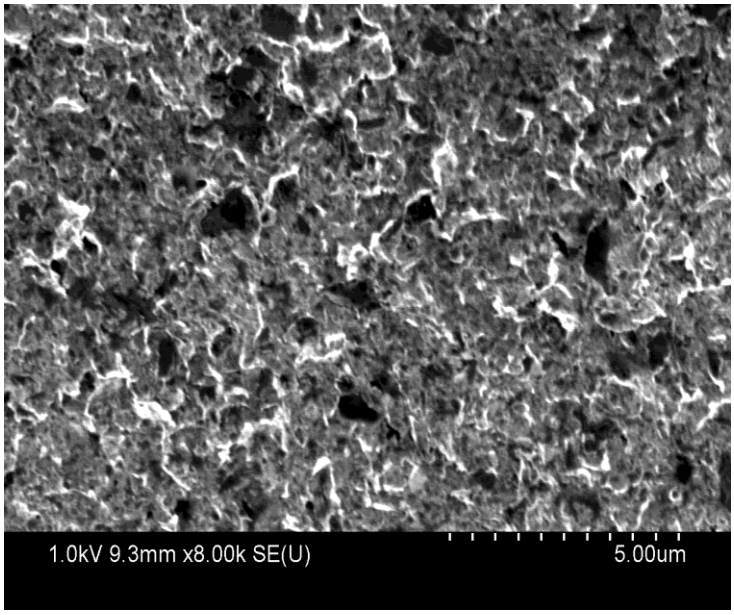

Figure 8.8: SEM picture showing the 10 ml filtration volume graphene film.

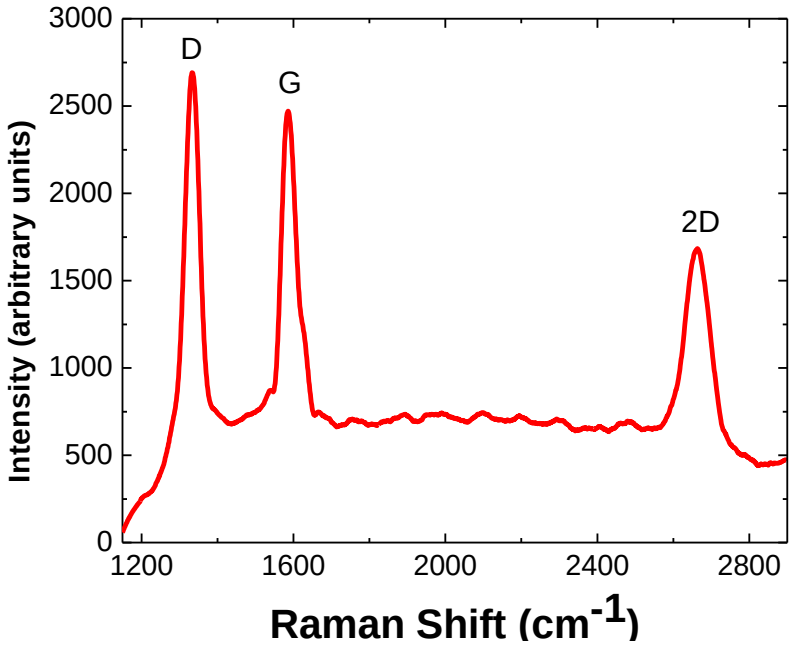

Figure 8.9: Raman spectrum of the 5 ml filtration volume graphene film.

8.6 Conductance of Various Graphene Films

We are interested to characterize the nature of the graphene film by preparing different graphene films at various filtration volumes to see if there's any noticeable trend. Figure 8.10 shows the conductance of the graphene film at different filtration volume. The trend is noticeable in which conductance increases as graphene concentration increases but at 6 ml and after, the line flattens. There is a 6 order of magnitude differences ranging from 10^{-8} to 10^{-2} S between the thinnest and thickest films. This is not surprising as electron transport at thinnest graphene film is through 2D electron hopping and as the thickness increases, electron transport is mainly through conductive paths.

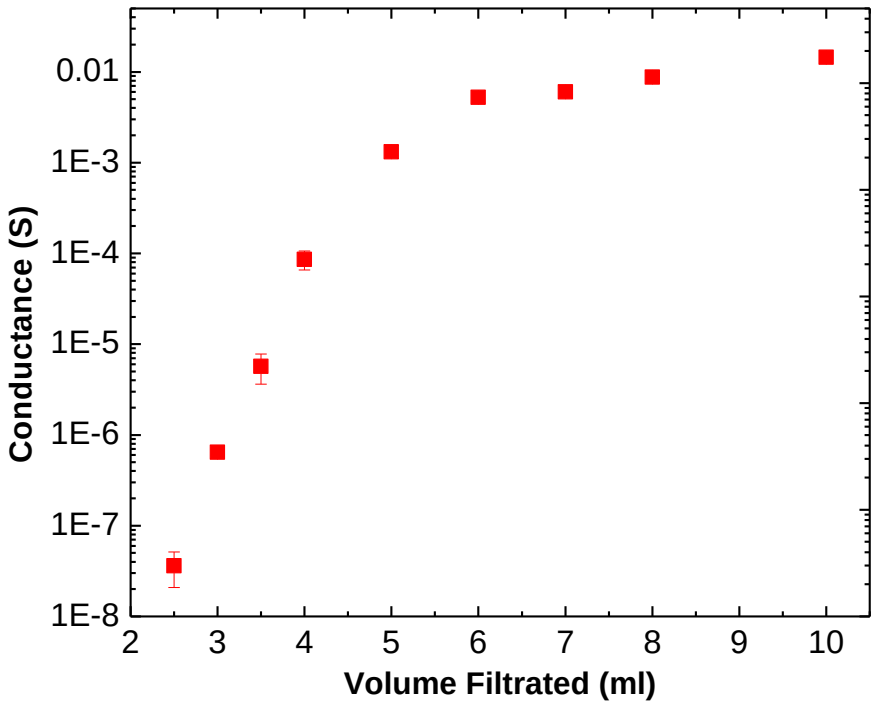

Figure 8.10: Shows the conductance (S) vs. volume filtrated (ml) for randomly stacked graphene sensors.

8.7 Characterization of Sensing Responses on Randomly Stacked Oxide-Free Graphene Gas Sensors

Experiments were done to analyze the sensing responses of the graphene sensors at different concentrations to a 100 millisecond pulse of toluene (an electron donor) and of 1,2-dichlorobenzene (an electron acceptor). In each case, we chose the number of molecules in the pulse to be similar to the number of molecules produced by our preconcentrator with sampling air containing 300 ppb of analyte. Figure 8.11 shows the real responses on sensitivity (%) of graphene sensors to toluene at various graphene filtration volumes (from 3 ml to 10 ml). Notice

the sensitivity decreases with increasing graphene loadings. At 3 ml loading, the sensor sensitivity is highest at roughly 14% and lowest at 10 ml loading with roughly 1.5%. The sensor sensitivity is defined as Sensitivity (%) = $(R-R_0) / R_0$, where R_0 is the initial resistance of the sensor at background carrier ultrahigh purity helium gas and R is the resistance value after exposure to the target gas molecules. It is interesting to note the resistance increases after exposure to toluene gas molecules (a typical electron donating molecule). This is unusual as graphene is normally known as a P-type semiconductor[15, 27, 28] due to water doping in the ambient environment. However, our graphene here is a N-type semiconductor due to the processing conditions as our graphene films undergo thermal treatment in the presence of nitrogen gas.[41] It is therefore possible for our graphene films being N-doped by the nitrogen gas which then exhibit the N-type characteristic behavior.

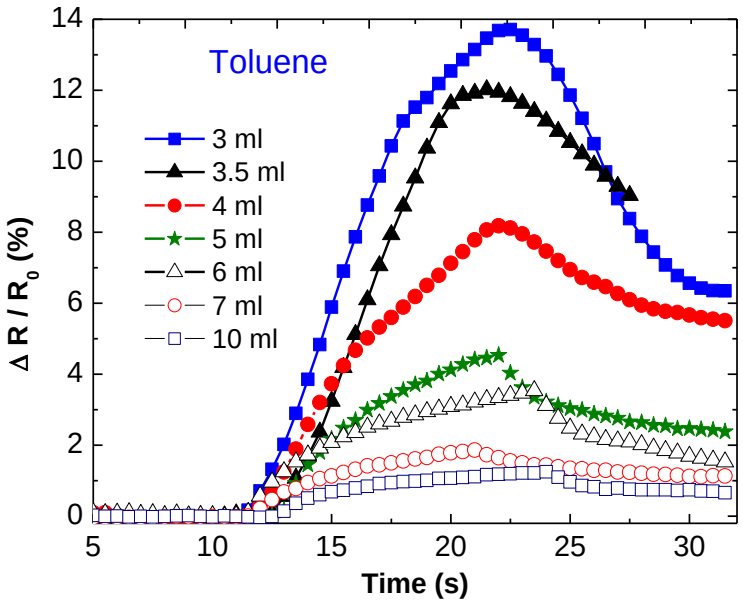

Figure 8.11: Shows the sensitivity response (%) of randomly stacked graphene sensors vs. various graphene filtration volumes (ml) to 100 millisecond pulse of 10^{14} toluene molecules.

8.8 Comparisons of Sensing Responses to Other Carbon Based Gas Sensors

Figure 8.12 compares the sensing responses with toluene from randomly stacked oxide free graphene sensors to polycrystalline graphene, highly defective CNT, and polycrystalline ribbon grpahene sensors under the same experimental conditions. For polycrystalline graphene, the maximum response is at 2.5% which corresponds to graphene filtration volume above 7 ml. For highly defective CNT sensors, the maximum response is at 4.2% which is about the response from 6 ml filtration volume. Polycrystalline ribbon graphene sensors has 5.5% maximum response which corresponds to 5 ml graphene filtration volume. At below 4 ml graphene filtration volume, the randomly stacked oxide free graphene sensors show superior sensing as compared to other types.

Figure 8.13 compares the sensing responses with 1,2-dichlorobenzene from randomly stacked oxide free graphene sensors to polycrystalline graphene, highly defective CNT, and polycrystalline ribbon graphene sensors under the same experimental conditions. At below 3.5 ml graphene filtration volume, the randomly stacked oxide free graphene sensors show similar sensing as polycrystalline ribbon graphene sensors. For polycrystalline graphene, the maximum response is at 6% which corresponds to graphene filtration volume at 4 ml. For highly defective CNT sensors, the maximum response is at 3.5% which is about the response from 5ml to 10 ml filtration volume.

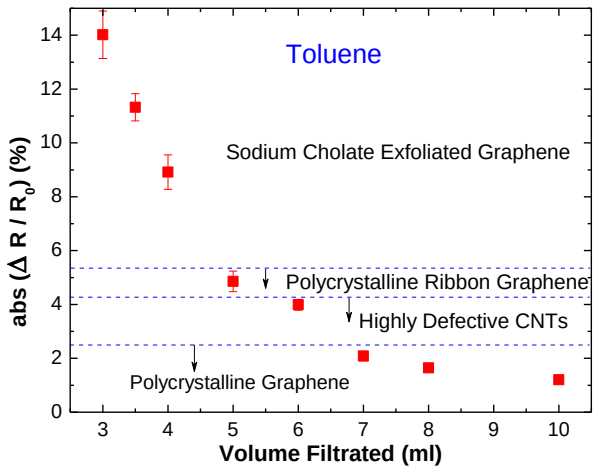

Figure 8.12: Shows the sensitivity response (%) of randomly stacked graphene sensors vs. various graphene filtration volumes (ml) to 100 millisecond pulse of 10^{14} toluene molecules. The dashed lines represent maximum responses from polycrystalline graphene, highly defective CNTs, and polycrystalline ribbon graphene (respectively) with same dosage of toluene (from previously published paper).

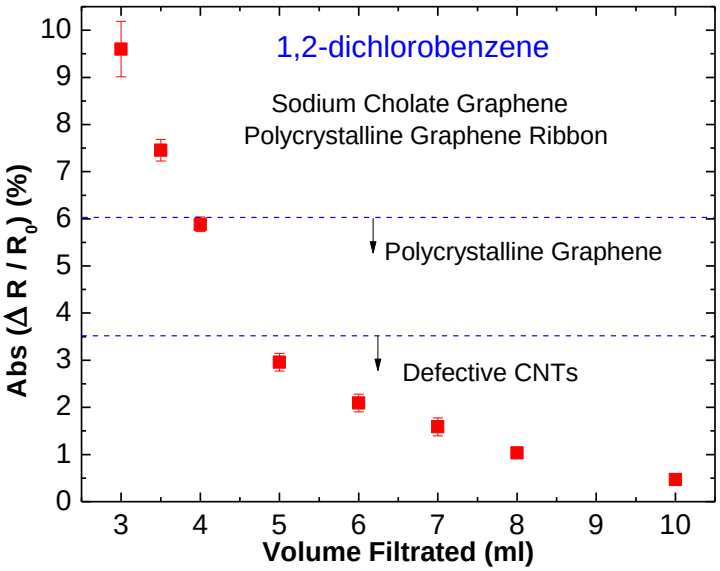

Figure 8.13: Shows the sensitivity response (%) of randomly stacked graphene sensors vs. various graphene filtration volumes to 100 millisecond pulse of 10^{15} 1,2-dichlorobenzene molecules. The dashed lines represent maximum responses from highly defective CNTs, polycrystalline graphene, and polycrystalline ribbon graphene (respectively) with same dosage of toluene (from previously published paper).

8.9 Effect of Applied Voltages on Graphene Gas Sensors

Figure 8.14 shows the sensing response towards toluene at 2 different graphene filtration volumes of 3 ml and 5 ml. Notice that at low applied voltages, there is no measurable change in the resistance of graphene sensor when it is exposed to pulses of toluene. However, a large response is seen once the voltage exceeds a critical level. Evidently, the applied electric field makes an unexpectedly large change in the sensitivity of the graphene sensors. For 3 ml graphene filtration volume, the sensor has maximum response at 1V as compared to 5 ml

filtration volume where the maximum occurs at 0.025V. Applying higher electric field would only decrease the sensor responses once it reaches the maximum value.

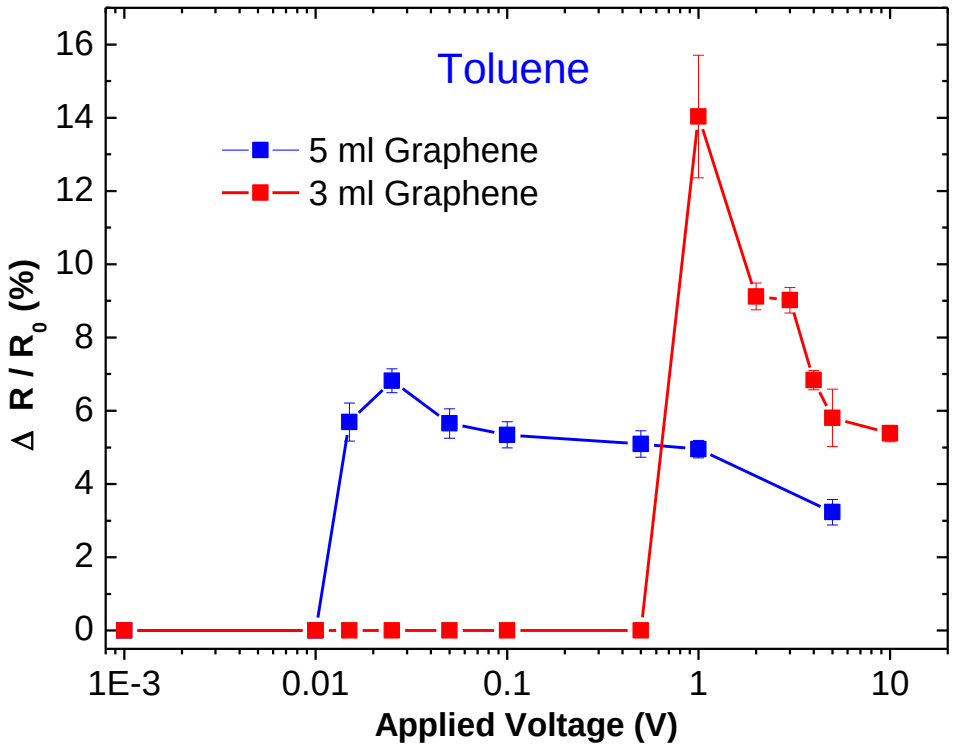

Figure 8.14: Applied voltage (V) vs. sensor sensitivity (%) for two graphene filtration volumes (3 ml, 5 ml) to 100 millisecond pulse of 10^{14} toluene molecules. There are no detectable responses at low voltage but turns on when the applied voltage exceeds critical values respectively.

8.10 Mott's Variable Range Hopping Model

We performed an additional experiment to verify the electron hopping regime in our sensors. The experiment was to measure resistance of randomly stacked oxide free graphene

sensors versus temperature in the range of 100-300 K, and use Mott's variable range hopping (VRH) model to explain the order of hopping in our graphene sensors. Figure 8.15 shows the temperature-dependent resistance of the sensor fitted to the following Mott's VRH model:

$$R(T) = R_0 \exp\left[-\left(T_0/T\right)^n\right]$$

Where R_0 is a constant, T_0 is the characteristic temperature and n is the (dimensionality + 1) of hopping in Mott's variable range hopping (VRH) model. The plot of Ln R vesus $T^{-1/3}$ for our sensors show a linear fitting as shown in the inset of Figure 8.15. This indicates that the electronic transport within the oxide free randomly stacked graphene film is determined by the two-dimensional electron hopping mechanism at 5 ml filtration volume.

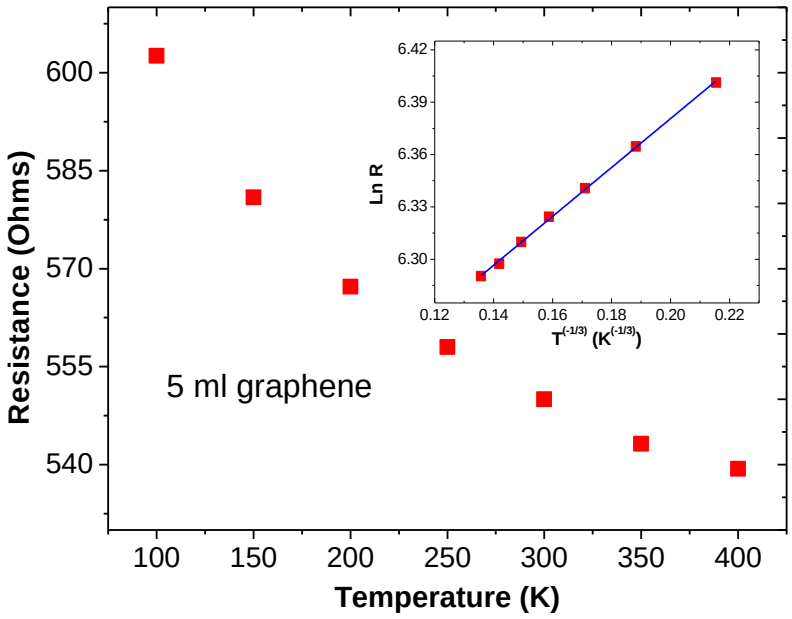

Figure 8.15: Temperature dependence on the 5 ml filtration volume graphene sensor with resistance (ohms) at different temperatures from 100-400 K. The inset shows the linear fitting of Ln R to $T^{-1/3}$ according to the Mott's VRH 2-D model.

8.11 Temperature Dependency on Resistance of Graphene Sensors

Figure 8.16 shows the temperature dependence resistance of graphene sensors versus temperatures (100-300K) at different filtration volumes. The resistance values were normalized against room temperature reading at 300K. At low temperatures (below 300K), electron hopping can be seen with 3 ml and 5 ml graphene filtration volumes. At 7 ml, minimal electron hopping occurs and the trend starts to change at 8 ml. Finally at 10 ml, differently from the semiconductor like behavior in the below 7 ml cases, the resistance of the graphene film increases monotonically with temperature thus confirming the metal like behavior. It has not been previously reported for graphene films for such broad temperature linear spanning range. Potential application such as nanothermometers can utilize such linear trend across this temperature range for our randomly stacked oxide free graphene film at 10 ml filtration volume.

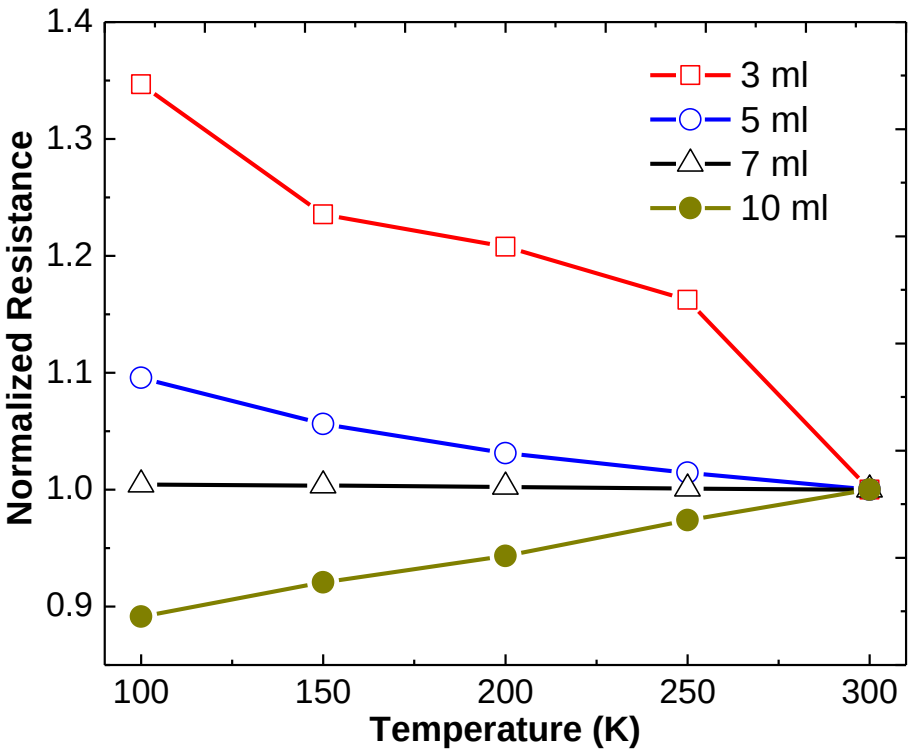

Figure 8.16: Shows the temperature dependence on different graphene sensor loadings with resistance (ohms) at different temperatures from 100-300 K.

8.12 Effect of 2D Electronic Hopping Mechanism on Graphene Gas Sensor Responses

We speculate surfactant sodium cholate assisted exfoliated graphene produces mono layer of islands of inner core well-ordered carbon atoms with metallic like conduction surrounded by outer regions of disordered carbon atoms on the edges of the islands. As the graphene film thickness increases (filtration volume increases), there is a shift in conduction from 2D electron hopping through thicker barriers at thin film (3 ml filtration volume) to fluctuation assisted tunneling through thin barriers at thick film (10 ml filtration volume). The

thicker barriers corresponds to the disordered carbon atoms at the outer regions of the graphene island where the thin barriers corresponds to well ordered carbon atoms at the inner core of the island. Due to greater thickness of the barrier disordered regions at thin graphene film (3 ml filtration volume), the increase in conductance was observed as the temperature increases. Essentially, there are more disordered regions of the graphene islands being exposed on the surface at low filtration volume. At thicker graphene film (10 ml filtration volume), there are more overlapping between individual graphene islands thus minimizing the amount of disordered regions which makes the barrier thinner thus decrease in conductance was observed as the temperature increases. Therefore it is not surprising to see the superior sensitivity observed from thinner graphene film (3 ml filtration volume) compared to polycrystalline graphene/ribbons and defective CNTs sensors as 2D electron hopping dominates. Whereas as the film thickness increases (filtration volume increases), the sensitivity drops as the conduction mechanism shifts from 2D VRH to metal-like conduction mechanism.

8.13 Conclusion

In summary, simple chemiresistor based gas sensors with randomly stacked oxide free graphene film were fabricated using surfactant assisted exfoliation of graphite and tested for target gas molecule sensitivity. Vacuum filtration is used to produce various thickness of graphene films at different filtration volumes. Stamp printing technique was used to deposit graphene film on top of electrode gap in order to avoid polymer resist contaminates on the sensor. At low filtration volumes, oxide free randomly stacked graphene film sensors showed better sensitivity towards target molecules compared to polycrystalline/ribbon graphene and

defective CNT gas sensors. As the graphene film thickness increases, there is a shift in conduction mechanism from 2D electron hopping to metallic like conduction which explains the drop in sensitivity as the filtration volume increases.

8.14 References

1. Abergel, D. S. L.; Apalkov, V.; Berashevich, J.; Ziegler, K.; Chakraborty, T., Properties of Graphene: A Theoretical Perspective. *Adv. Phys.* **2010,** *59* (4), 261-482.

2. Allen, M. J.; Tung, V. C.; Kaner, R. B., Honeycomb Carbon: A Review of Graphene. *Chem. Rev. (Washington, DC, U. S.)* **2010,** *110* (1), 132-145.

3. Bolotin, K. I.; Sikes, K. J.; Jiang, Z.; Klima, M.; Fudenberg, G.; Hone, J.; Kim, P.; Stormer, H. L., Ultrahigh Electron Mobility in Suspended Graphene. *Solid State Communications* **2008,** *146* (9-10), 351-355.

4. Das, S. S.; Adam, S.; Hwang, E. H.; Rossi, E., Electronic Transport in Two Dimensional Graphene. *arXiv.org, e-Print Arch., Condens. Matter* **2010**, 1-85, arXiv:1003.4731v1 [cond-mat.mes-hall].

5. Geim, A. K.; Novoselov, K. S., The Rise of Graphene. *Nature Materials* **2007,** *6* (3), 183-191.

6. Mucciolo, E. R.; Lewenkopf, C. H., Disorder and Electronic Transport in Graphene. *J. Phys.: Condens. Matter* **2010,** *22* (27), 273201/1-273201/12.

7. Novoselov, K. S.; Geim, A. K.; Morozov, S. V.; Jiang, D.; Katsnelson, M. I.; Grigorieva, I. V.; Dubonos, S. V.; Firsov, A. A., Two-Dimensional Gas of Massless Dirac Fermions in Graphene. *Nature* **2005,** *438* (7065), 197-200.

8. Novoselov, K. S.; McCann, E.; Morozov, S. V.; Fal'ko, V. I.; Katsnelson, M. I.; Zeitler, U.; Jiang, D.; Schedin, F.; Geim, A. K., Unconventional Quantum Hall Effect and Berry's Phase of 2ï€ in Bilayer Graphene. *Nature Physics* **2006,** *2* (3), 177-180.

9. Rao, C. N. R.; Sood, A. K.; Subrahmanyam, K. S.; Govindaraj, A., Graphene: The New Two-Dimensional Nanomaterial. *Angew. Chem., Int. Ed.* **2009,** *48* (42), 7752-7777.

10. Rao, C. N. R.; Sood, A. K.; Voggu, R.; Subrahmanyam, K. S., Some Novel Attributes of Graphene. *J. Phys. Chem. Lett.* **2010,** *1* (2), 572-580.

11. Soldano, C.; Mahmood, A.; Dujardin, E., Production, Properties and Potential of Graphene. *Carbon* **2010,** *48* (8), 2127-2150.

12. Stander, N.; Huard, B.; Goldhaber-Gordon, D., Evidence for Klein Tunneling in Graphene P-N Junctions. *Physical Review Letters* **2009,** *102* (2).

13. Wakabayashi, K.; Takane, Y.; Yamamoto, M.; Sigrist, M., Electronic Transport Properties of Graphene Nanoribbons. *New J. Phys.* **2009,** *11* (Sept.), 095016.

14. Young, A. F.; Kim, P., Quantum Interference and Klein Tunnelling in Graphene Heterojunctions. *Nature Physics* **2009,** *5* (3), 222-226.

15. Schedin, F.; Geim, A. K.; Morozov, S. V.; Hill, E. W.; Blake, P.; Katsnelson, M. I.; Novoselov, K. S., Detection of Individual Gas Molecules Adsorbed on Graphene. *Nature Materials* **2007,** *6* (9), 652-655.

16. Robinson, J. T.; Perkins, F. K.; Snow, E. S.; Wei, Z.; Sheehan, P. E., Reduced Graphene Oxide Molecular Sensors. *Nano Letters* **2008,** *8* (10), 3137-3140.

17. Capone, S.; Forleo, A.; Francioso, L.; Rella, R.; Siciliano, P.; Spadavecchia, J.; Presicce, D. S.; Taurino, A. M., Solid State Gas Sensors: State of the Art and Future Activities. *Journal of Optoelectronics and Advanced Materials* **2003,** *5* (5), 1335-1348.

18. Kong, J.; Franklin, N. R.; Zhou, C.; Chapline, M. G.; Peng, S.; Cho, K.; Dai, H., Nanotube Molecular Wires as Chemical Sensors. *Science* **2000,** *287* (5453), 622-625.

19. Moseley, P. T., Solid State Gas Sensors. *Measurement Science and Technology* **1997,** *8* (3), 223-237.

20. Zettl, A., Extreme Oxygen Sensitivity of Electronic Properties of Carbon Nanotubes. *Science* **2000,** *287* (5459), 1801-1804.

21. Novoselov, K. S.; Geim, A. K.; Morozov, S. V.; Jiang, D.; Zhang, Y.; Dubonos, S. V.; Grigorieva, I. V.; Firsov, A. A., Electric Field in Atomically Thin Carbon Films. *Science* **2004,** *306* (5696), 666-669.

22. de Heer, W. A.; Berger, C.; Wu, X.; First, P. N.; Conrad, E. H.; Li, X.; Li, T.; Sprinkle, M.; Hass, J.; Sadowski, M. L.; Potemski, M.; Martinez, G., Epitaxial Graphene. *Solid State Communications* **2007,** *143* (1-2), 92-100.

23. Seyller, T.; Bostwick, A.; Emtsev, K. V.; Horn, K.; Ley, L.; McChesney, J. L.; Ohta, T.; Riley, J. D.; Rotenberg, E.; Speck, F., Epitaxial Graphene: A New Material. *Physica Status Solidi (B) Basic Research* **2008,** *245* (7), 1436-1446.

24. Li, X.; Cai, W.; An, J.; Kim, S.; Nah, J.; Yang, D.; Piner, R.; Velamakanni, A.; Jung, I.; Tutuc, E.; Banerjee, S. K.; Colombo, L.; Ruoff, R. S., Large-Area Synthesis of High-Quality and Uniform Graphene Films on Copper Foils. *Science* **2009,** *324* (5932), 1312-1314.

25. Kim, K. S.; Zhao, Y.; Jang, H.; Lee, S. Y.; Kim, J. M.; Ahn, J. H.; Kim, P.; Choi, J. Y.; Hong, B. H., Large-Scale Pattern Growth of Graphene Films for Stretchable Transparent Electrodes. *Nature* **2009,** *457* (7230), 706-710.

26. Dua, V.; Surwade, S. P.; Ammu, S.; Agnihotra, S. R.; Jain, S.; Roberts, K. E.; Park, S.; Ruoff, R. S.; Manohar, S. K., All-Organic Vapor Sensor Using Inkjet-Printed Reduced Graphene Oxide. *Angewandte Chemie - International Edition* **2010,** *49* (12), 2154-2157.

27. Fowler, J. D.; Allen, M. J.; Tung, V. C.; Yang, Y.; Kaner, R. B.; Weiller, B. H., Practical Chemical Sensors from Chemically Derived Graphene. *ACS Nano* **2009,** *3* (2), 301-306.

28. Lu, G.; Ocola, L. E.; Chen, J., Gas Detection Using Low-Temperature Reduced Graphene Oxide Sheets. *Applied Physics Letters* **2009,** *94* (8).

29. Gómez-Navarro, C.; Weitz, R. T.; Bittner, A. M.; Scolari, M.; Mews, A.; Burghard, M.; Kern, K., Electronic Transport Properties of Individual Chemically Reduced Graphene Oxide Sheets. *Nano Letters* **2007,** *7* (11), 3499-3503.

30. Yang, D.; Velamakanni, A.; Bozoklu, G.; Park, S.; Stoller, M.; Piner, R. D.; Stankovich, S.; Jung, I.; Field, D. A.; Ventrice Jr, C. A.; Ruoff, R. S., Chemical Analysis of Graphene Oxide Films after Heat and Chemical Treatments by X-Ray Photoelectron and Micro-Raman Spectroscopy. *Carbon* **2009,** *47* (1), 145-152.

31. Dan, Y.; Lu, Y.; Kybert, N. J.; Luo, Z.; Johnson, A. T. C., Intrinsic Response of Graphene Vapor Sensors. *Nano Letters* **2009,** *9* (4), 1472-1475.

32. Pearce, R.; Iakimov, T.; Andersson, M.; Hultman, L.; Spetz, A. L.; Yakimova, R., Epitaxially Grown Graphene Based Gas Sensors for Ultra Sensitive No2 Detection. *Sensors and Actuators, B: Chemical* **2011**.

33. Joshi, R. K.; Gomez, H.; Alvi, F.; Kumar, A., Graphene Films and Ribbons for Sensing of O2, and 100 Ppm of Co and No2 in Practical Conditions. *Journal of Physical Chemistry C* **2010,** *114* (14), 6610-6613.

34. De, S.; King, P. J.; Lotya, M.; O'Neill, A.; Doherty, E. M.; Hernandez, Y.; Duesberg, G. S.; Coleman, J. N., Flexible, Transparent, Conducting Films of Randomly Stacked Graphene from Surfactant-Stabilized, Oxide-Free Graphene Dispersions. *Small* **2010,** *6* (3), 458-464.

35. Lotya, M.; Hernandez, Y.; King, P. J.; Smith, R. J.; Nicolosi, V.; Karlsson, L. S.; Blighe, F. M.; De, S.; Zhiming, W.; McGovern, I. T.; Duesberg, G. S.; Coleman, J. N., Liquid Phase Production of Graphene by Exfoliation of Graphite in Surfactant/Water Solutions. *Journal of the American Chemical Society* **2009,** *131* (10), 3611-3620.

36. Bourlinos, A. B.; Georgakilas, V.; Zboril, R.; Sterioti, T. A.; Stubos, A. K., Liquid-Phase Exfoliation of Graphite Towards Solubilized Graphenes. *Small* **2009,** *5* (16), 1841-1845.

37. Eda, G.; Fanchini, G.; Chhowalla, M., Large-Area Ultrathin Films of Reduced Graphene Oxide as a Transparent and Flexible Electronic Material. *Nature Nanotechnology* **2008,** *3* (5), 270-274.

38. Eda, G.; Lin, Y. Y.; Miller, S.; Chen, C. W.; Su, W. F.; Chhowalla, M., Transparent and Conducting Electrodes for Organic Electronics from Reduced Graphene Oxide. *Applied Physics Letters* **2008,** *92* (23).

39. Salehi-Khojin, A.; Lin, K. Y.; Field, C. R.; Masel, R. I., Nonthermal Current-Stimulated Desorption of Gases from Carbon Nanotubes. *Science* **2010,** *329* (5997), 1327-1330.

40. Salehi-Khojin, A.; Khalili-Araghi, F.; Kuroda, M. A.; Lin, K. Y.; Leburton, J. P.; Masel, R. I., On the Sensing Mechanism in Carbon Nanotube Chemiresistors. *ACS Nano* **2010,** *5* (1), 153-158.

41. Czerw, R.; Terrones, M.; Charlier, J. C.; Blase, X.; Foley, B.; Kamalakaran, R.; Grobert, N.; Terrones, H.; Tekleab, D.; Ajayan, P. M.; Blau, W.; Rühle, M.; Carroll, D. L., Identification of Electron Donor States in N-Doped Carbon Nanotubes. *Nano Letters* **2001,** *1* (9), 457-460.

Appendix A: Fabrication Recipe for Manufacturing Silicon Devices

Thermal Oxidation

1. Single side polished (SSP) 100 mm silicon wafer (Silicon Quest, 500 micron thick, <100> orientation, 1-5 ohm-cm nominal resistivity).
2. Buffered oxide etchant (BOE) for 1 min. Rinse with DI water and dry with N_2.
3. Load the wafer in the oxidation furnace tube at 400C with 2.5 L/min N_2 (6-stack multi-zone tube-furnace system, MNMS).
4. Set furnace temperature at 1100C.
5. Set O_2 flow at 6 L/min and turn off N_2 flow when temperature is at 1100C.
6. Dry oxidation in furnace for 13 hours to get 500 nm of oxide on the wafer.
7. Turn on N_2 flow at 2.5 L/min and turn off O_2 flow. Set temperature at 400C.
8. Unload the wafer when the temperature gets below 600C.

Create gold contacts

9. Degrease the wafer (acetone, IPA, DI, IPA, N_2 dry).
10. Bake out wafer on hotplate at 150C for 2 min.
11. Spin coat AP 8000 adhesion promoter (recipe #3, 3000 rpm, 30 sec).
12. Spin coat pore side of wafer with PR1518 (recipe#3, 3000 rpm, 30 sec).
13. Soft bake on Al ring 3 minutes 110C with heat shield.
14. Expose mask #1 (8 sec exposure) using aligner preset#3 (Electron Visions (EVG) double-sided aligner, MNMS).

15. Develop in AZ400K developer (4:1 DI: developer, 100 ml DI) about 120 sec.

16. DI quench then rinse with low pressure DI, N_2 dry.

17. Check with microscope for developing result.

18. Hard bake 120 sec at 110C.

19. O_2 descum in Jupiter RIE at 250W for 30 sec (3:1 O_2: Ar).

20. Sputter Cr for 10 nm at 300 W (AJA 8-gun DC metal sputtering system, MNMS).

21. Sputter Au for 100nm at 300 W.

22. Liftoff in 1165 PR stripper in ultrasound for at least 15 min then DI rinse, then transfer.

23. Acetone bath in ultrasound for 2 min, IPA bath in ultrasound for 2 min, N_2 dry.

24. Check with microscope and make sure there are no remaining particles.

Protecting the patterns

25. Spin coat AZ4620 recipe #3 (3000 RPM, 30 sec).

26. Hard bake at 110C for 2 min and ramp to 160C for 20 mins.

Laser shop dicing

27. Have wafer scored but not cut along the alignment marks in between sensors.

APTES coating

28. Strip PR in 400T stripper at 120C for 30 min.

29. DI water rinse

30. SC-1 clean at 72C for 5 mins. (200 ml DI, 20 ml H_2O_2, 2 ml NH_4OH)

31. DI water rinse, IPA rinse, N_2 dry.

32. Clean the container with acetone to ensure no residual water in it.

33. APTES solution 1% for 20 mins (80 ml acetone, 0.8 ml APTES).

34. Rinse the wafer with acetone.

35. IPA rinse and N_2 dry.

36. Cure wafer at 120C for 20 min.

Appendix B: Sodium Cholate Surfactant Exfoliation of Graphite into Graphene

1. Purchase graphite flakes (+100 mesh, >75% min, 2.5 kg, Sigma-Aldrich).
2. Weigh 0.5 g of sodium cholate (BioXtra, >99%, Sigma-Aldrich) into the Erlenmeyer flask.
3. Using a graduated cylinder, add 100 ml DI water into the Erlenmeyer flask. Stir until sodium cholate is completely dissolved.
4. Weigh 1.5 g of graphite flakes. Add into the 0.5% sodium cholate/water solution.
5. Sonicate solution for 60 minutes with 100 W sonicator (ultrasound probe) at 100% power.
6. Allow solution to cool and transfer to centrifuge tubes and centrifuge for 90 minutes at 500 RPM.
7. Slowly and carefully decant top 80% of centrifuge tubes into 20 ml scintillation vials. Solution should have no noticeable particles.

Appendix C: Randomly Stacked Oxide-Free Graphene Film Formation

1. Obtain a 47 mm Mixed Cellulose Ester (MCE) membrane with 0.22 micron pore size (Millipore, Fischer Scientific GST04700).
2. Wet the Vacuum filtration setup with DI water before placing the MCE membrane on the setup.
3. Apply house vacuum and add 10 ml of DI water to the vacuum filtration setup. This will charge the membrane. Allow all 10 ml water to filter through the membrane.
4. Shut off the house vacuum.
5. Carefully and slowly pour the desired volume of graphene solution into the vacuum filtration setup. Be extra careful to not form bubbles as this will disrupt the film.
6. Cover the top of vacuum filtration setup with Parafilm.
7. Once all graphene solution has passed through the membrane. Open the house vacuum.
8. Allow the membrane to sit under house vacuum for at least 1 hour.
9. Slowly pour 80 ml of DI water into the vacuum filtration setup to get rid of sodium cholate surfactant.
10. Allow all water to pass through and let it sit under house vacuum for 10 minutes to partially dry the membrane.
11. Remove the membrane from the vacuum filtration setup and placed it in a covered dish.
12. Allow the membrane to completely dry overnight.

Appendix D: Deposition of Randomly Stacked Oxide-Free Graphene Film on Silicon Devices

1. Rinse the silicon device with acetone, methanol, IPA, water and IPA. Place on 110C hot plate for 2 minutes to bake out the solvents.
2. Add 2 microliter of DI water to the center of the silicon device over the gap between the electrodes.
3. Using a 1.5 mm hole punch to punch out a small disk of the MCE-graphene membrane.
4. Place the disk upside down so graphene film is facing the silicon device onto the water drop of the device.
5. Use a filter paper and soak up the excess water so the MCE-graphene disk appears to lay flat on the silicon device.
6. Briefly press the filter paper onto the MCE-graphene disk.
7. Fill a 5 ml Erlenmeyer flask with 4 ml of acetone and boiling chips.
8. Place the acetone filled flask onto a hot plate with heat setting at 4.5.
9. Bring the acetone to a boil.
10. Place the silicon device in the PEEK carrier upside down with MCE-graphene disk facing the flask.
11. Expose the silicon device to the acetone vapor until all liquid acetone has vaporized.
12. Remove the silicon device from the flask and place in acetone bath for 1 hour.
13. Remove from acetone bath and rinse with acetone, methanol, IPA, DI water, IPA, and N_2 dry.
14. Solder the silicon device to finalize graphene based gas sensor.

Appendix E: Standard Fabrication Procedure

E.1 Sputtering Procedure

LL = Loadlock, SC = Sputtering Chamber, RDC = Radial Distribution Chamber

Initial Checks:
1. Make sure CryroHiVac for RDC and SC are on.
2. SC ion gauge < 10^{-7} Torr.
3. RDC ion gauge < 10^{-7} Torr.
4. Turn off ion gauge.
5. Turn on DRYVAC roughing pump on vacuum control panel.

Loading Sample into Loadlock:
1. Unscrew LL door.
2. Make sure LL gate valve to RDC is closed.
3. Make sure LL roughing valve is closed.
4. Open LL vent valve.
5. Wait for LL door to open (several minutes).
6. Close LL vent valve.
7. Load sample puck into LL and close door.
8. Open LL roughing valve.
9. Close LL roughing valve when TC 1 reaches 4 x 10^{-2} Torr.
10. Slowly open LL gate valve until fully open.

Transferring Sample into Sputtering Chamber:

1. Check that fork is in the correct position to retrieve the sample puck.
2. Drive the fork into the LL adjusting the height to be below the puck rim.
3. Capture puck.
4. Raise fork to upper red line on manipulator.
5. Retract fork into RDC, until it stops.
6. Close RDC gate valve.
7. Lower fork until it clears alignment stops.
8. Rotate fork counter clockwise from top to the SC alignment stops.
9. Raise fork to the lower red line on manipulator.
10. Open SC gate valve.
11. Check that the sample stage in “open” to receive the sample puck.
12. Slowly drive the fork onto stage, watching alignment.
13. Lower sample puck onto stage until the fork releases from the rim.
14. Slowly retract the fork watching for misalignment.

15. Close RDC gate valve.

Sputtering:
1. Verify that all shutters are closed.
2. Start sample rotation (speed = 4).
3. Open argon ¼ turn valve at the desired gun.
4. Turn on MFC channel 1 (flow rate should be at 20 sccm).
5. Activate conductance valve.
6. TC 3 = around 2.3 x 10 -3 Torr.
7. Open gun shutter of appropriate gun.
8. Set appropriate power level.
    Al 300 W ~ 40 Å /min
    Au 300 W ~ 490 Å /min
    Cr 300 W ~ 170 Å /min
    NiCr 400 W ~ 160 Å /min
9. Turn on DC power and presputter for 30 s to clean surface and stabilize gun power.
10. Open sample shutter to 300 ℃.
11. Begin timing deposition.
12. Close gun shutter.
13. Turn off gun power.
14. Turn of MFC.
15. Close gun shutter.
16. Stop sample rotation with “open” side toward manipulator fork.
17. Close ¼ turn Ar valve.
18. Turn off conductance valve.

Unloading Sample from Sputter Chamber:
1. Slowly open SC gate valve.
2. Slowly drive fork into SC watching for interference with sample stage.
3. Capture puck.
4. Raise fork to upper red line on manipulator.
5. Retract fork into RDC until it stops.
6. Close SC gate valve.
7. Lower fork to clear alignment stops.
8. Rotate fork counter clockwise from the top to the LL alignment stops.
9. Raise fork to red line of manipulator.
10. Make sure LL roughing valve and vent valve are closed.
11. Open LL gate valve.
12. Transfer puck to LL.
13. Lower puck onto LL stage.
14. Retract fork.
15. Close LL gate valve.

Removing Sample and Finishing:
1. Unscrew LL door.
2. Open LL vent valve.

3. Wait for LL door to open (several minutes).
4. Close LL vent valve.
5. Unload sample puck from LL and close door.
6. Open LL roughing valve.
7. Close LL roughing valve when TC 1 reaches 5 x 10 -2 Torr.
8. Turn off DRYVAC pump.

E.2 Photolithography

1. Prebake the wafer at 110 ℃ for 1 min.
2. PR spincoat deep etched side (choose recipe).
3. Softbake 60 ℃ (use ring on the hotplate) for 2 min.
4. Softbake 110 ℃ (use ring on the hotplate) for 2 min.
5. PR spincoat the opposite side (choose recipe)
6. Softbake 60 ℃ (use ring on the hotplate) for 3 min.
7. Softbake 110 ℃ (use ring on the hotplate) for 3 min.
8. Expose the first side.
9. Develop the alignment marks.
10. Exposure for the other side.
11. Develop (AZ 400K: DI water = 1:4) for 1-3 min.
12. Develop (AZ 400K: DI water = 1:10) for 1 min.
13. Overflow rinse in DI water for 1 min.
14. Nitrogen blow dry.
15. Softbake 60 ℃ (use ring on the hotplate) for 2 min.
16. Hardbake 110 ℃ ramped to 160 ℃, beginning timing from 150 ℃ for 15 min.

Spin Coating Procedure:

Caution:
Wafer must be centered on chuck. If wafer is not centered, wafer may fly off chuck and cause wafer damage as well as personal injury.

The nitrogen valve must be opened during spinner operation. Nitrogen is used to displace oxygen from the electronics area of the machine. The fumes given off during the process may be potentially explosive if combined with the right levels of oxygen. After spinner operation is complete, the nitrogen valve should be turned off to prevent nitrogen loss.

Photoresist should be handled under yellow safe light. If the photoresist or photoresist- coated wafer is exposed to sunlight or standard room lighting, damage to the photoresist will result.

Photoresist is sensitive to temperature and humidity levels. The large containers of photoresist stored in the gowning room refrigerator should not be opened until the photoresist reaches room temperature. Generally this takes 24 h to occur.

1. Turn the nitrogen valve on.

2. Turn the machine on at the power switch located on the back of the device. After approximately five seconds, the display will show the recipe currently selected.
3. The recipes that are currently in use are:

    Recipe #1
    2000 RPM 1 s-1 s
    5000 RPM 1 s-1 s
    5000 RPM 1 s-28 s

    Recipe #2
    1000 RPM 1 s-1 s
    1500 RPM 1 s-20 s
    3000 RPM 1 s-40 s

    Recipe #3
    1000 RPM 1 s-2 s
    2000 RPM 1 s –2 s
    3000 RPM 1 s-30 s
4. Remove the spinner cover and place an aluminum foil protective cover in the bowl of the spinner.
5. Attach the vacuum chuck to the spinner shaft. The shaft as well as the chuck has a flat spot so that the chuck can only be installed in one way.
6. Place the wafer on the vacuum chuck.
7. Center the wafer. Toggle the START/STOP switch on and off to make sure that the wafer is centered on the chuck. The spin coater will not start until a check for vacuum is performed. This should take a second or two. If the wafer is not centered on the chuck, an out of round condition will be created and the photoresist or other coating will not be evenly distributed. Several attempts may be needed to center the wafer.
8. Select the recipe as per the process sheet requirements. The desired recipe can be selected on the spin coater by depressing the CHANGE PRESET button. Next press ENTER and then the MINUS or PLUS button. This will allow you to scroll through the recipes. Once you have the desired recipe, press the ENTER button. Next press the MESSAGE button and this will return you to the screen where recipe number, rpm, and time is displayed. New recipes can also be generated by depressing the CHANGE PRESET button. Only experienced lab staff should make changes to the recipes.
9. Disperse several drops (2 to 3 droppers) of photoresist or other coating in the center of the wafer.
10. Press the START button. As the wafer turns, the photoresist or other coating will be distributed across the surface of the wafer. If the amount of photoresist is not adequate, feathering of the photoresist will occur. The wafer will not be completely covered. The spin rate as well as remaining time will be indicated on the display screen. The process can be stopped at any time by pressing the STOP button. Often when the wafer is spinning a cotton candy like substance will appear at the bowl periphery. To avoid wafer contamination, this substance should be removed with an alpha wipe as the spinning process is being performed.
11. Remove the wafer when the spin coater automatically stops.
12. If the spin coating process did not work out as desired, the photoresist can be removed with an acetone rinse and the process repeated again.

13. Shut down the spin coater, remove the vacuum chuck and aluminum foil protective bowl cover.
14. Turn off the power switch
15. Replace the bowl cover.
16. Turn off the nitrogen valve.

E.3 Aligner Operation Procedure

Cautions:
During the exposure process the ultraviolet lamp house will move forward. Care must be taken not to use the area in front of the lamp house for storage.

Exposure of the eyes and skin to ultraviolet light should be avoided. Exposure to ultraviolet light can cause burning of the eyes and skin.

If there is a failure of the ultraviolet lamp pressure boundary due to explosion or other causes, warn others and leave the room immediately. Mercury vapor is extremely dangerous to health.

1. Turn on the MAIN switch that is located on the control panel.
2. Turn the UV light power switch to on.
3. Depress the UV light START switch. The ultraviolet light will come on. The machine will increase the power of the ultraviolet light when an exposure is made.
4. Turn on the POWER ON key switch. The POWER ON Key switch should not be turned on until the UV light power supply is energized.
5. Turn on the computer processing unit.
6. Set the micrometers to RED 5 for standard position. If you don't, there is a pretty good chance that you will get a low vacuum message later on during aligner operation. The unit is now ready for operation. Instructions for the use of the machine will be displayed in the EV420 LCD display.

Top Side Alignment:

If at any time you want to stop the process, press the RESET key and you will be taken back to the initial step by following commands on the LCD DISPLAY. Follow all steps which are displayed and masked by < >.

1. Move <TRAY OUT> to continue.
2. Verify that you are in the topside alignment routine by pressing the MENU key. Select the CHANGE, SIDE, and TOP commands. Then press F4 twice to go back and continue in the procedure.
3. Select the Preset by use of the direction keys. The presets are used to store different exposures times and intensities. As an example, Presets 3 and 4 are used for 4620 Photoresist. The process sheet will tell you what preset to select. If you press ENTER, exposure data will be shown. Press F4 to go back.
4. Load the mask with the load frame. The mask is used to shield the photoresist from the ultraviolet light. The load frame has small metal pins that are used to align the load frame to

the tray. Similarly the load frame has small plastic pins that are used to align the mask to the load frame. The mask is loaded into the load frame with the chrome side up and the flat of the mask facing the bottom of the load frame. Make sure that the metal alignment pins are seated by trying to slightly move the load frame. Sometimes the metal pins do not always go down into the guides.

5. Move the < TRAY IN>.
6. Align the optics. It is best to visually align the microscope above the alignment marks first. You can use the microscope direction keys for that. If you have the microscope above the alignment marks you will be able to see a ruby red light at the location of the alignment marks on the mask. Once you have the microscope roughed in, look at the computer screen to make the final adjustments. You also may have to use the rotation micrometer to get things aligned. Select LEFT or RIGHT optic. Toggle between microscope and translation with MIC/Chr. Focus optics with MIC/Chr, Z/Y and UP and DOWN direction key. Use the C/F key to select coarse or fine adjustment. When the red light is on for the LEFT key it means that the left optic is selected. When the red light is on for the RIGHT key it means that the right optic is selected. When the red light is on for the Z/Y key, the Z or focus direction is selected. When the red light is off for the Z/Y key, the Y direction is selected. Do the same way with the C/F key. If the red light is on you have selected the coarse focus. Once everything is lined up, you should get a picture on the computer screen. The picture shows the alignment marks close up. After Alignment confirm with <CONTINUE>.
7. Move <TRAY OUT>.
8. Remove load frame and confirm with <CONTINUE>.
9. Load the substrate or wafer with the wafer ruler. The wafer or substrate should be loaded with the flat portion of the wafer against the flat portion of the ruler.
10. Press <CONTINUE>. This will fix the wafer with vacuum.
11. Remove the wafer ruler.
12. Press <CONTINUE> again.
13. Move <TRAY IN>.
14. Press <CONTINUE>.
15. Press <CONTINUE> again. This will start the ultraviolet light exposure. Photoresist is an organic polymer that is used as a shield during processing. Ultraviolet light chemically breaks the photoresist down. Although you will see a violet glow during the exposure, ultraviolet light is not visible. Ultraviolet light is just above violet portion of visible light on the electromagnetic spectrum. Sunlight is also a source of ultraviolet light.
16. Move <TRAY OUT>.
17. Take the wafer off of the vacuum chuck.
18. Press the RESET Key.
19. Unload the mask. Put the load frame back on the tray. Make sure that it is aligned.
20. Then press F1 to say YES
21. Press <CONTINUE>.
22. Move <TRAY IN>.
23. Move <TRAY OUT>. Once the tray is out, make sure that the load frame is taken off of the tray before you go to the next step.
24. Move <TRAY IN>.
25. Turn off the UV light power switch.
26. Turn off the POWER ON key switch.

27. Turn the MAIN switch to the off position.

E.4 Thermal Oxidation Procedure On Silicon Wafer

1. Further cleaning
   a. Make the SC-1 solution and heat hotplate to 150 C
      DI 100 ml

      Hydrogen Peroxide 10 ml

      Ammonium Hydroxide 1 ml (29 drops)

   b. Transfer carrier to SC-1 solution on hotplate
   c. Set hotplate probe to 73˚C; ramp & soak time 30 min
   d. Transfer carrier to DI / IPA beaker (200 /200 ml) 2 min
   e. Rinse with IPA and spin dry
   f. BOE 10 minutes.
2. Thermal Oxidation in furnace tube
   a. Make sure the furnace tube is ready to use, and the N_2 is 2.5L/min
   b. Set the tube temperature to 400^{o}C.
   c. Put the sample carrier into DI for 1 minutes to rinse.
   d. Transfer the carrier with the die into BOE etchant for 1 minutes if the samples is exposed to air for more than 30 minutes. Use only Polypropylene (Do not use glass!) utensil for handle of HF and BOE.
   e. 3 step DI water Rinse; 1 minute for each step.
   f. Transfer carrier and dies into IPA
   g. Spin dry dies
   h. Pull a furnace tube wafer boat out of the furnace.
   i. Put the dies between source wafers.
   j. Load the boat into furnace tube, and push the boat into the center of the tube(>3min). The time will elapse 20' after you have set the temperature, and the temperature will be around 300^{o}C. Whatever the temperature is, load the boat at once.
   k. Begin timing when the temperature arrives at 400^{o}C for 15 minutes.
   l. Set temperature to 1100^{o}C.
   m. Wait until temperature reaches 1100^{o}C (about 20 minutes).
   n. Change O_2 to 6L/min and shut of N_2 flow, begin timing for 13 hours to get 0.5 micron oxide layer.
   o. Set the temperature to 400^{o}C, change the N_2 to reading 2.5L/min and shut off O_2 flow
   p. Wait until the temperature is lower than 800^{o}C (about 40 minutes)
   q. Pull the boat to the mouth of the tube very slowly.
   r. Unload wafers.
   s. Push the boat to the center of the tube.

Author's Biography

Kevin Yu-Chung Lin was born in Kaohsiung, Taiwan in 1984. He moved to Hillsborough, NJ at age 14 and graduated from Hillsborough High school in 2002. He graduated from Rutgers University (State University of NJ) in 2006 with a Bachelor of Science degree in Chemical Engineering and a minor in Psychology. He received *Summa Cum Laude* distinction at graduation. After graduation, he continued his studies at the University of Illinois at Urbana-Champaign. He completed his Master of Science degree in Chemical Engineering in 2009 under the direction of Professor Richard I. Masel. The thesis was on "Application of MEMS technology in design and fabrication of silicon hydrogen microfuel cells and silicon integrated sensor arrays for micro gas chromatography systems." He continued his studies under the same direction of Professor Richard I. Masel for the completion of his Ph.D. in Chemical Engineering.

Publications

9. **Kevin Y. Lin**, A. Salehi-Khojin, D. Estrada, E. Pop, R.I. Masel. "Randomly Stacked Oxide-free Graphene Film as Chemiresistors." In preparation.
8. A. Salehi-Khojin, F. Khalili-Araghi, M.A. Kuroda, **Kevin Y. Lin**, J.P. Leburton, R.I. Masel. "On the sensing mechanism in carbon nanotubes chemiresistors." *ACS Nano* 2011, 5, 153.
7. M. Sayyah, A. Salehi-Khojin, **Kevin Y. Lin**, R.I. Masel. "Electrochemical multiphase microsensor for detection of organophosphates." *Journal of Micromechanics and Microengineering* 2011, 21.
6. A. Salehi-Khojin, **Kevin Y. Lin**, C.R. Field, R.I. Masel. "Nonthermal current-stimulated desorption of gases from carbon nanotubes." *Science* 2010, 329, 1327-1330.
5. S. Moghaddam, E. Pengwang, **Kevin Y. Lin**, R.I. Masel, M.A. Shannon. "Fuel cell-based MEMS power source." *ASME International Mechanical Engineering Congress and Exposition Proceedings* 2009, v 13, n PART B, 817-819.

4. **Kevin Y. Lin**, R.D. Morgan, H.S. Kim, L. Zhu, B. Gurau, M.A. Shannon, R.I. Masel. "A MEMS based miniature hydrogen fuel cell for portable power generation." *Technical Digest of IEEE Solid-State Sensor and Actuator Workshop* 2008.

3. L. Zhu, **Kevin Y. Lin**, R.D. Morgan, V.V. Swaminathan, H.S. Kim, B. Gurau, D. Kim, B. Bae, R.I. Masel, M.A. Shannon. "Integrated micro-power source based on a micro-silicon fuel cell and a micro electromechanical system hydrogen generator." *Journal of Power Sources* 2008, 185(2), 1305-1310.

2. S. Moghaddam, E. Pengwang, **Kevin Y. Lin**, R.I. Masel, M.A. Shannon. "Millimeter-scale fuel cell with onboard fuel and passive control system." *Journal of MEMS* 2008, 1388.

1. L. Zhu, **Kevin Y. Lin**, R.D. Morgan, H.S. Kim, B. Gurau, D. Kim, B. Bae, R.I. Masel, M.A. Shannon. "Development of a fully integrated micro-power source based on a micro-silicon fuel cell and a MEMS hydrogen generator." *Technical Digest of IEEE Solid-State Sensor and Actuator Workshop* 2008.